GEORG-AUGUST-UNIVERSITÄT
GÖTTINGEN

Dissertation

Precise Nanoengineering of Polymer Functionalized Nanomaterials with Silica as Coating and Templating Tools

Yingying Cai

Göttingen,2021

GEORG-AUGUST-UNIVERSITÄT
GÖTTINGEN

Precise Nanoengineering of Polymer Functionalized Nanomaterials with Silica as Coating and Templating Tools

Dissertation

zur Erlangung des mathematisch-naturwissenschaftlichen Doktorgrades
"Doctor rerum naturalium"
der Georg-August-Universität Göttingen

im Promotionsprogramm Chemie
der Georg-August University School of Science (GAUSS)

vorgelegt von

Yingying Cai

aus Shanghai, China

Göttingen, 2021

Betreuungsausschuss

Prof. Dr. Philipp Vana, MBA	Institut für Physikalische Chemie Georg-August-Universität Göttingen
Prof. Dr. med. Frauke Alves	Institut für Diagnostische und Interventionelle Radiologie Universitätsmedizin Göttingen
Prof. Dr. Andreas Janshoff	Institut für Physikalische Chemie Georg-August-Universität Göttingen

Mitglieder der Prüfungskommission

Referent

Prof. Dr. Philipp Vana, MBA	Institut für Physikalische Chemie Georg-August-Universität Göttingen

Korreferent

Prof. Dr. med. Frauke Alves	Institut für Diagnostische und Interventionelle Radiologie Universitätsmedizin Göttingen

Weitere Mitglieder der Prüfungskommission

Prof. Dr. Andreas Janshoff	Institut für Physikalische Chemie Georg-August-Universität Göttingen
Jun.-Prof. Dr. Daniel Obenchain	Institut für Physikalische Chemie Georg-August-Universität Göttingen
Dr. Tim Schäfer	Institut für Physikalische Chemie Georg-August-Universität Göttingen
Prof. Dr. Marcus Müller	Institut für Theoretische Physik Georg-August-Universität Göttingen

Tag der mündlichen Prüfung: 16. Dezember 2021

Contents

Abstract

The construction of a well-defined hybrid nanostructure becomes possible if functional polymer meets inorganic nanomaterials in a well-designed way. To fully control the structure of the nanohybrid and create the synergy between the surface-bound polymer and the nanomaterial, a vast variety of engineering options must be understood in-depth and practically optimized for both functional polymer and nanomaterials. These options include: I) size (distribution), colloidal stability, and surface ligand exchange for the nanomaterials; II) type of monomer(s), chain-length, topological design, and end-group functionalization for the surface-grafted polymer; III) the anchoring strategies between the polymer and surface of the nanomaterials.

In this thesis, four projects, focusing on the design and fabrication of four different nanohybrids with polymers functionalization for different applications, are presented. Within these projects, reversible addition-fragmentation chain transfer (RAFT) polymerization technique was employed to fabricate the functional polymer with full control of the macromolecular architecture. These RAFT polymers are introduced onto different types of nanoparticles (NPs) with high capping density, yielding hybrid nanocomposite with well-defined structures.

Another important strategy used in this thesis is the silica coating/fabrication method. It includes the classic one-phase coating approach and reversed microemulsion technique. Choosing suitable methods and conditions, the silica coating can be performed in a controlled fashion. For those nanomaterials without effective surface chemistry, the thin silica shell brings its well-established surface chemistry to them, e.g., for introducing polymer brushes.

The reversed microemulsion method for silica coating found its

application in the first project: superparamagnetic ~ 8 nm magnetite nanoparticles (MNPs) bearing hydrophobic ligands were uniformly coated with a thin silica shell of a thickness of ~ 12 nm in a one-to-one fashion. From the silica surface, the surface-initiated RAFT polymerization was performed to introduce a dense hydrophilic and thermo-responsive poly(*N*-isopropylacrylamide) (PNIPAM) shell. The highlight of this project is the dramatic change of the superparamagnetic properties of the MNPs after silica coating and polymer functionalization. The superconducting quantum interference device (SQUID) measurements impressively demonstrated the complete suppression of the magnetic interaction between the MNPs even in the dry-powder state. This result is very intriguing for magnetic hyperthermia applications where the magnetic interaction is highly unfavored for its strong jeopardizing effect on the heating performance.

The thesis further focused on the nanoengineering of Egyptian blue nanosheets (EBNS). Egyptian blue (EB) is a near-infrared (NIR) fluorescent material with excellent photoluminescence (PL) performance. However, the lack of effective production of this nanomaterial and the absence of a surface modification method are the bottlenecks of EBNS to be applied as a cost-effective NIR fluorophore for a wide audience, especially in the NIR bioimaging field. To unfold this feature, high-energy ball milling technique was first applied to enable the mass production of the nanomaterial, with a significantly reduced size of EBNS. Again, silica coating was chosen here to introduce effective surface modification on EBNS. During the project, two new challenges were found for EBNS: the significant size-dependent PL performance, and the strong light scattering effect of EBNS in colloid caused by the mismatch of the refractive index of EBNS and water. These insights are very important for optimizing PL performance of EBNS for detailed application scenarios, e.g., choosing the suitable size of EBNS and its dispersion media. Under this consideration, two types of polymers, hydrophobic PNIPAM, and hydrophilic poly(methyl methacrylate) (PMMA) brushes were introduced to the surface of EBNS respectively, to enhance the dispersibility of EBNS in the diverse media. Notably, the good match of the refractive index of PMMA, silica, and EBNS in one nanohybrid can significantly reduce the scattering event thus increasing the PL output of the

material.

The role of silica is very flexible in the fabrication of hybrid nanomaterials. Rather than as coating material for further functionalization, in the project of creating circular AuNPs nanopattern, ~ 46 nm silica NPs served as a temporary template for the colloidal self-assembly of polyethylene glycol (PEG) capped ~ 13 nm AuNPs, by utilizing the adsorption between the surface-grafted PEG and the silica surface. Surprisingly, after depositing the silica-Au nanostructure on the substrate, the AuNPs were perfectly arranged into a 2D circular nanopattern. To completely remove the silica content without alerting the circular AuNPs pattern, an etching condition was established using an extremely concentrated NaOH solution at increased temperature. Both high ionic strength from NaOH and increased temperature can significantly raise the efficiency of silica etching while immobilizing PEG capped AuNPs on the substrate without any diffusion, since PEG is unsolvable under this condition. The perfect circular AuNP pattern has great potential to be used as an innovative nanopixel for advanced nanopatterning.

Furthermore, this thesis focused on the fabrication of novel nanostructure for *in vivo* phase-contrast computed tomography (CT) experiments under synchrotron radiation. In this project, the impact of the geometry of AuNPs on the contrast performance was studied by comparing "hollow AuNPs" with solid AuNPs with the same penetration thickness. To mimic a "hollow" AuNP, the self-assembly approach was used to fabricate a dense layer of ~ 5 nm AuNPs onto thiol functionalized ~ 37 nm silica NPs. Both nanostructures were functionalized with PEG to increase the colloidal stability under extremely high concentration (100 mgAu/mL). The *in vivo* experiment confirmed the strong CT enhancement of "hollow" AuNPs for lung imaging.

1

Polymer Functionalized Nanomaterials: State of the Art

The rise of surface-bound polymer brushes has revolutionized the surface engineering of nanomaterials. This chapter briefly summarizes the recent progress on the fabrication strategies for polymer/inorganic nanohybrids for various applications including biomedical (**Section 1.1**) and surface nanopatterning (**Section 1.2**). On this topic, RAFT polymerization offers great design options to create synergy between nanocomponents and polymer, which will be discussed in detail.

1.1 (RAFT) polymer functionalized nanomaterials in modern biomedical applications

For biomedical applications, surface modification is one of the most important topics for almost all types of nanomaterials. For this task, the functional polymer can integrate its favored functions, e.g., bio-compatibility, stimuli-responsive, to the nanomaterial for the hybrid performance or simply enhance the colloidal stability. The structural designs of the polymer brushes including anchoring strategies, choosing of functional monomer, and topological structure are all crucial for the desired functional integration between polymer and nanomaterials.

Since the debut of RAFT polymerization in 1998,[1] it has quickly shown its talent for the precise fabrication of polymer with flexible design and special functions. The RAFT polymerization technique offers well-defined

polymer chain length, flexible end-group modifications, access for block-copolymer, and topological designs.[2-12] These precise design options and wide selection of monomers induced an explosion of applications including e.g., drug-delivery,[13-17] bio-imaging and diagnosis,[18,19] bioseparation,[20] stimuli-responsiveness.[21-23] All these above-mentioned advantages play important roles in the revolution of surface engineering of nanoparticles. In this way, the polymer-functionalized inorganic nanomaterials have experienced extensive product proliferation for a wide range of applications, especially in the biomedical field.[24-26]

Since many useful nanomaterials, e.g., superparamagnetic magnetite NPs (MNPs), quantum dots, upconverting NPs are protected with hydrophobic ligands (e.g., oleic acid, oleylamine) and thus only dispersible in hydrophobic solvents. The first critical task for any biological application is to transfer these NPs into aqueous environments, with high colloidal stability and biocompatibility. Here, the surface-bound polymer shell offers a greater ability to introduce long-term aqueous colloidal stability and the non-specific interaction of nanomaterials with the biomolecules (antifouling). A great variety of polymers have been developed for this task, e.g., polyethylene glycol (PEG),[27,28] poly(2-hydroxyethyl methacrylate),[29] polyvinylpyrrolidone,[30,31] poly(2-oxazoline),[32] and zwitterionic polymers.[33,34] Among these candidates, PEG and its derivatives are the most widely used polymer for their reliable performance and good commercial availability. RAFT polymerization also provides very good access for the synthesis of PEG-based polymer with versatile anchoring strategies toward diverse nanomaterials.[35-40]

There are two major factors that influence the stabilizing performance from the polymer shell. One is the strength of anchoring between the polymer and surface, the second factor is the capping density. To avoid detachment and increase the capping density of polymer, strong and effective grafting approaches are required. On this topic, **Section 2.2** will provide a detailed discussion on the anchoring strategies used in this thesis.

Surface-grafted polymer brush has found great success in the realm of smart drug delivery. In these applications, polymers with stimuli-responsive

properties, especially thermal-responsiveness, are great tools to achieve targeted delivery due to the temperature difference in diverse environments. For example, in this thesis, the thermal responsive PNIPAM is chosen as the polymer shell for several projects. The PNIPAM possesses a lower critical solution temperature (LCST) behavior. This solution-cloud transition is a combination of enthalpic and entropic effect:[23,41,42] Above its LCST, hydrated PNIPAM lost most of its attached water molecules with the release of drug molecules.[43-45] All these smart properties can be introduced to the nanomaterials in the form of surface grafted RAFT polymers. Furthermore, the thermal-responsive polymer brushes can synergize with the thermal properties from the core-materials to induce the LCST by external stimuli. Combining local hyperthermia methods, e.g., NIR photon,[46-49] ultrasound,[50] magnetic field,[45] the thermal responsive drug-release can be monitored in a certain region of the body, such as a solid tumor.[51] The simultaneous drug release from the polymer shell with hyperthermia creates an enhanced performance for cancer treatment.

1.2 Nanopatterning with polymer capped metal nanoparticles

Arranging nanoparticles on a macroscopic substrate with an ordered pattern induced a great variety of applications for a wide audience including sensing,[52-55] metal-assisted chemical etching,[56,57] superhydrophobic coating,[58] and biomedical research.[59-62] Innovations in nanopatterning often lead to significant breakthroughs in nanotechnology.

On this topic, the high precision arrangement of the nanoparticles is crucial here: the nanopattern must be clearly defined in a periodic manner, and the distance between the nanoparticles must be adjustable. To achieve this, both interparticle interaction and particle–substrate interaction must be understood in-depth. In this regard, the unmodified NPs are unsuitable for this task: either densely packed nanoparticle arrangement or nonordered structure. To deposit nanoparticles in a certain pattern (hexagonal or square

array), methods based on block copolymer self-assembly have made great progress.[63,64] Especially, block copolymer micelle nanolithography offers a very efficient and precise patterning of a wide range of metal nanoparticles.[64-67]

In these approaches, noble metal nanoparticles are widely used as patterning units for their useful plasmonic interaction and well-established surface chemistry for later modifications. Typically, the precursor salt (e.g., $HAuCl_4$, H_2PtCl_6) is loaded inside the block copolymer micelles, the NPs can be obtained either by reduction with N_2H_4[68], or directly using plasma treatment[67] after the polymer micelles are deposited on the substrate[67]. **Figure 1-1 A** demonstrates the typical hexagonal nanopatterned AuNPs (gold nanoparticles) obtained from this method. By varying the concentration of the block copolymer in the micelle solution, the interparticle distance can be tuned between 50 to 150 nm.[60] To render further structural information to the nanopattern, electron beam lithography[68] and masking methods[67,68] are often applied to create structure on a higher scale level (typically in the micrometer range). **Figure 1-1** demonstrated some selected patterns fabricated with block copolymer micelle approach by using electron beam lithography (**B**) and polystyrene sphere mask (**C**).

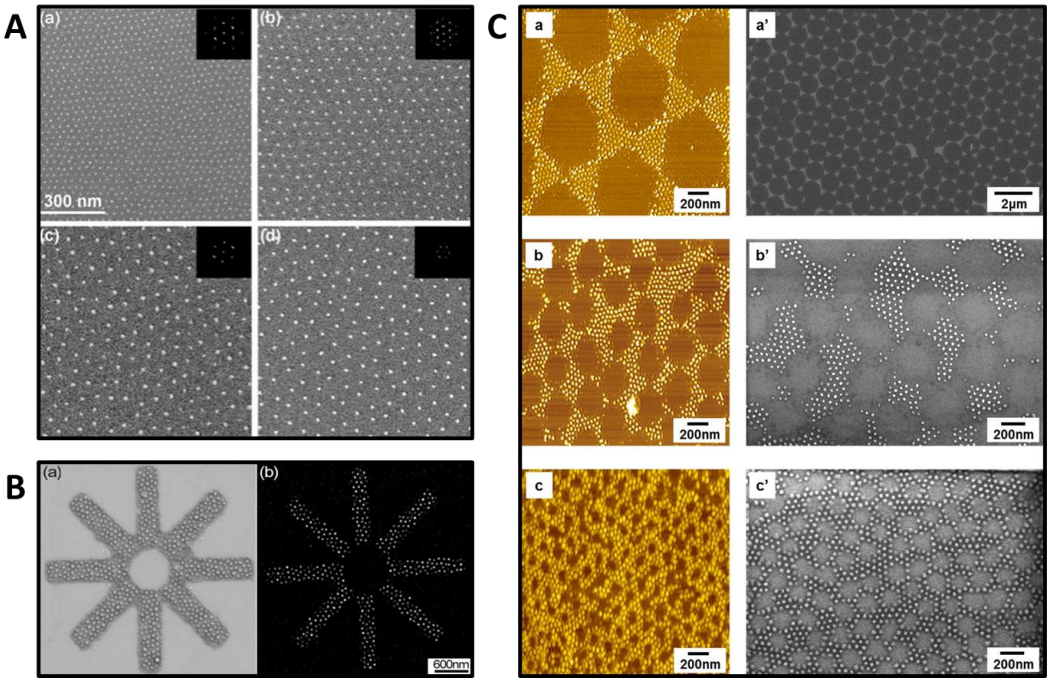

Figure 1-1 (**A**) SEM images of hexagonal patterned AuNPs from block copolymer

micelle nanolithography with increasing interparticle distance. (**B**) SE micrographs of star-shaped nanopatterned (a) block copolymer micelles and (b) Au-nanoparticles using mask drawn by the electron beam. (**C**) (a–c) AFM images of micro-nanopatterned block copolymer micelle arrays after plasma treatment using the PS sphere as an etching mask, with diameters of 1.0 µm, 500 nm, and 250 nm, respectively. (a'–c') SEM images of micro-nanopatterned Au arrays fabricated from a–c. Adapted with permissions from reference[68] (A–B), copyright 2003 Institute of Physics Publishing Ltd; from reference[67] (C), copyright 2016 American Chemical Society.

The lower limit of the interparticle distance from the block copolymer micelle technique is around 50 nm. For nanopatterns with interparticle distance < 50 nm, NPs with the surface grafted polymer are one of the best candidates. **Figure 1-2 A–B** shows the hexagonal nanopattern formed by RAFT PNIPAM capped ~ 13 nm AuNPs with tunable distance.[69] This approach is also available as a grafting-from method for silica NPs (**Figure 1-2 C–D**).[70] The success of these methods relies heavily on the high capping density of the surface-bound polymer brushes.[69-71] Detailed discussion on the topic of high efficient grafting strategies can be found in **Section 2.2**.

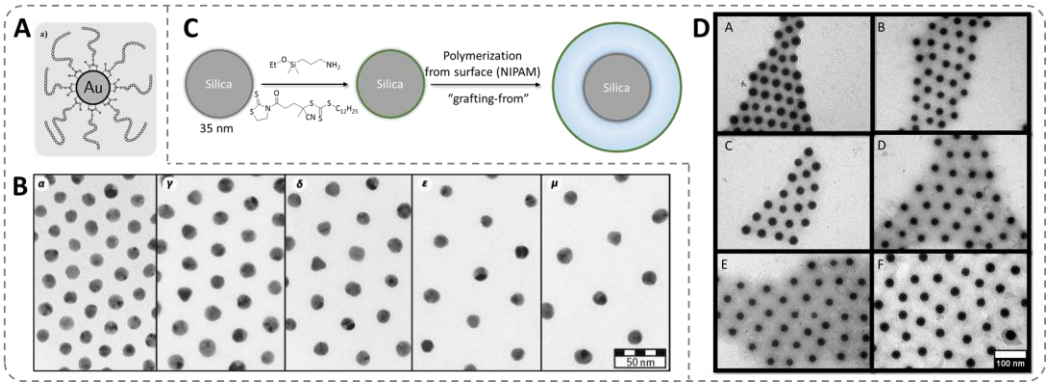

Figure 1-2 (**A**) Schematic illustration of RAFT polymer grafted AuNPs. The RAFT groups act as anchoring moieties onto the surface of AuNPs. (**B**) TE micrographs of PNIPAM capped AuNPs in hexagonal patterns with increasing interparticle distance controlled by the polymer chain length. (**C**) Schematic illustration of the grafting-from strategy of PNIPAM on silica NPs surface with SI RAFT polymerization. (**D**) TE micrographs of PNIPAM capped silica NPs with increasing interparticle distance. Adapted with permissions from reference[69] (A–B), copyright 2013 American Chemical Society; from reference[70] (C–D).

Notably, all the above-mentioned methods use a single NP as a templating unit. The innovation of the patterning units can be achieved by

using well-defined nanostructures carrying their own specific particles arrangement. This approach allows the integration of the hierarchical nanoassembly design and the ordered surface arrangement to create a unique surface nanopattern. In our group, a series of colloidal planet–satellite nanostructures with a great choice of nanoparticles including gold,[72] silver,[73] and silica NPs[70] are fabricated using RAFT polymer as linker (**Figure 1-3**). These nanostructures have interparticle distances typically between 5 to 50 nm controlled by the functional polymer linkers. Their colloidal nanostructures can also be coated onto a substrate like glass, silicon wafer, and CaF_2 surface using dip-coating method to form a homogenous monolayer.[70]

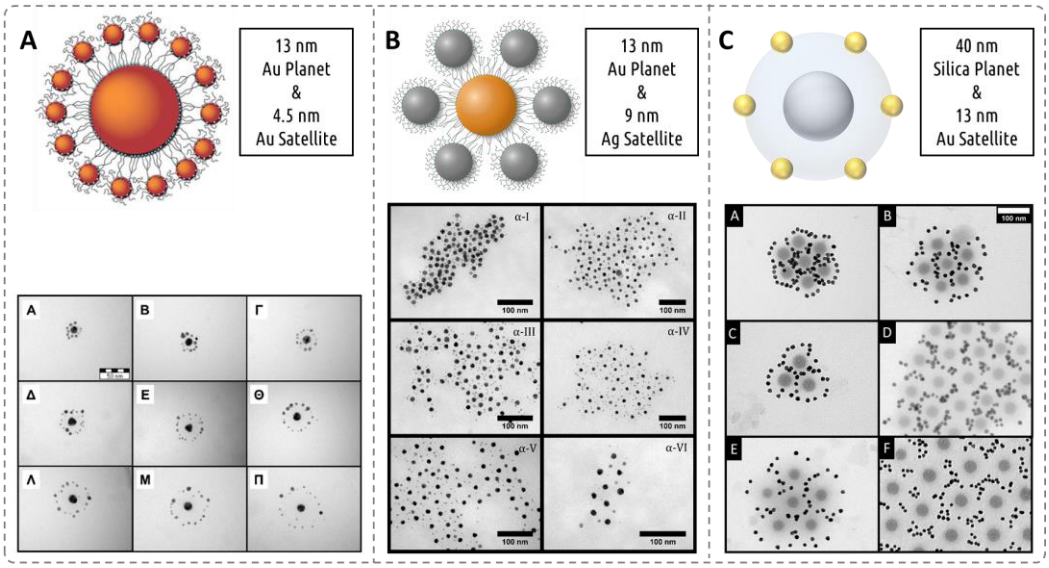

Figure 1-3 Schematic illustrations and TE micrographs of the planet–satellite nanostructures consisting of (**A**) ~ 13 nm AuNPs as planets and ~5 nm AuNPs as satellites, (**B**) ~ 13 nm AuNPs as planets and ~ 9 nm AgNPs as satellites, (**C**) ~ 40 nm silica NPs as planets and ~ 13 nm AuNPs as satellites. Adapted with permissions from reference[72] (A), copyright 2014 John Wiley and Sons; from reference[73] (B), Copyright 2016 American Chemical Society; from reference[70] (C).

2
Theoretical Background and Methodology

The theoretical background and methodology involved in this thesis are reviewed in this chapter, which comprises of three topics: the formation and surface chemistry of silica NPs and silica-coated nanomaterials (**Section 2.1**), anchoring strategies for polymer onto nanomaterials (**Section 2.2**), and the properties and nanoscience of NIR fluorescent Egyptian blue (**Section 2.3**).

2.1 Fabrication and modification of silica in nanoscale

Silica has always been the most extensively used nanomaterial since the seminal study from Stöber *et. al.* in 1986[74]. The role of silica in modern nanoengineering goes quickly beyond simply applying it as conventional particles, for example, silica coating has become a popular tool to enable surface modification of a large variety of nanomaterials.[75] Here, silica surface offers a series of advantages including biocompatibility, colloidal stability, and a great library of well-established silica surface chemistry.[76,77] Especially for the nanomaterials exhibiting difficulties in the direct surface chemistry, e.g., quantum dots,[78] magnetite,[79-81] and zirconia,[82] silica-coating always provides an "all-round strategy" for introducing surface modifications.

This section will focus on the synthetic strategies for both silica NPs and silica coating, along with the elucidation of the mechanisms (**Section 2.1.1**). Also, the surface modification options on the silica surface, in particular, the commonly used approaches for grafting polymers onto silica surface will be discussed in **Section 2.1.2**

2.1.1 Mechanisms and methods of silica formation in nanoscale

One of the most widely used methods to fabricate silica NPs is the "classic" Stöber process[74]. This reaction is based on polycondensation of hydrolyzed TEOS (tetraethyl orthosilicate) in ethanol solution with ammonia as the catalyst. The mechanism is shown in **Scheme 2-1** including two steps: (I) Hydrolysis of ethoxyl groups in TEOS into silanol monomers, and (II) subsequent condensation of hydrolyzed TEOS into silica networks.

Scheme 2-1 Simplified reaction scheme of Stöber process.

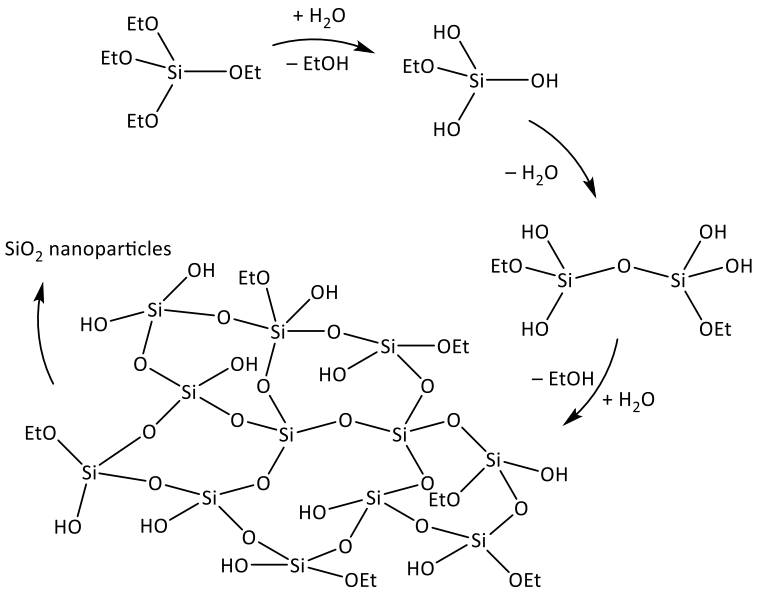

LaMer theory[83,84] provides a quantitative description on the formation of silica NPs which is divided into three stages (**Figure 2-1**): (I) The concentration of hydrolyzed TEOS (C) increases rapidly with the proceed of the hydrolysis reaction, no nucleation occurs during this stage. (II) The nucleation starts when C exceeds a critical point C_{crit}. (III) The nuclei further grow until $C < C_s$.[85]

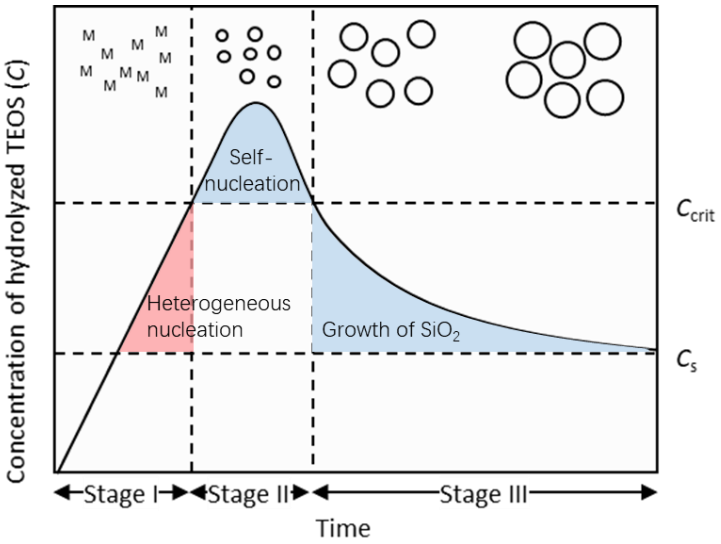

Figure 2-1 Schematic illustrated LaMer theory for the formation of silica NPs. "M" represents hydrolyzed TEOS.

Stöber method is also used as a general tool for silica coating on nanomaterials. Here, the nanomaterials servers as a heterogeneous core, on which the nucleation of silica is much easier than the self-nucleation case since the nucleating surface already exists. As the result, if C is controlled below C_{crit} (**Figure 2-1**, red region), the silica prefers to heterogeneously grow on the surface of foreign nanomaterials: The core–shell structure will be formed without core-free silica nanoparticles. In the case of $C > C_{crit}$, both targeted core–shell structure and free silica NPs could present in the products.[86] As the most straightforward approach for silica-coating, the Stöber method can be applied to many nanomaterials. It also provides tunable silica thickness by varying the feed ratio of TEOS and reaction time.[86-89] However, this method heavily relies on the perfect dispersibility of coated nanomaterials in ethanol solution for the entire coating process. A feasible strategy to circumvent this issue is to use polyvinylpyrrolidone as the stabilizer. This amphiphilic polymer has efficient adsorption onto a decent variety of charged collides, e.g., noble metal NPs, boehmite rods, gibbsite platelets, and charged poly(styrene) particles,[75] enabling to transfer particles from water into ethanol for the subsequent silica coating.[77]

Water-in-oil (w/o) microemulsion (also known as reversed

microemulsion) technique is a powerful method to synthesize silica NPs or perform silica-coating on core NPs with uniform, tunable size, and high roundness. With the aid of surfactant, nanosized water micelles containing ammonia are formed in the cyclohexane environment, where TEOS undergoes hydrolysis and condensation, forming silica NPs with superior monodispersity particularly in the range of 30–60 nm.[90,91]

When using this method for silica-coating, NPs with hydrophobic protecting ligand (e.g., alkylamine) are the suitable core candidates: they can be dispersed in cyclohexane environment to participate in the silica formation. Koole *et. al.* elucidated a ligand exchange mechanism that the alkylamine ligand on the quantum dots (QDs) surface can be replaced with both hydrolyzed TEOS and surfactant molecules (IGEPAL® CO-520). The ligand exchange facilitates the incorporation of QDs into the water micelle, where the further silica growth takes place (**Figure 2-2**). Since the quantum efficiency of QDs is highly correlated to its surface-ligand interaction, this ligand exchange process was confirmed by the fluorescence quenching event caused by the hydrolyzed TEOS and surfactant molecules on QDs.[91] Ding *et. al.* also approved this mechanism with the Fourier-transform infrared spectroscopy analysis during the silica-coating process on MNPs.[86]

Furthermore, since the ligand exchange is the crucial step for the heterogenous nucleation, both ligand and surface properties of the core NPs have a huge impact on the result of silica coating. Under specific conditions, an eccentric silica coating can be maneuvered. Koole *et. al.* reported that the presence of stronger ligands (alkylthiol) can hinder the ligand exchange thus resulting in incomplete or delayed incorporation of QDs.[91] In the case for noble metal NPs, they process intrinsic strong affinity towards alkylamine. The strongly bonded amine ligand can also lead to a partial replacement of hydrolyzed TEOS and yield an eccentric silica coating.[92,93] A widely agreed mechanism for the formation of eccentric silica coating is illustrated in **Figure 2-3**. Here, since the hydrolyzed TEOS is immiscible with the hydrophobic surface ligands, phase segregation of the ligands occurs on the NPs surface. As the result, the nucleation and silica growth can only occur on the hydrophilic site on the NPs, giving the eccentric product.[92,94]

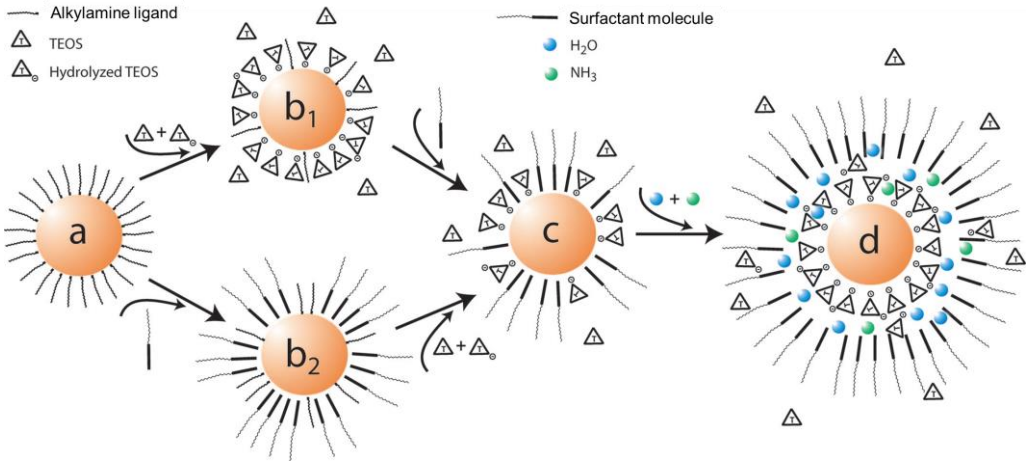

Figure 2-2 Illustration of mechanism for silica coating on QDs in w/o microemulsion system. (a) QDs capped with alkylamine ligand. (b) Ligand exchange of alkylamine with hydrolyzed TEOS (b_1) or surfactant (b_2). (c) Equilibrium state between hydrolyzed TEOS and surfactant molecules on QDs surface. The alkylamine is completely replaced. (d) After the addition of ammonia, the concentration of hydrolyzed TEOS further raises and completely replaces the surfactant molecules with the formation of the micelle, where silica further grows on the QDs surface. Adapted with permission from reference[91], copyright 2008 American Chemical Society.

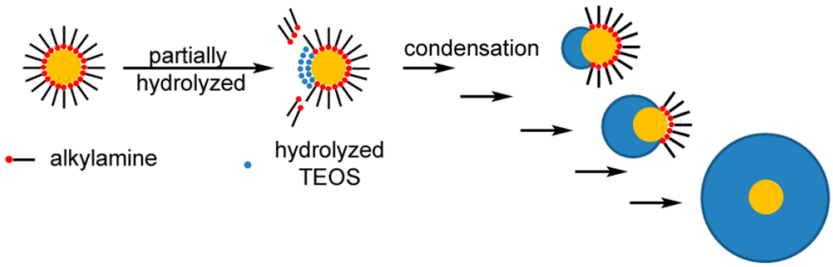

Figure 2-3 Schematic illustration for the mechanism of eccentric silica coating on alkylamine capped AuNPs. Adapted with permission from reference[92], copyright 2014 American Chemical Society.

2.1.2 Surface modification strategies on the silica surface

As mentioned before, the surface chemistry of silica is well established and found many applications in various fields. Arising from the favorable silanol groups on its surface, silica can be modified with a large variety of functional moieties through condensation with corresponding alkoxysilanes.[76,95] Most frequently, amine or thiol terminated silanes are used to anchor subsequent chemical or biological moieties, utilizing their

convenient linkage with e.g., *N*-hydroxysuccinimide- (NHS), isothiocyanate-, maleimide-, and carboxyl-functionalized groups.[76,95,96]

These efficient anchoring approaches also open the routes to introduce polymer brushes onto the surface of silica. By far the most powerful and widely used strategy here is SI polymerization. Different Synergies between silica and libraries of polymer with diverse functions are reported in the literature, mainly achieved by surface-initiated (SI) RAFT polymerization[96-98] and atom transfer radical polymerization (ATRP)[71,99-101]. For doing this, RAFT agents or initiators for ATRP must be first anchored on the silica surface. Commonly, silica surface carrying RAFT agents can be prepared with a two-steps reaction: Silica surface is first modified with amine groups by using aminosilane and followed by anchoring RAFT agents with activated carboxyl groups.[96,102-105] For SI-ATRP, α-bromoisobutyrate groups are the most commonly used initiator.[71,101] Readers interested in this topic are referred to a detailed review[106] elsewhere.

2.2 Strategies for anchoring polymer onto nanomaterials*

Functional polymers are used to enhance the performance of diverse materials and quickly found applications in various fields of research and industry.[12] Particularly, RAFT polymers are widely applied for surface modification on nanomaterials, such as on NPs or membranes. The enormous surface area and comparable size of nanomaterials maximize the effect brought by the polymer functionalization. In this section, the most applied anchoring strategies for introducing RAFT polymers, including grafting-to and grafting-from approaches are reviewed.

---

* Reproduced from Peng, W.; Cai, Y.; Fanslau, L.; Vana, P. *Polymer Chemistry* **2021**, DOI: 10.1039/D1PY01172C. with permission from Royal Society of Chemistry.

2.2.1 Grafting-to and grafting-from approaches for introducing RAFT polymer to nanomaterials

The binding of RAFT polymers onto the surface of nanomaterials requires specific chemistry towards each type of surface. A number of different anchoring strategies are available to link RAFT polymers to a surface, which often come with their own merits and shortcomings. Researchers should carefully consider suitable anchoring options depending on the properties of their system, including the type of polymer, the surface character of the NP, the properties of the protecting ligand, and the required capping density of the polymer on the surface.

In general, there are two most commonly employed grafting strategies: grafting-to and grafting-from approaches. In the grafting-to strategy, the pre-synthesized polymer is introduced to the surface, whereas in grafting-from, the polymer synthesis is initiated from the NP surface (**Scheme 2-2**). Grafting-to is considered a more straightforward method,[107] since the grafting step can often be facilitated by a simple ligand exchange reaction: polymers carrying a functional group with a stronger affinity towards the NP surface tend to replace the weaker binding protecting ligand. Also, polymer and NPs are individually prepared to allow for separate syntheses conditions and hence tight control over polymer characteristics.[108-110] In contrast, grafting from surfaces demands the attachment of the RAFT agent before RAFT polymerization. In this stage, the surface-bound RAFT agent might alter the colloidal stability of the system since the protecting effect of these small molecules is very limited. Special care on the storage and purification steps must be given to avoid irreversible aggregation.[111,112] Moreover, the polymerization conditions must be optimized for the NPs as well to ensure the complete dispersion of NPs in the polymerization mixture. For the modification of bio-surfaces or bio-containing surfaces such as proteins, the grafting-from approach can struggle to retain the biological functionality after polymerization.[110] Furthermore, the characterization of the surface-bound polymer is not as straightforward as for grafting-to approaches.[111,113] Oftentimes, the free polymers formed in solution are characterized as a substitute for the surface-anchored ones, as they are quite similar with

respect to molecular weight and dispersity.[114,115]

Scheme 2-2 Illustration of the most commonly used strategies to immobilize polymers onto the surface of NPs. (**A**) Grafting-to, (**B**) grafting-from with B_1 for R-approach and B_2 for Z-approach.

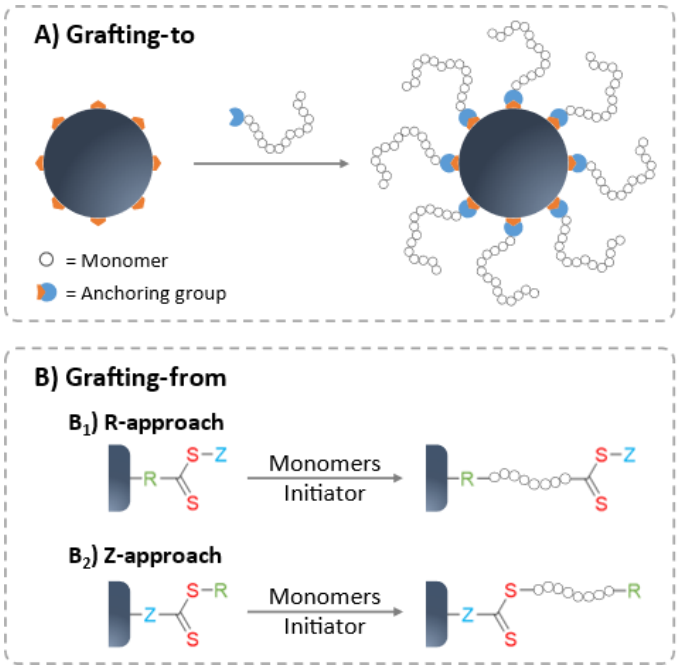

However, in many cases, grafting-from outperform grafting-to approaches in terms of obtained grafting density.[26,109,110,116,117] This difference can be explained by the steric hindrance effect during the grafting-to process: the approaching polymer chain is sterically blocked by the grafted polymer chains as well as by binding site masking *via* random coil formation of the approaching polymers.[109,110] The grafting-to approach often shows chain length dependence and performs better with shorter polymer chains.[107,118] Other challenges for grafting-to approaches are the ligand exchange process and the efficiency of the anchoring chemistry. The reader should keep in mind that the surface properties of NPs differ strongly from their bulk counterpart, mainly due to the protection ligand from the synthesis. Oftentimes, choosing NPs with suitable ligand and solvent combinations is the key to a successful polymer-ligand exchange.

Notably, the molecular design of the attached RAFT agent plays a critical role when it comes to polymerization characteristics of the grafting-from approach. If the RAFT agent is coupled to the surface *via* its R-group (R-group approach), the polymer chains grow while being attached to the surface. The

propagating radical is located at the solvent-facing polymer terminus, thereby able to readily engage with monomers and RAFT agents in the solution during the whole polymerization process, even at high molecular weights (**Scheme 2-2 B**). Consequently, high monomer conversion and narrow polymer dispersity of the grafted polymer can be achieved.[96,108,115] Concerns could arise due to the termination between surface-bound radicals (both inter- and intra-particle termination). However, since an excess of free RAFT agent is often added to the polymerization mixture, the termination reaction is then dominated between the solution radicals.[119] Similar to the solution polymerization without NPs, the amount of initiator must be controlled to avoid the formation of termination product on the surface-grafted polymer shell,[120] which precludes further polymerization to longer polymers or BCPs. An important advantage brought by R-approach is that the RAFT moieties will stay on the outward-facing chain termini of the surface-grafted polymer brushes which can be utilized for further modifications.

In contrast, if the RAFT agent is anchored *via* the Z-group (also called transfer-to), the thiocarbonylthio groups are permanently attached to the surface during and after polymerization. This means that radical chain propagation and termination only occur in the solution. This approach only allows active radicals to recombine back onto the surface-grafted Z-groups, giving the advantage of avoiding the anchoring of any terminated product (**Scheme 2-2 B**).[119] However, since the recombination of polymer radicals with the surface RAFT Z-groups has a similar steric issue as the grafting-to approach, in practical, R-group approaches are often favored over Z-group approaches, especially for longer polymers.[108,109,120,121] Furthermore, for the first step of anchoring RAFT agents onto the surface, the R-group offers easier access to introducing anchoring moieties over the Z-group.[119] Also, the Z-group approach locates the thiocarbonylthio group directly on the surface of the NPs, which comes with a potential risk of chain stability loss due to hydrolysis or aminolysis of the RAFT agent.[122]

In summary, understanding the mechanism and character of each approach is necessary for the successful design of the experiment. The

approach of introducing polymer shells on the surface of NPs must be chosen according to the specific type of NP including its surface ligands and solvent conditions.

2.3 NIR luminescent Egyptian blue nanosheets

2.3.1 From the earliest artificial pigment to the NIR fluorescent nanomaterial

Flashback to 2600–2480 B.C., blue is the divine color for ancient Egyptians to express their gods and universe. Since blue pigment was extremely rare in nature, the ancient Egyptians synthesized the earliest artificial pigment – "Egyptian blue" (EB). This pigment was extensively used in that era until the end of Roman times.[123,124]

The initial encounter of this pigment with modern scientists dates back to the 19th century, during excavation at Pompeii. In 1959, the crystal structure of $CaCuSi_4O_{10}$ (main composite of EB) was first revealed by Pabst.[125] Using X-ray diffraction experiment, $CaCuSi_4O_{10}$ was identified as a silicate with a layered structure.[125-127] In 2000, Pozza. *et. al*. discovered an intriguing property of EB: it possesses NIR photoluminescence with emission at ~ 920 nm and a broad excitation band covering 450–700 nm.[128] This trait provides archaeologists and museum scientists access to identify painting material in cultural heritage in a non-invasive manner.[129] Later, Accorsi *et. al*.[130] determined an exceptionally high quantum yield (> 10.5%) and a long lifetime (107 μs) of this NIR luminescence.

Based on the nature of its layered crystal structure, in 2013, Johnson-McDaniel *et. al.*[131] established a method to exfoliate EB into nanosheets (EBNS), generating a new avenue of EB for the nano-applications.

2.3.2 Properties of the $CaCuSi_4O_{10}$ crystal

Egyptian Blue consists mostly of crystalline $CaCuSi_4O_{10}$ that contributes

to the blue coloration and NIR photoluminescence properties. In this section, the properties of the $CaCuSi_4O_{10}$ including its crystal structure, energy levels, and the origin of its color as well as PL features will be reviewed.

As shown in **Figure 2-4**, $CaCuSi_4O_{10}$ is a phyllosilicate (layered silicate) with a tetragonal structure in *P*4/*ncc* space group (gillespite structure). Within one unit cell, [SiO_4]-tetrahedra are linked as two [Si_8O_{20}] sheets. A copper ion is coordinated by four O-atoms from the unshared corners of [SiO_4]-tetrahedron in a square planar (D_{4h}) symmetry, and builds a silicate layer parallel to the (100) plane. Calcium ions are located between the silicate layers coordinating midway with eight oxygen atoms and holding the layers together.[125,126]

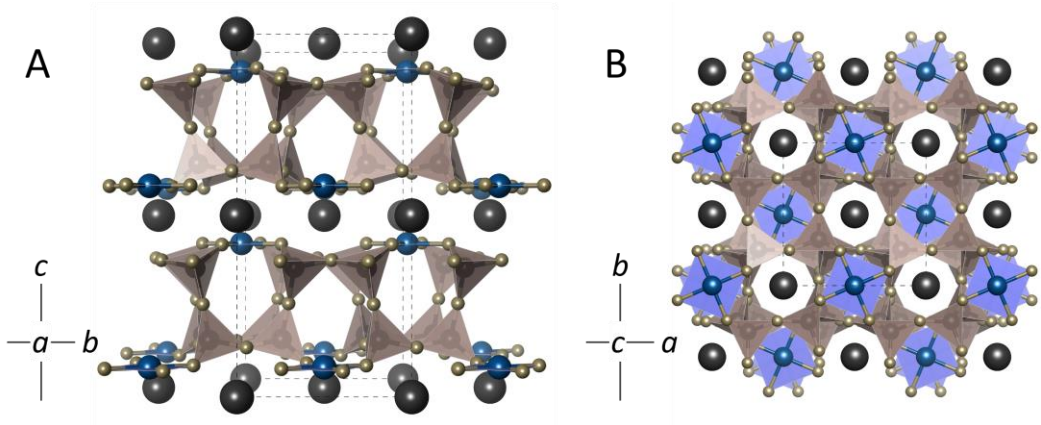

Figure 2-4 Crystal structure of $CaCuSi_4O_{10}$ viewed (**A**) along *a*-axis to display the layered silicate structure and (**B**) along *c*-axis to demonstrate D_{4h} coordination of copper ions. Black, blue, and gold balls represent Ca, Cu, and O ions, respectively. Box with dashed borders represents the tetragonal unit cell. These figures are illustrated using data from Bensch and Schur[126] (Crystallography Open Database ID: 8103941).

The blue color of $CaCuSi_4O_{10}$ comes from the Cu^{2+} ions with $3d^9$ outer electron configuration (^2D state). If placed in an octahedral ligand field (O_h), the ^2D state splits into $^2T_{2g}$ and ^2E_g states. Due to the lattice constraints and the Jahn-Teller effect, the ligand coordination is distorted into D_{4h} symmetry causing a further splitting of $^2T_{2g}$ into $^2E_g + {}^2B_{2g}$, and ^2E_g into $^2A_{1g} + {}^2B_{1g}$ (**Figure 2-5**). The $^2B_{1g} \rightarrow {}^2B_{2g}$ (~ 800 nm), $^2B_{1g} \rightarrow {}^2E_g$ (~ 630 nm) and $^2B_{1g} \rightarrow {}^2A_{1g}$ (~ 540 nm) transitions have green to red absorption, resulting in a blue coloration for EB. The NIR luminesce of $CaCuSi_4O_{10}$ originates from

the emission of the $^2B_{2g} \rightarrow {}^2B_{1g}$ transition (centered at 910 nm) with a wide stoke shift over 1000 cm^{-1}. Notably, all above-mentioned electronic transitions are intra-configuration (d-d) thus parity forbidden. The transitions are actually forced by vibronic coupling between the asymmetric lattice vibrational modes and the electronic transitions. Furthermore, this vibronic coupling has the boarding effect for the transition bands.[127,128] **Figure 2-6** shows the excitation/absorption and emission spectra of EB. This luminesce possesses an exceptionally long lifetime (107 μs, probably due to the symmetry prohibition) and an extremely high quantum yield of 10.5%.[130]

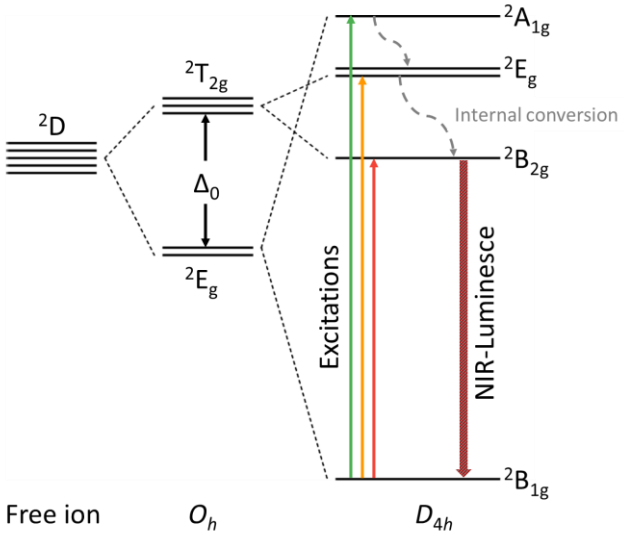

Figure 2-5 Energy levels diagram of Cu^{2+} ion with D_{4h} ligand field in $CaCuSi_4O_{10}$ lattice and the corresponding transitions. This figure is recreated based on the works of Pozza *et. al.*[128] and Warner[127].

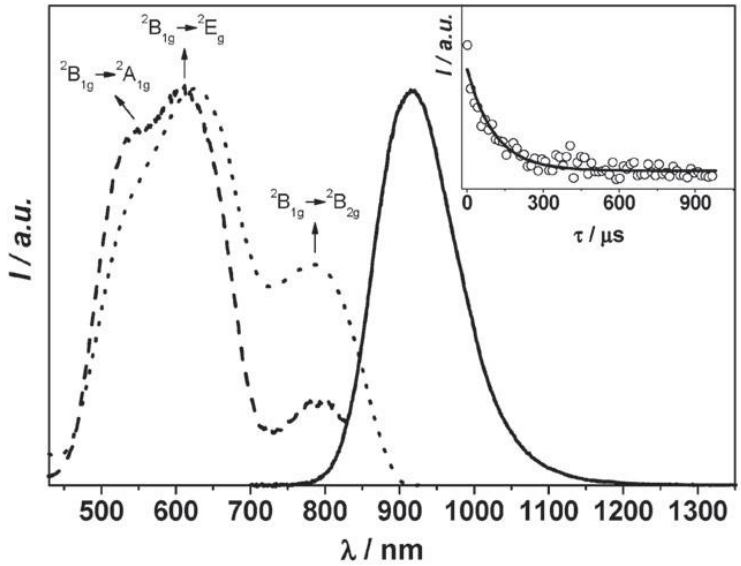

Figure 2-6 (Dotted line) absorbance, (dashed line) excitation with the maximum at 637 nm, and (solid line) emission spectra of EB bulk material. Inset: luminescence decay (107 µs, determined with excitation at 637 nm). Adapted with permission from reference[130], copyright 2009 Royal Society of Chemistry.

2.3.3 Nanoscience of Egyptian blue

The research of EB in nanoscience began in 2013, Johnson-McDaniel *et. al*. reported that $CaCuSi_4O_{10}$ crystals in EB can be delaminated into two-dimensional nanosheets by stirring EB pigment in water at 80 °C for several days. Transmission electron microscopy (TEM) (**Figure 2-7 A**) shows the as-obtained EBNS have a lateral size distribution from several hundred nanometers to several micrometers. The selected-area electron diffraction (SAED) pattern confirmed the crystals structures of EBNS: the pattern can be indexed to the (200) and (020) reflections with zone axis of [001]. Powder X-ray diffraction (XRD) data reveals the preferred orientation along {00*l*} and the cleavage along the (001) plane indicated by the diminished {*hk*0} peaks (marked peak in **Figure 2-7 B**). The EBNS still maintains the PL behavior from its bulk material (**Figure 2-7 C**). Notably, compared with bulk EB, the excitation spectra of EBNS shows a reduced intensity at 540 nm (corresponding $^2B_{1g} \rightarrow {}^2A_{1g}$ in D_{4h} environment from Cu^{2+}) indicates the decreased vibronic coupling in the 2D system. The author also points out that the increased temperature is a vital parameter for this approach: the delamination is insufficient at room temperature.[131,132]

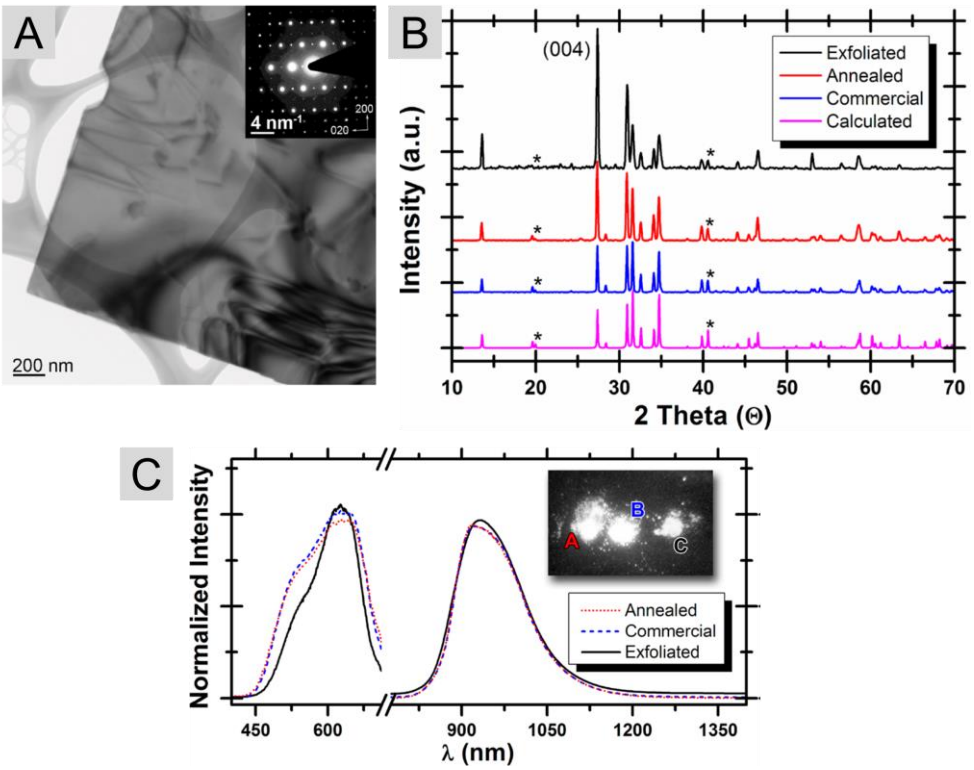

Figure 2-7 (**A**) TEM image of as-exfoliated EBNS. Inset shows the SAED pattern captured at interplanar angles of 90°. (**B**) Powder XRD data for EBNS (black line) compared with commercial EB pigment (blue line). (**C**) Excitation and emission spectra of EBNS (black solid line) and commercial bulk EB (blue dashed line) in powder state. Adapted with permission from reference[131], copyright 2013 American Chemical Society.

3

Silica-coated Magnetite Nanoparticles carrying a High-Density Polymer Brush Shell of Hydrophilic Polymer†

3.1 Preface

Integrating the properties of magnetite nanoparticles (MNPs) and high-density polymer brushes in one structure requires sophisticated synthetic designs and effective chemical approaches. In this work, a simple and versatile strategy is presented for the fabrication of hydrophilic-polymer capped magnetite-core–silica-shell nanohybrids with a well-defined structure employing reverse microemulsion technique and RAFT polymerization. The high-density polymer brush allows a precise patterning of the magnetic nanohybrids with tunable interparticle distances ranging from 20 nm to 80 nm by controlling the polymer size. The high structural precision provides a near stand-alone state of the MNPs in the nanohybrids with effectively inhibited magnetic interaction as shown by SQUID (superconducting quantum interference device) measurements.

Possessing inherently favorable superparamagnetic properties, magnetite nanoparticles (MNPs, < 20 nm) have attracted much research interest over recent years for extensive applications, e.g. magnetic resonance imaging,[133-138] drug delivery,[139-141] tumor treatment,[142-145] catalysis,[146-149]

† Adapted with permission from Cai, Y.; Peng, W.; Demeshko, S.; Tian, J.; Vana, P. *Macromolecular rapid communications* **2018**, *39*, 1800226. Copyright 2018 John Wiley and Sons.

magenetolithography,[150-152] and water purification.[153,154] In biological systems, dispersibility, the arrangement, and the interaction between MNPs play an essential role in general performances.[144,155] In magnetic hyperthermia, reducing the magnetic interaction can efficiently avoid the decrease of heating performance.[144] Surface modifications of nanoparticles are inevitably important to control and optimize these factors. Silica coating[86,156,157] of MNPs provides a chemical stable and biocompatible[133,138,158] approach. Beyond its encapsulative protection, the silica shell gives convenient access for chemical and biological functionalization for various clinical applications[159,160]. Functional polymers are heavily investigated over the last decades and have found numerous applications in nanotechnology. Applying polymer brushes as macromolecular coating provides several advantages. In general, a polymer brush shell enhances the colloidal stability of nanocomposites and offers better and tunable dispersibility in different solvent systems. For *in vivo* applications, the polymer shell often provides stealth characteristics,[155] reducing immunogenicity, toxicity, and degradation.[161] Increasing interest has been focused on the integration of different functionalities into one precise single nanostructure. In this context, a general reproducible synthetic pathway to fabricate a well-defined polymer functionalized one-to-one magnetite-silica nanostructure is highly desirable.

Previous studies[69,71] have shown that polymer-brush-grafted nanoparticles can self-assemble in a 2D hexagonal pattern on the nanoscale with tunable interparticle distance, if the polymerization is conducted in a controlled living manner. To obtain a well-defined polymeric brush on the silica surface, surface-initiated reversible addition-fragmentation chain transfer (SI-RAFT) polymerization[96] was chosen. This technique allows us to precisely control the molecular weight of the grafted polymer with narrow molar mass distributions. Our approach also provides an inherent trithiocarbonate end-group functionality at the polymer chain termini which could be used for further noble metal nanoparticle attachment[72,73] or thiol-ene chemistry[162-164] which could completely be removed[165] depending on the situation.

3.2 Results and discussion

Scheme 3-1 Synthetic scheme for the preparation of high-density PNIPAM-grafted MNP@SiO_2 nanohybrids.

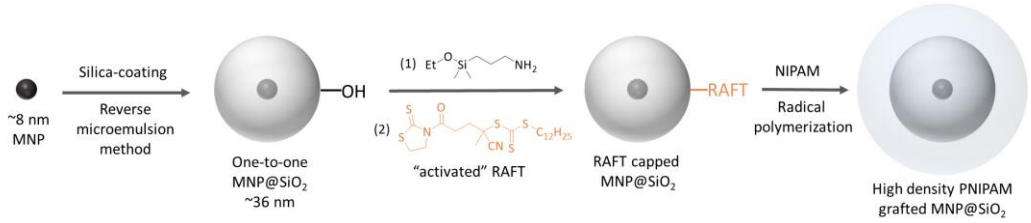

In the here presented work, we have succeeded for the first time in preparing perfectly dispersed, well-defined silica-coated MNPs (MNP@SiO_2) grafted with a hydrophilic high-density polymer brush (**Scheme 3-1**). For our study, oleylamine capped MNPs[166] (7.9 ± 1.9 nm) from a thermal decomposition method[167] were chosen as typical superparamagnetic cores. We exploited the reverse microemulsion method[86,93,157] to obtain first the silica-coated MNPs. This method enables a precise one-to-one encapsulation of MNPs with silica and fine control of the shell thickness on the nanoscale (13.9 ± 2.1 nm in this work). The size of MNP@SiO_2 is controlled to be above 30 nm (35.7 ± 3.7 nm) in consideration of potential applicability for intravenous medical applications.[139] Applying SI-RAFT polymerization from MNP@SiO_2 nanoparticles requires an efficient covalent loading of RAFT agents on the surface. We employed a two-step reaction by first modifying the surface of MNP@SiO_2 with amino moieties *via* an aminosilane and subsequently adding a RAFT agent that carries a mercaptothiazoline group, which effectively anchors to the surface-bound amino group (**Scheme 3-1**). *N*-isopropylacrylamide (NIPAM) was chosen as a reference monomer for the SI-RAFT polymerization because of its hydrophilicity, temperature-responsive properties (LCST with the occurrence of a hydrophilic to hydrophobic transition),[168] and the feasibility for *in vivo* applications.[169] The SI-RAFT polymerization was performed in dioxane with "sacrificial" free RAFT agents.[96] Further polymerization conditions with the corresponding molecular weight of the free polymer are summarized in **Table 8-1** (**Section 8.3**). This protocol was found to be very efficient and reproducible, even complete drying and high-speed centrifugation treatment cause no problems

for redispersing the RAFT-modified MNP@SiO_2 nanoparticles in dioxane. We cleaved the nanoparticle-grafted polymer by dissolving the MNP@SiO_2 with HF solution and confirmed the molar mass control for the surface-initiated polymer chains (**Figure 8-4**) for sample I and the consistence of chain lengths between free and grafted polymers[71,101]. From thermogravimetric analysis (TGA, **Figure 8-11**), the polymer grafting density was determined to be 0.50 chains per nm^2, which is in the concentrated-brush regime[170]. The PNIPAM-grafted MNP@SiO_2 can be perfectly dispersed in many polar solvents, e.g., chloroform as shown by DLS measurements (**Figure 8-5**). Simultaneously possessing uniform polymer chain length, monodispersed particle geometry, high grafting density, and perfect dispersibility, a self-assembled hexagonal pattern of MNP@SiO_2 nanoparticle with distinct spacing (**Figure 3-1**) on carbon film can be achieved by simply drop-casting the nanoparticle from chloroform onto a TEM grid. The average interparticle distance was extracted from TEM images. **Figure 3-2** shows its relationship with the number average molar mass $\bar{M}_n$ of free polymers. This dependence is comparable with our previous results[69] on gold nanoparticles using a grafting-to approach.

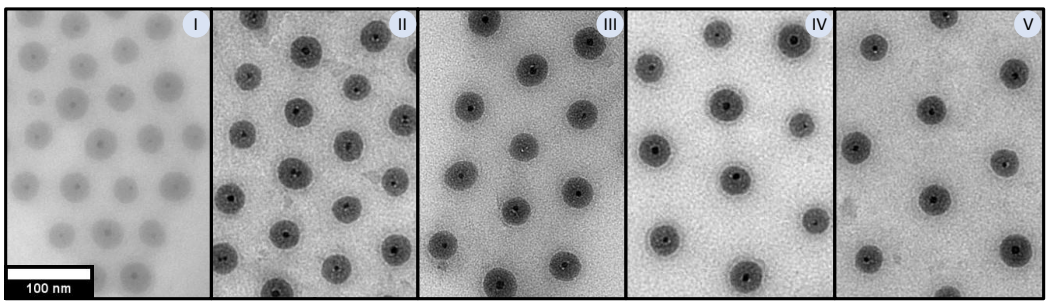

Figure 3-1 TE micrographs of PNIPAM-grafted MNP@SiO_2 for samples I to V. MNP@SiO_2 are found in hexagonal patterns with distinct spacing. TEM images with lower magnification are shown in **Section 8.3**.

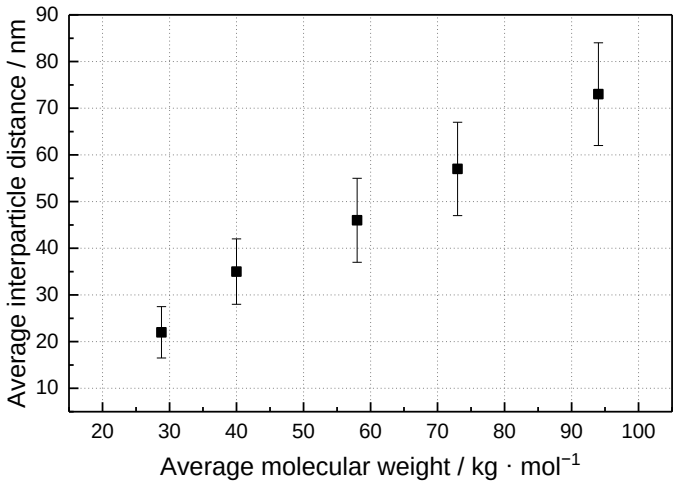

Figure 3-2 Average interparticle spacing in dependence of PNIPAM-grafted MNP@SiO_2 samples I to V *vs.* $\bar{M}_n$ of the free polymers.

Magnetic characterization of the resulting core–shell particles was performed using a SQUID (**Figure 3-3**). Owing to the well-defined structures, we were able to accomplish a coherent study of the influence of silica coating and polymer brush size on the magnetic properties and the interparticle magnetic interaction. **Figure 3-3 (a)** shows no observable hysteresis loop indicating a superparamagnetic behavior of all the samples at room temperature. The specific saturation magnetization (M_s^{sample}) decreases significantly when going from pure nanoparticles to silica-coated and finally to polymer-brush coated particles. However, if we normalize M_s to the mass of the MNPs cores, M_s^{core}, the value for MNP@SiO_2 (60.5 emu · g^{-1}) matches very well with that of the uncoated MNPs (61.0 emu · g^{-1}), showing that the decrease in the "apparent M_s" simply originates from the decreasing mass ratio of magnetite when covered with silica and grafted polymer. The zero-field-cooled/field-cooled (ZFC/FC) curves give insight into the interaction between MNPs in different samples. The significant broadening of the ZFC peak in **Figure 3-3 (b)** for the unfunctionalized MNP is not mainly caused by inhomogeneous particle size distribution, but by magnetic interactions between the particles.[171] Once the MNPs are coated with silica or further capped with polymer brush, the ZFC peak becomes narrower and the FC curve at low temperature (< 50 K) becomes convex. Both changes indicate a reduced interaction between MNPs as a consequence of their greater

distance[12]. At blocking temperature (T_B), the transition between superparamagnetism and blocked state occurs. In general, T_B decreases with increasing interparticle distances of the MNPs.[172] T_B decreases significantly from 72 K of unfunctionalized MNPs to 33 K for both coated MNPs. These results consist well with the announcements from a computational study[173]. The magnetic dipole interaction can be neglected if the MNPs are fixed in the matrix and separated from each other by a distance larger than three times their diameter (diameter = 7.9 nm, distance between MNPs > 30 nm, in our case). The above results impressively demonstrate that the magnetic dipole interaction of the MNP cores is very effectively reduced to a negligible level.

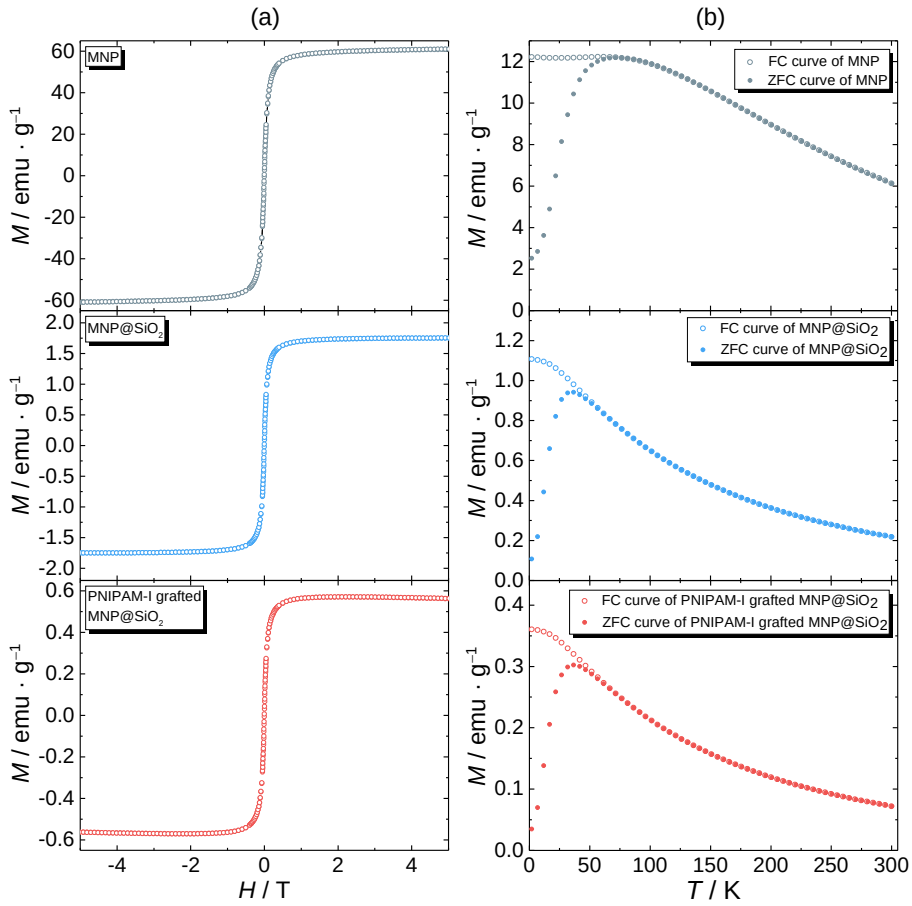

Figure 3-3 (**a**) Magnetization for MNP, MNP@SiO_2, and PNIPAM grafted MNP@SiO_2 (sample I) at room temperature. The saturation magnetization is read as 61.0, 1.75, and 0.56 emu · g^{-1} for mass normalization of the samples. (**b**) ZFC/FC measurements of the corresponding sample at H = 100 Oe.

3.3 Conclusion

In conclusion, we reported a straightforward and easy synthesis of a well-defined high-density hydrophilic PNIPAM brush-grafted MNP@SiO_2 nanohybrid with perfect dispersibility obtained by a reverse microemulsion method and SI-RAFT polymerization. We demonstrated the self-assembly ability of forming an ordered pattern of magnetic nanoparticles on the nanometer scale with tunable interparticle distances. SQUID experiments proved that magnetic interactions between MNPs are significantly reduced by a sufficient one-to-one silica coating and the subsequent polymer shielding.

4

Scalable Production and Surface Functionalization of NIR Luminescent Egyptian Blue Nanosheets

4.1 Preface

NIR fluorophores are emerging as a preferable tool for a wide range of applications in biomedical,[174-176] photonic, and optoelectronic fields.[177-180] Compared with conventional fluorophores, NIR fluorophores with emission in the range of 650–1450 nm benefit from minimized light absorption, reduced scattering, and autofluorescence from samples or environments, thus perform significantly improved signal-to-noise ratios.[174-176,181] Of particular interest is applying NIR fluorophores as sensing or imaging agents in biomedical environments for the excellent tissue penetration performance of NIR photons. These substantial advantages initiated an explosion of interest in developing diverse NIR fluorophores, such as organic dyes[182,183] metal complexes[184], quantum dots[185,186], single-walled carbon nanotubes[187,188], and lanthanide-doped nanoparticles.[174,176] Many of these intensively-studied NIR fluorophores have inherent critical drawbacks: the organic fluorophores suffer from photobleaching, the quantum dots contain highly toxic elements (e.g. cadmium, lead, arsenic)[185,186], single-walled carbon nanotubes have very low quantum yields[189], and lanthanide-doped particles often combine biotoxicity with low quantum yields[190]. With the quick development of NIR applications, the demand for a high-performance, cost-effective, and versatile NIR luminescent material rises rapidly.

Egyptian blue (EB, $CaCuSi_4O_{10}$) is the oldest (2600–2480 B.C.) artificial

pigment invented by ancient Egyptians for the presentation of their divinities.[123] Besides its intensive blue color, EB also exhibits a strong and broad near-infrared photoluminescence (excitation ~ 630 nm / emission ~ 910 nm) with exceptionally high quantum yield (10.5%), high photostability, and a very long luminescent lifetime (107 μs).[130] Besides the outstanding photoluminescence behaviors, its disparate low cost (~ 2 $/g from pigment seller) makes EB and its copper silicates family ($BaCuSi_4O_{10}$ and $SrCuSi_4O_{10}$) potential replacements for the expensive synthetic NIR materials for many modern applications. For example, Lewis *et. al.* used mechanical milling to produce micrometer-scaled EB particles as NIR fingerprint dusting powder to be unitized in the forensic application.[191]

Inconceivably, this ancient pigment still remains idle for modern NIR fluorescence applications. This unsatisfied situation is caused by two big obstacles: (i) Cracking down the size of EB into nano-level is inevitable for many applications which demand homogenous distribution of fluorescent materials in diverse solvents or matrices. (ii) The exceptionally high chemical resistance of EB hampers the study of its surface modification, which is vital to any advanced application scenario with requirements on the specific surface features. For example, the fluorescent nanomaterials used in bio-imaging often need to be surface-modified in order to adjust the physicochemical properties and for introducing biomolecules for specialized targeting.

The nanoengineering of EB started in 2013. Based on the crystal structure of EB (layered silicate), the Salguero group established a protocol to exfoliate EB bulk material into nanosheets by simply stirring EB in hot water using a glass stir bar for at least five days. The yielded EB nanosheets (EBNS) showed a thickness of several nm and a lateral diameter up to several μm.[131] A sonication method was also applied by the Salguero group to exfoliate $BaCuSi_4O_{10}$ and $SrCuSi_4O_{10}$, since the exfoliation rate of these layered silicates was found to be too low in hot water.[132] Very recently, Selvaggio *et. al.* applied this sonication method to produce EBNS.[192] However, all methods so far can only generate EBNS on mg scale and require a long fabrication time. This awful production efficiency hampers the

accessibility and usability of EBNS and extinguishes the economical utility from the bulk material. Also, the abovementioned methods lack the control on the dimension of EBNS which is crucial for modern nanoengineering: these EBNS have a very broad size-distribution containing large nanosheets up to several µm, which is unsuitable for e.g., *in vivo* applications, where larger particles (> 1 µm) must be strictly avoided to prevent blockage at the injection site. Salguero reported that the lateral dimension of these nanosheets, produced both from stirring and ultrasonication, roughly correlates with the crystallite size in the bulk starting material.[193] It is clear that the low energy input in these two methods can only separate the weakly bonded silica layers, while being ineffective for cracking down the covalently bonded structure in the lateral silicate layers of EB.

Scheme 4-1 Fabrication strategies applied in this thesis with the corresponding illustrations and photographs of (**I**) EB bulk material and (**II, III**) EBNS from different fabrication approaches.

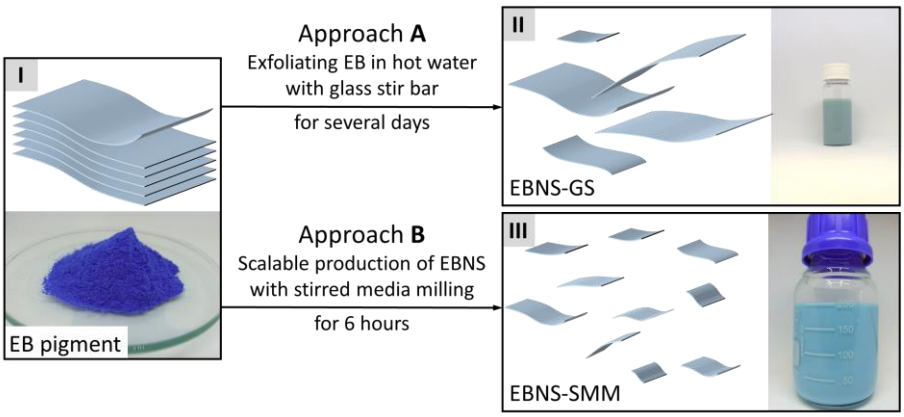

This project targeted to overcome all aforementioned shortcomings and develop a new application-oriented nanoengineering concept that fully exploits all the benefits of EB. The early stage of this project was focused on the effective production strategies of EBNS (**Scheme 4-1**): First, EBNS were produced using the protocol from Salguero's work by using a glass stir bar. Aimed at simultaneously increasing the production rate and enhancing cracking performance, the stirred media milling technique is introduced here to achieve a mass production (60 g) of EBNS within 6 hours. Owing to the high milling energy, the dimension of EBNS can be further reduced to reach a lateral size of ~ 90 nm and thickness ~ 2 nm, as confirmed by TEM

and AFM. Also, the NIR photoluminescence (PL) measurements were conducted to compare the fluorescence intensity of EBNS from both methods, revealing a decreased tendency of fluorescence intensity by reduced nanosheets' size.

Scheme 4-2 Illustration of the silica-coating and functionalization strategies on EBNS applied in this thesis.

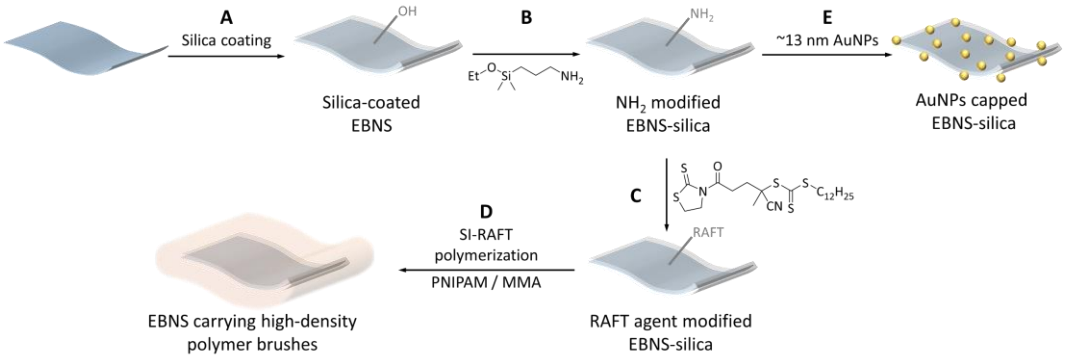

The second goal of this project is the development of surface modification for EBNS, since no surface chemistry on EB has been reported. A general strategy to fabricate silica-coated EBNS is demonstrated in this project by using an optimized Stöber process (**Scheme 4-2 A**). The outer silica shell provides the benefits of present versatile well-known chemical and biological functionalization.[76] Notably, for biological systems, silica shells can suppress the potential adverse effects from copper ions[194-196] without screening the excitation and emission photon owing to its high transparency in visible and NIR regions[196].

Finally, dense polymer brushes are brought onto the surface of silica-coated EB *via* SI-RAFT polymerization (**Scheme 4-2 B–D**). The surface-bound functional polymer brings favorable surface properties to EB such as dispersibility and enhanced colloidal stability in a wide selection of the solvent/matrix environments. Here, hydrophilic PNIPAM and hydrophobic PMMA are both successfully formed on the surface of the silica shell for EBNS. The good match of refractive index (RI) between PMMA, silica, and EBNS significantly reduced the unfavored light scattering process and thus enhanced the PL performance of the PMMA grafted EBNS material.

4.1 Development of high-efficient fabrication strategies for Egyptian blue nanosheets

In the early stage of this project, the literature-known methods are used for producing EBNS. However, during this stage, several critical drawbacks of the present methods were found (**Section 4.1.1**). With the aim of solving all the drawbacks simultaneously, a modern ball-milling technique is applied to achieve rapid fabrication of EBNS with a much smaller size (**Section 4.1.2**). However, the PL measurements indicate degeneration of emission intensity with decreasing size of EBNS. This new insight brings consideration to choosing a suitable size of EBNS for actual application scenarios (**Section 4.1.3**).

4.1.1 Reproducing and analysis of present methods for fabricating Egyptian blue nanosheets

First, the production of EBNS using the protocol from Salguero's work[197] was conducted. The exfoliation of EB is accomplished by stirring EB bulk material in 80 °C water with a glass stir bar[197]. The formation of nanosheets was confirmed: After 2 weeks of stirring, a milky blue dispersion of EBNS (**Scheme 4-1 I**) was obtained with good colloidal stability. The dried product displays pale blue-gray color (**Figure 4-10 A**). The reduced intensity of coloration in comparison with bulk material probably originates from the increased light scattering due to reduced particle size. TEM measurements (**Figure 4-1**) show the successful delamination of EB into 2D structures with a wide distribution of lateral dimension from 10 nm to 2 µm. Nanosheets (**Figure 4-1 b-c**) with crystal structures (SAED pattern, **Figure 4-1 inset**) and amorphous/polycrystalline byproducts (**Figure 4-1 d**) were observed in the sample. AFM measurements further confirmed the 2D structure of EBNS and determine the thickness of nanosheets as 4.1 ± 2.9 nm (**Figure 4-2**). Interestingly, the thickness of EBNS is almost uncorrelated with its lateral dimension. However, the statistic evaluation of lateral size is difficult using nanoscopic methods due to its very broad distribution. The size distribution

of EBNS from an exemplary micrograph (**Figure 4-2**) was conducted and gives a value of 161 ± 108 nm. Notably, this value cannot represent the whole sample.

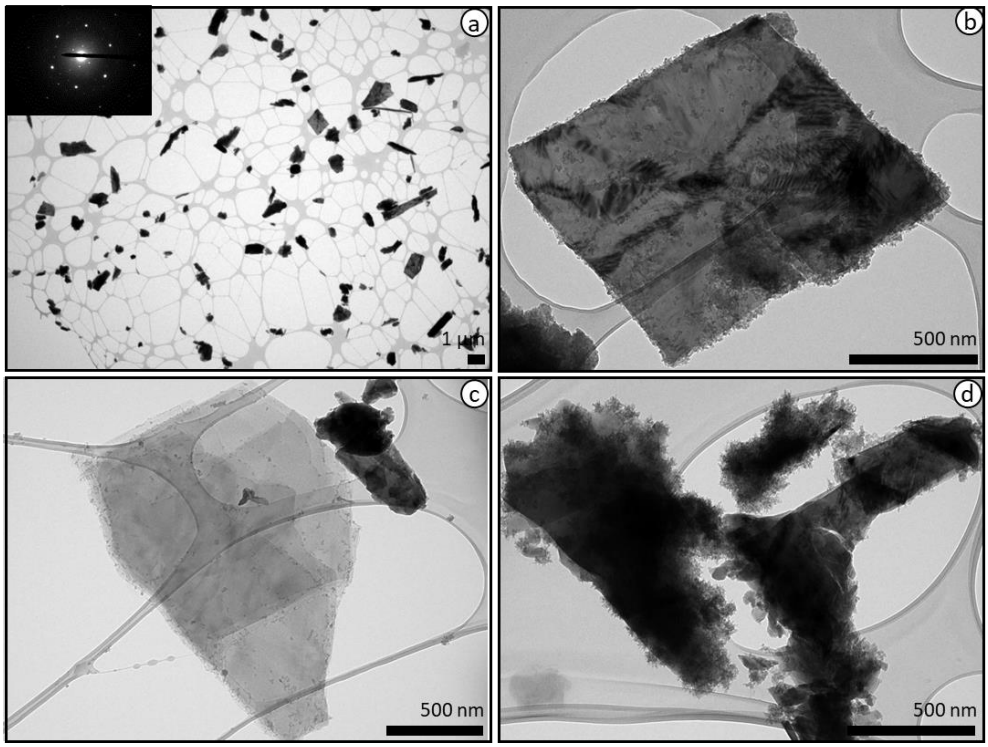

Figure 4-1 TE micrographs of exfoliated EBNS-GS in (**a**) lower and (**b-d**) higher magnification. (**b, c**) The crystal structure of EBNS with few layers on a lacey carbon film. (**d**) Some amorphous/polycrystalline parts attached to the nanosheets. Inset: SAED pattern of EB-NS crystal.

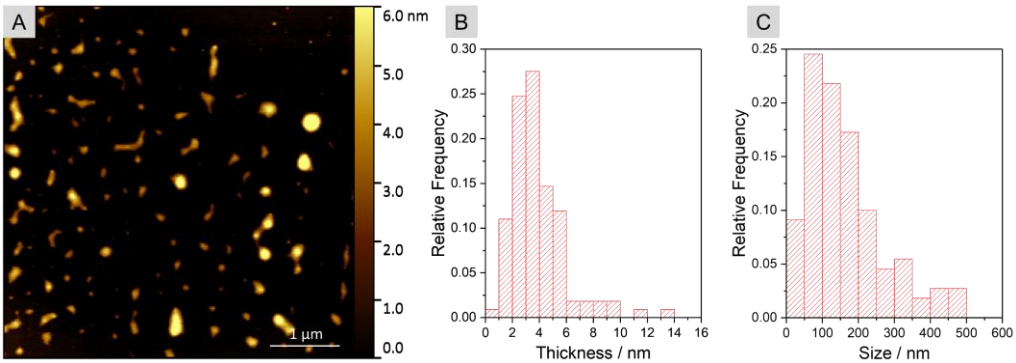

Figure 4-2 (**A**) AFM images of exfoliated EBNS-GS on a silicon wafer. (**B**) Thickness, and (**C**) lateral size distributions are evaluated from this image.

It is worth mentioning that a significant amount of glass nanoparticles is present as contamination in the product (~ 20 wt%), originating from the abrasion of the glass stir bar. As a proof, an additional blank experiment

without EB was conducted, that is, only a glass stir bar in hot water, and found that a colloid of glass nanoparticles in the range of 100 nm to several µm was formed already after 3 days of stirring (**Figure 4-3**). The tip-sonication method, on the other hand, yielded a black-colored dispersion with heavy contamination of nano-sized steel particles from the steel-made tip. Both glass and steel contaminations were unable to be chemically removed without damaging the EB (e.g., using HF) and could not be physically separated by centrifugation or filtration. It is known that the EB crystal is a very hard material (~ 5 Mohs scale[198]). In this regard, glass and steel are not suitable as contacting materials for EB. The main cause of the heavy contamination and the large size of the nanosheets should be the imperfect choice of the contacting materials and an insufficient application of energy for the cracking-down process.

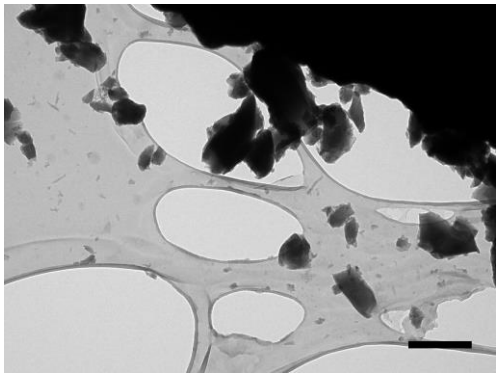

Figure 4-3 TE micrograph of glass nanoparticles formed by stirring glass stir bar in 80 °C water for 3 days. Scale bar: 500 nm.

4.1.2 Scalable production of Egyptian blue nanosheets using stirred media milling

For the scalable production of EBNS, high-energy ball milling was applied using Y_2O_3 stabilized ZrO_2 as grinding media.[199,200] In the realm of powder engineering, ZrO_2 is widely used as standard milling material, because of its high hardness and non-toxic nature. A wet-milling process in aqueous media was chosen here based on the physiochemical insight into the EB exfoliation, in which part of the weakly bonded interlayer Ca^{2+} ions need to detach from the crystal, causing the separation of the silicate layers. In this process, water should play an important role, because of its solvation power.

Stirred media milling approach was chosen for the milling procedure,[199,201,202] that offers several advantages for EBNS production. As one of the most efficient methods for producing both organic[203-205] and inorganic[199,200] nanoparticles, stirred media milling has found widespread use, e.g., in the field of pharmaceuticals, food industry, and ore processing. Compared to vibration mills or planetary ball mills, the stirred media milling method has a high potential for upscaling.[206-208] These mills are typically operated in circular mode, i.e., the suspension is pumped within a circuit through the grinding chamber. Inside the chamber, the grinding media is intensively agitated by the stirrer, causing the particles to be ground through the applied high-stress intensities. Continuous grinding is ensured by retaining the grinding media with a suitable separating device at the outlet.

In the present work, a state-of-the-art laboratory stirred media mill (PML-II, Bühler AG) was applied for this system, which provides high milling energy and the whole grinding environment is consisting of wear-resistant materials. In a typical run, around 60 g of EBNS was able to be produced using a two-step milling process. In the pre-mill step, the EB feed material was ground to ~ 1 µm, as indicated by laser diffraction analysis. In the fine-milling step, smaller milling beads were used with increased circumferential speed. The hydrodynamic radius of the EBNS was monitored during the fine milling process by dynamic light scattering (DLS) until the hydrodynamic diameter reaches a plateau of ~ 250 nm (**Figure 4-4**). A homogenous light-blue colored EBNS colloid was obtained (**Scheme 4-1 III**) with excellent dispersibility in water. The EBNS colloid can be stored over several months with only little amounts of precipitation, which can be completely redispersed within seconds by bath-type sonication or agitation. The EBNS can be easily collected by centrifugation or filtration and redispersed in water or ethanol even after drying in the oven. It is worth mentioning that the supernatant of the EBNS colloid is completely colorless after centrifugation, indicating that no copper ions are released during the milling process. Also, no significant weight gain was observed after the milling process, indicating that the milling material is not contaminating the product. The hydrodynamic size of the EBNS – as found by DLS – was approximately 250 nm, which is typically much larger than the actual size of the

nanoparticles[209]. TEM (**Figure 4-7 a**) and AFM (**Figure 4-7 b**) were used to investigate the size and thickness distribution of the yielded EBNS. TE micrographs demonstrate the impressive small lateral size of the EBNS with a complete absence of large (> 500 nm) nanosheets (**Figure 4-7 a**,**e**). The statistic evaluation on the lateral size gives a value of 90 ± 50 nm by defining the longest diagonal of the nanosheet as its diameter (the strictest rule). The relatively low contrast of EBNS in the TE micrograph also indicates the ultra-thin thickness of the yielded EBNS when comparing it with the ~ 3 nm thick carbon film substrate. The thickness of the EBNS was statistically determined *via* AFM measurements to be 2.6 ± 0.6 nm (**Figure 4-7 b**,**f**), indicating effective delamination of the EB crystals.

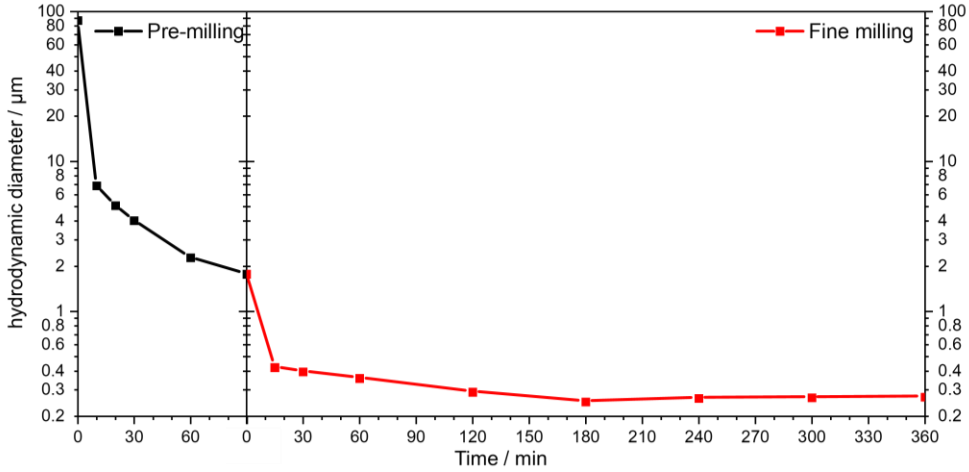

Figure 4-4 The hydrodynamic diameter of EB during the milling process as obtained *via* laser diffraction analysis and DLS. The black line is the pre-milling stage and the red line is the fine-milling stage.

4.1.3 New insights into the size-dependent photoluminescence performance of Egyptian blue nanosheets

Photoluminescence spectroscopy was performed to investigate the PL performance of EBNS yielded from diverse fabrication methods. Under the excitation with a wavelength of 637 nm, emission spectra were recorded, for EBNS from exfoliation in hot water with glass stir bar (EBNS-GS), EBNS produced with stirred media milling (EBNS-SMM), and two commercial pigment samples of EB bulk materials with different size (EB-120µm and EB-10µm, sizes are provided by pigment seller) for comparison (**Figure 4-5**).

Surprisingly, the emission of EB shows unexpected degeneration when the size of EB decreases. The extremely strong emission from EB-120µm is reduced to only ~ 20% for EB-10µm. For EBNS-GS, it remains only ~ 1% PL intensity compared with EB-120µm (despite still luminating). The final product from the high energy milling (EBNS-SMM) has lost most of its PL intensity and no emission peak can be detected using the applied set-up.

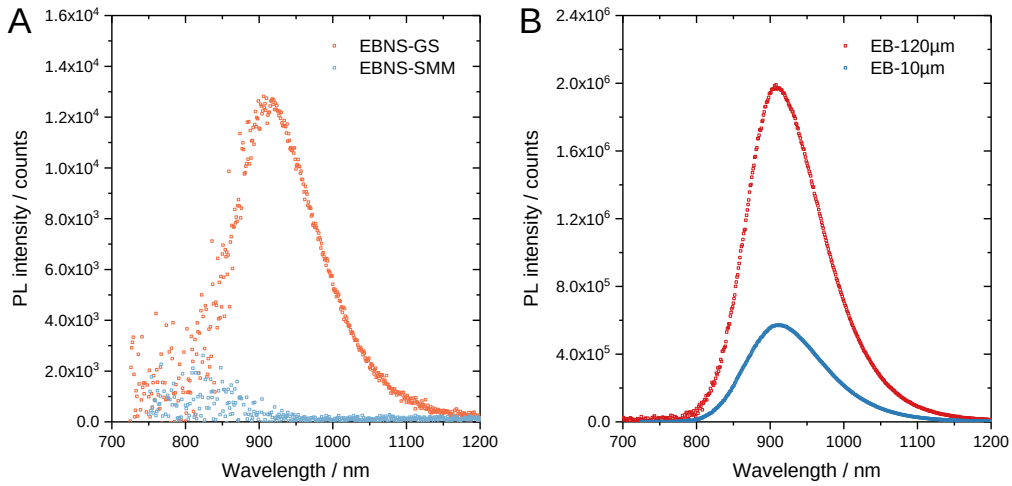

Figure 4-5 Emission spectra of (**A**) EBNS-GS, EBNS-SMM, and (**B**) EB bulk materials with the size of 120 µm and 10 µm. All samples are in powder state and measured with the same coverage area.

To understand this unexpected size effect on the PL performance of EBNS, the mechanism of NIR emission of EBNS is revisited to find a reasonable explanation. The emission of EB originates from a d-d transition ($^2B_{2g} \rightarrow {}^2B_{1g}$), which is parity forbidden but forced by the vibronic coupling between the electronic transition and the asymmetric vibrational modes in the lattice (more details can be found in **Section 2.3**). Since the number of vibrational modes is related to the size of lattice, a decreased size of EB ought to reduce the coupling between the lattice vibrational modes and the electronic transition, causing the degeneration of emission.

Now, we have seen a de facto paradox for EBNS: the final product from stirred media milling matches the size requirement for *in vivo* application while losing most of its NIR PL property. The new insight into the size-dependent NIR luminescence should never be underscored for designing any nanomaterial with EB for PL applications. The stirred media milling

technique still provides a facile approach for quick mass production of EBNS with controllable size. Furthermore, the mechanism on the size dependence must be elucidated to guide the nanoengineering on the fabrication of EBNS with envisioned PL performance.

4.2 Surface functionalization on Egyptian blue nanosheets

The absence of chemistry on the EBNS surface is another critical shortcoming of EBNS for diverse tasks. Silica-coating approach is chosen for the EBNS modification, in order to facilitate its versatile and well-studied chemical and biological functionalization options (details see **Section 2.1.2**) Here, a quick and straightforward method to fabricate silica-coated EBNS is established based on the Stöber process[74], for both EBNS-GS and EBNS-SMM. The silica coating procedure is optimized for EBNS to achieve a thin silica shell without much increase of the lateral size. The major challenge here is to avoid any aggregation of EBNS during the silica-coating reaction. First, EBNS must be perfectly dispersed into an ethanol solution containing tetraethyl orthosilicate (TEOS) and ammonia with the aid of sonication. The concentration of EBNS must be kept low (0.2 mg/mL), in order to achieve a perfect long-term dispersion of EBNS during the coating process. The formed silica-coated EBNS can be purified by centrifugation-redispersion cycles to remove any excess reactants and was finally dispersed in water.

TEM images display decisive evidence of the silica-coating of EBNS: The edges of the nanosheets become significantly smoother after coating (**Figure 4-6** for EBNS-GS; **Figure 4-7** and **Figure 4-8** for EBNS-SMM). The obtained silica-coated EBNS-SMM possesses a slightly increased lateral dimension of 110 ± 50 nm and a thickness of 7.2 ± 1.8 nm (**Figure 4-7 e-f**, determined by TEM and AFM, respectively). It should be noted here that using this approach, the thickness of EBNS can be controlled by the dosing of TEOS. Furthermore, the blank probe with the same reactant without EBNS gives

only ~ 20 nm silica nanoparticles (**Figure 4-6 d**), which is not present in the silica-coated EBNS sample. These lines of evidence confirm the silica-shell formation on the surface of EBNS.

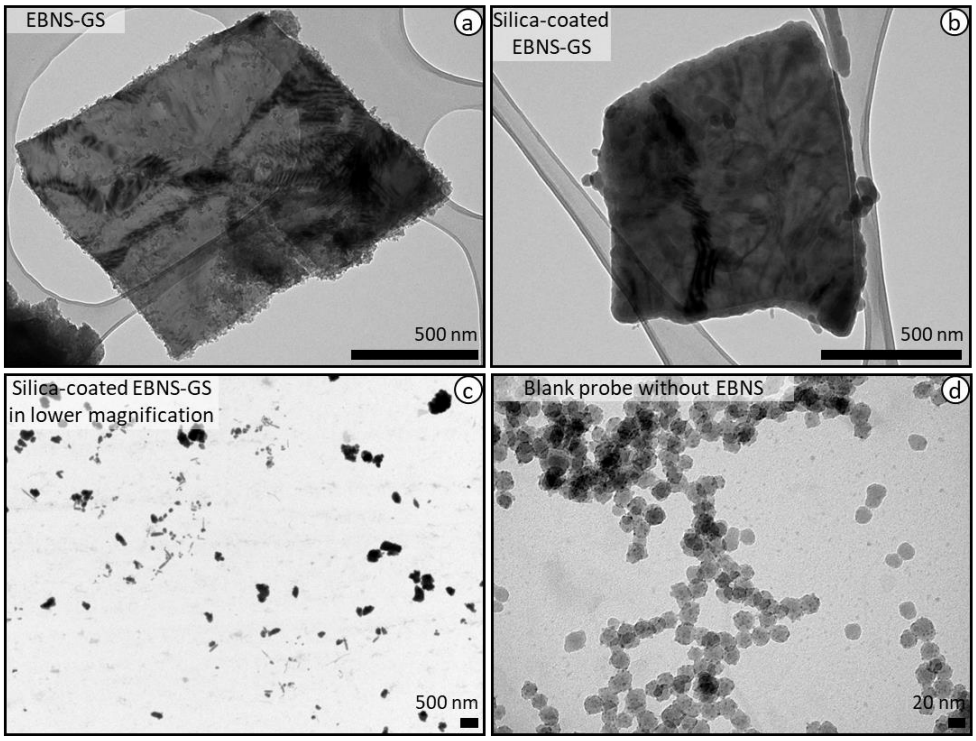

Figure 4-6 TE micrographs of (**a**) EBNS-GS and (**b**) silica-coated EBNS-GS. The significant difference in edges indicates the formation of silica shell. (**c**) Lower magnification overview of silica-coated EBNS-GS. (**d**) Blank probe without EBNS gives only ~ 20 nm silica nanoparticles.

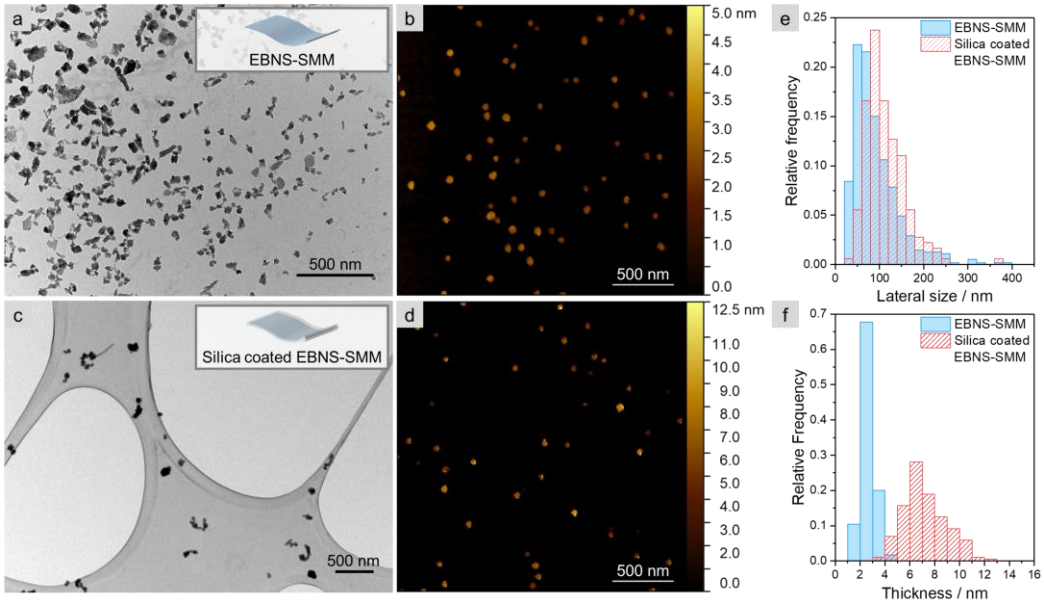

Figure 4-7 (**a**,**c**) Representative TE-micrographs and (**b**,**d**) AFM images of EBNS-SMM and silica-coated EBNS-SMM. The edge of the nanosheets becomes smoother after silica coating (TE-micrograph with higher magnification in **Figure 4-8**). (**e**) Lateral size distribution of EBNS (90 ± 50 nm, *n* = 547) and silica-coated EBNS (110 ± 50 nm, *n* = 182), determined by TE-micrographs. As mentioned in the text, the largest dimension of each nanosheet is measured for statistics. (**f**) The thickness of EBNS (2.6 ± 0.6 nm, *n* = 239) and silica-coated EBNS (7.2 ± 1.8 nm, *n* = 185), determined by AFM.

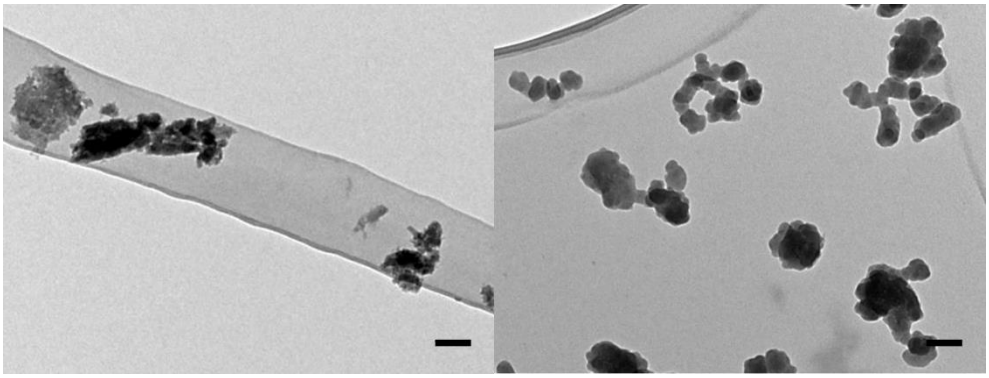

Figure 4-8 High magnification TE micrographs of (left) EBNS-SMM and (right) silica-coated EBNS-SMM. The significant difference of edges indicates the formation of silica shell. Scale bar: 100 nm.

A further surface modification with polymer brushes on silica-coated EBNS was also accomplished in this thesis. SI-RAFT polymerization – the same strategy employed in **Chapter 3** – was applied here to introduce high-density PNIPAM and PMMA brushes to silica-coated EBNS (experimental details in **Section 8.4.2**). As shown in TEM images (**Figure 4-9**), polymer

shells between EBNS can be clearly visualized, indicating the successful formation of surface-bound polymer brushes. To the best of the author's experience, the unmodified EBNS is only dispersible in protic solvents (water and ethanol). These polymer shells extend the solubility of EBNS for a large variety of solvents: EBNS carrying hydrophilic PNIPAM is dispersible in many polar solvents, including ethanol, water, acetone, chloroform, *etc*. Meanwhile, hydrophobic PMMA offers dispersibility in many organic solvents for EBNS, like toluene, THF, acetone, chloroform. Also, the PMMA-grafted EBNS can be perfectly dispersed in the PMMA polymer matrix (**Figure 8-13**).

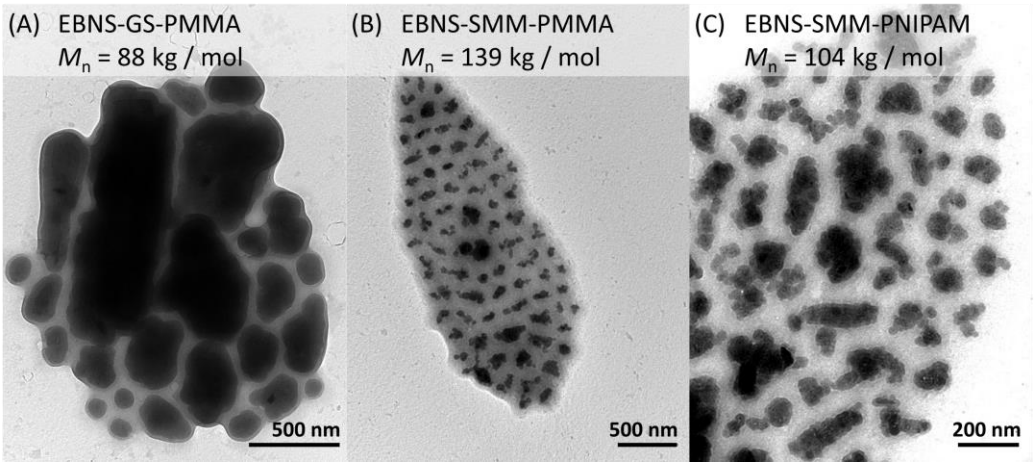

Figure 4-9 TE micrographs of silica-coated EBNS carrying polymer brushes: (**A**) PMMA ($\bar{M}_n$ = 88 kg/mol) on EBNS-GS, (**B**) PMMA ($\bar{M}_n$ = 139 kg/mol) on EBNS-SMM, and (C) PNIPAM ($\bar{M}_n$ = 104 kg/mol) on EBNS-SMM.

Moreover, polymer brushes bring their favorable functions to EBNS: the thermo-responsive property of PNIPAM could potentially open the access for EBNS to many modern nano-applications, e.g., drug-delivery,[49,210,211] hyperthermia,[210-212] catalysis,[213,214] and sensing.[215-217]

Since the NIR luminescence is the major offering of EBNS, PL-based applications are obviously the core of innovation for EBNS. For designing an optical composite material, the matching of optical properties, e.g., refractive index (RI), between each composite is vitally important: A mismatched RI causes strong light scattering on the interface between the material and causes a significant degeneration of optical out-put. PMMA is an excellent optical polymer with high RI (n = 1.489[218]) which matches well with EBNS (n = 1.633 and 1.590[125]) and silica shell (n = 1.463[219]). In this way, Silica

coated EBNS with surface-bound PMMA is designed to suppress the heavy light scattering for application as matrix-free material and dispersion in suitable environments (solvents or matrices with matched RI). In fact, PMMA functionalized EBNS exhibits significantly improved transparency in its matrix-free solid state as well as colloidal dispersion in toluene (n = 1.496) (**Figure 4-10**). Absorption spectra (**Figure 4-11**) also show consistency with this observation: The pristine EBNS in water (n = 1.333) shows only a typical profile of Rayleigh scattering without any observable absorption peak, whereas EBNS carrying PMMA display a clear absorption with a maximum at 680 nm with suppressed scattering profile. Since the light scattering process can jeopardize the light absorption of EBNS for excitation, the PL performance of EBNS is greatly improved after being modified with PMMA. **Figure 4-12** shows the emission spectra of EBNS-GS and EBNS-GS carrying PMMA measured with the same coverage area. Even if the latter one contains much lower EBNS due to the presence of silica coating and polymer shell, it still displays much stronger PL intensity than pristine EBNS.

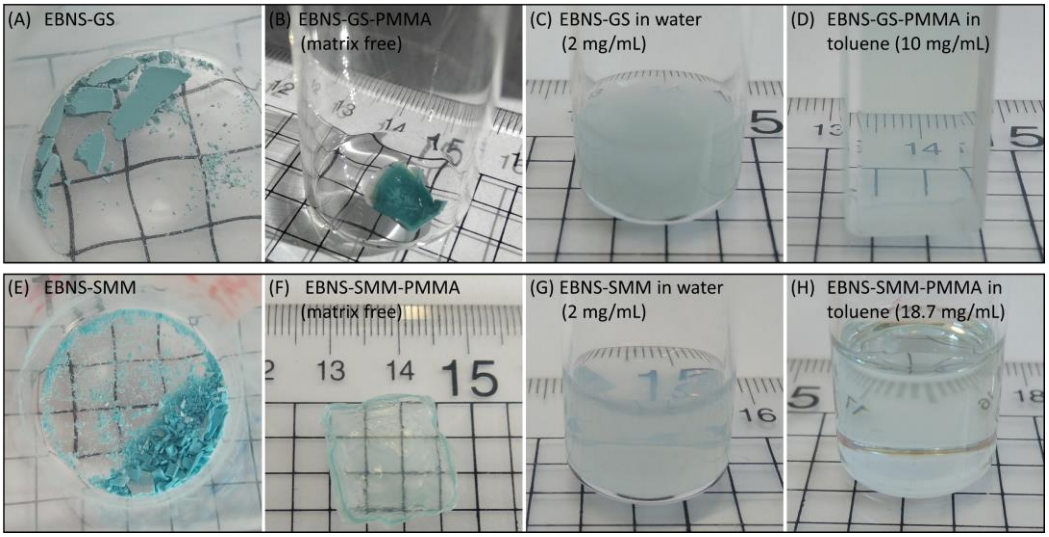

Figure 4-10 Photographs of (**A**) EBNS-GS as powder, (**B**) EBNS-GS carrying PMMA brushes ($\bar{M}_n$ = 88 kg/mol) in solid state (matrix-free), (**C**) EBNS-GS in water (2 mg/mL), (**D**) EBNS-GS carrying PMMA in toluene (10 mg /mL), (**E**) EBNS-SMM as powder, (**F**) EBNS-SMM carrying PMMA brushes ($\bar{M}_n$ = 139 kg/mol) in solid state (matrix-free), (**G**) EBNS-SMM in water (2 mg/mL), and (**H**) EBNS-SMM carrying PMMA brushes in toluene (18.7 mg/mL).

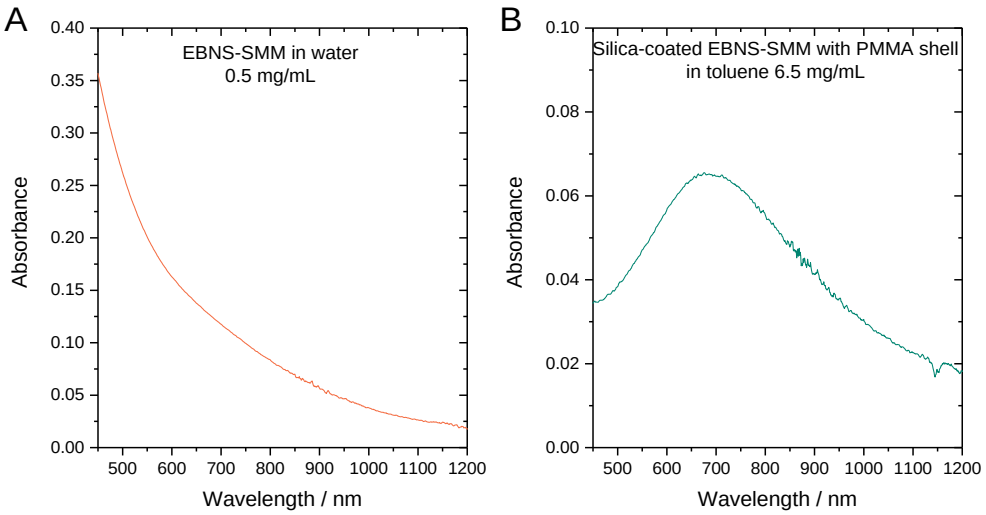

Figure 4-11 Absorption spectra measured by UV-Vis-NIR spectrophotometer of (**A**) EBNS-SMM dispersion in water (0.5 mg/mL) and (**B**) PMMA grafted EBNS-SMM in toluene (6.5 mg/mL).

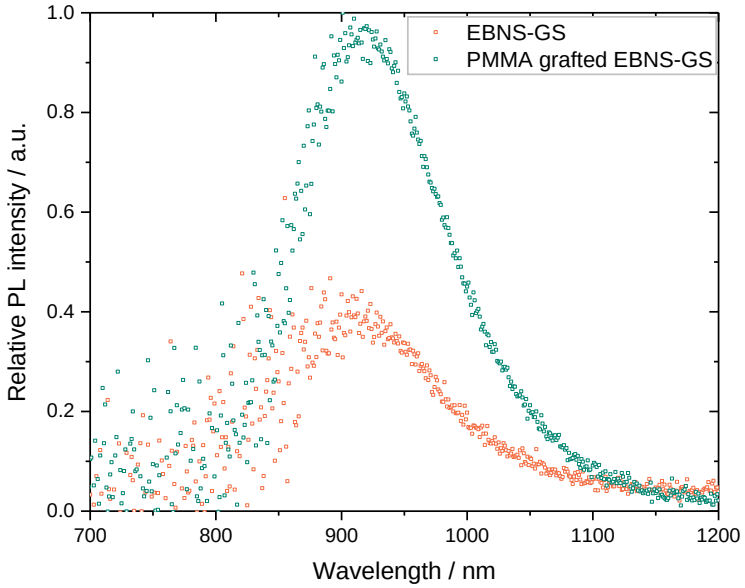

Figure 4-12 Emission spectra of EBNS-GS and PMMA grafted EBNS-GS in solid-state. Measurements are conducted with the same coverage area.

The interaction of fluorescent material with plasmonic nanoparticles often brings intriguing fluorescence energy transfer affairs which can be used as sensor applications.[220-222] Furthermore, the localized surface plasmon resonance of AuNPs is well-known for their ability to enhance fluorescence strength as the light-harvesting antenna,[223-226] which is also an incentive for

the case of EBNS. AuNPs can also be used as hot spots for introducing further functional molecules with sulfur-containing moieties for more advanced tasks.[227,228] For EBNS, a prototype of AuNPs attached EBNS is fabricated as a proof-of-concept platform for future study on these topics.

For doing so, AuNPs can be attached onto the surface of NH_2-covered EBNS-silica, by taking advantage of the strong aurophilicity of the NH_2 groups. First, silica-coated EBNS was surface-modified with NH_2 groups. The self-assembly process was carried out by adding a specific amount of citrate capped ~ 13 nm AuNPs in aqueous sol to the NH_2-functionalized EBNS-silica colloid. TEM images (**Figure 4-13**) show the successful formation of the well-defined AuNPs-EBNS nanohybrid. Notably, the distance between EBNS and AuNPs can be precisely tuned by the thickness of the silica shell between them.

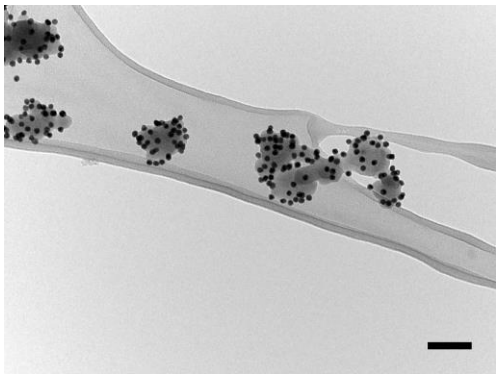

Figure 4-13 TE-micrograph of NH_2-covered EBNS-silica with AuNPs attached on its surface. Scale bar = 100 nm.

4.3 Conclusion

In summary, a state-of-the-art method for the mass production of Egyptian Blue nanosheets is established. For the first time, the size of EBNS has been reduced to sub 100 nm. The degeneration of PL performance with reduced size of EBNS is discovered. This new knowledge provides an important perspective for choosing a suitable size of EBNS for detailed applications requirements. This work further demonstrated the first chemical modification of the EBNS surface by coating EBNS with a thin silica

shell. The silica-coated EBNS is a very flexible platform for introducing further functional groups, e.g., biomolecules, polymers, or groups for constructing nanocomposites. Two types of polymers: hydrophilic PNIPAM and hydrophilic PMMA brushes are introduced onto the surface of silica capped EBNS, integrating their dispersibility and functions to EBNS. AuNPs were attached to the surface *via* a self-assembly process.

5

Circular Nanopattern of AuNPs Mediated by Colloidal Self-assembly Process

5.1 Preface

Surface patterned noble metal NPs have been a fundamental tool for nanotechnology with a wide field of application including sensing,[52-55] metal-assisted chemical etching,[56,57] superhydrophobic coating,[58] and biomedical research.[59-62] The innovation on the surface nanopattern always brings new intriguing features to the surface properties and induces breakthroughs in functional surface engineering.

To the date of this thesis, assembly of NPs in diverse geometrical patterns using a wide range of tools is available including block-copolymer self-assembly,[229] beam-lithography template,[230] dip-pen nanolithography,[231] DNA molds,[232] polymer-grafted NPs,[69,71,80] *etc*. Using these methods, a large variety including densely packed monolayers,[233-235] hexagonal-spaced patterns,[63,68,69,80,236,237] and 1D linear assemblies[64,237-240] can be achieved. However, these methods were using single NPs as a patterning unit. The tools to create advanced "nano-pixels" for nanopatterning barely exist. Here, this thesis created a new type of such "nano-pixel" unit: circular-patterned AuNPs.

Scheme 5-1 Schematic representation of fabrication strategy for silica-core–AuNPs-satellite nanoassemblies and 2D AuNPs nanopattern. PEG-shell on AuNPs is omitted for clarity.

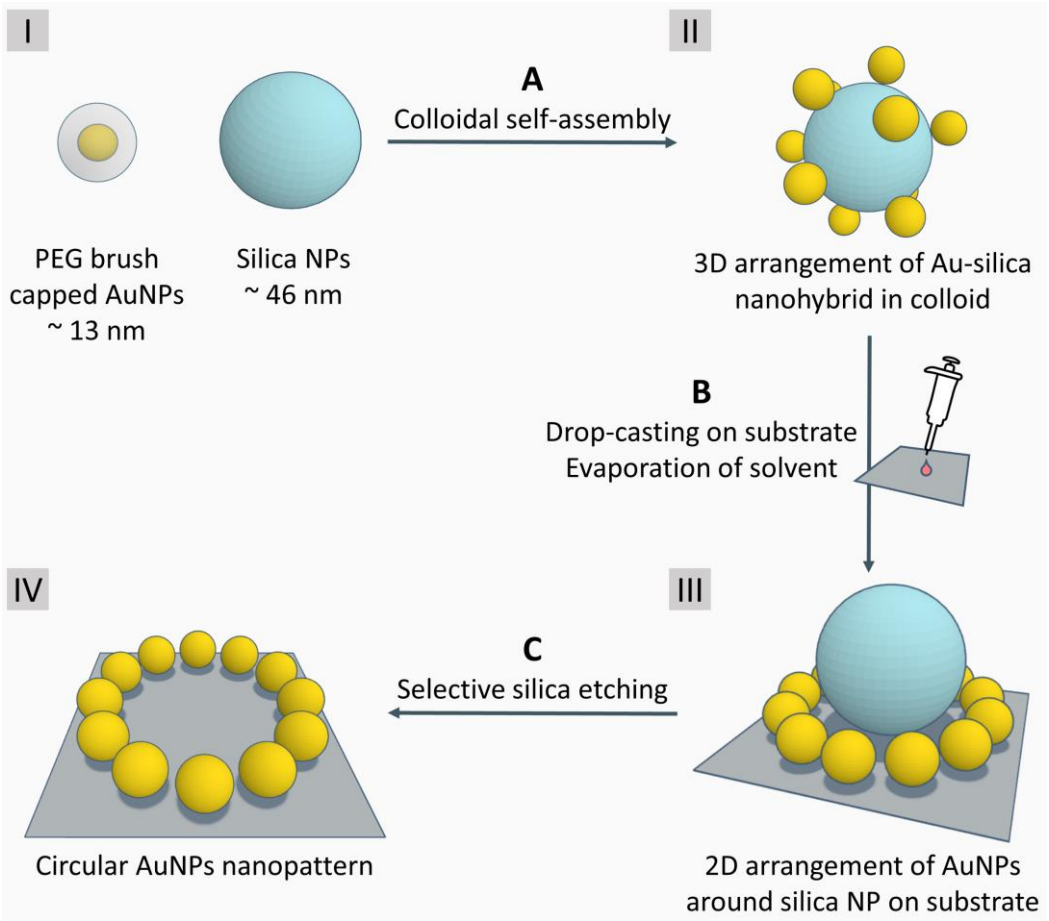

For doing this, a very straightforward method to fabricate a ~ 70 nm circular pattern of ~ 13 nm AuNPs using ~ 46 nm silica NPs as temporary templates is established (**Scheme 5-1**). AuNPs covered with PEG brushes were fabricated by a grafting-to approach using thiol terminated PEG. Although the strong affinity of PEG onto the surface of silica is well-known in the literature,[241,242] the author first discovered that by mixing PEG capped AuNPs (PEG-AuNPs) with silica NPs in THF, a core–satellite nanostructure (**Scheme 5-1 II**) is formed by a self-assembly process. Once the silica-gold nanoassemblies are cast on a substrate, the AuNPs tend to arrange themselves around silica NPs into a 2D circular pattern (**Scheme 5-1 III**).

In order to remove the silica NP templates without any disordering of the precise arrangement of AuNPs, an etching procedure by incubating the

surface in 10wt% aqueous NaOH solution has been proved to be perfect for the purpose. The extraordinarily high concentration of NaOH servers two functions simultaneously. It first provides a high etching performance for silica NPs. The secondary function for applying a high concentration of NaOH is to immobilize AuNPs on the substrate: the solubility of the PEG shell on AuNPs reduces dramatically on high ionic strength.

In this project, the PEG shell on AuNPs fulfills several important roles at the same time including (i) enhanced colloidal stability, (ii) extended solvent adaptability for AuNPs, (iii) linker between AuNPs and silica NPs, and (iv) a protective shield to avoid any movement of AuNPs during the etching process.

5.2 Fabrication of PEG brushes grafted AuNPs

This section focuses on the fabrication of core–shell like structure of PEG brush capped AuNPs. There is a great variety of methods to introduce dense polymer brushes onto the surface of NPs. Here, one of the most straightforward approaches to obtain AuNPs-PEG is applied: an excess of commercially available thiol terminated methoxy PEG ($\bar{M}_n$ = 6000 g/mol) was added into an aqueous colloid of AuNPs. The thiol groups have strong aurophilicity by forming Au-S covalent bonds with a binding energy of 170 kJ/mol.[243] In this way, thiol end groups act here as effective covalent anchoring moieties for immobilizing PEG polymer brushes onto the surface of AuNPs.

Notably, the excess of PEG must be removed before the next step since free PEG also has a strong affinity towards the surface of silica NPs causing a passivation effect for silica and potentially jeopardizing the formation of Au-silica nanohybrids. Multiple (> 3) centrifugation/redispersion cycles were employed here to ensure sufficient purification.

The TE micrograph of PEG-AuNPs is shown in **Figure 5-1**. It can be clearly seen that the AuNPs with PEG shells have an increased interparticle distance. This indicates the formation of a dense polymer shell on the surface of AuNPs. The purified PEG-AuNPs are stocked under ambient conditions

and used as a stock solution. The detailed experimental procedure can be found in **Section 8.5**.

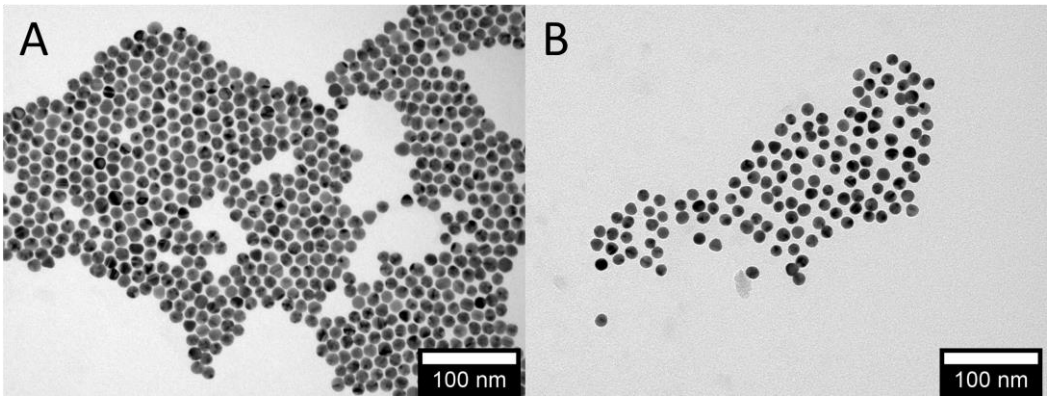

Figure 5-1 Exemplary TE micrographs of (**A**) citrate capped AuNPs and (**B**) PEG capped AuNPs.

5.3 Colloidal self-assembly of silica-core–AuNPs-satellite nanostructure

To create an ordered 2D pattern of NPs on the substrate, both interparticle interaction and substrate–nanoparticle interaction must be tuned to enable the precise arrangement of NPs. On this topic, surface-bound polymer brushes offer strong and flexible control for the detailed interaction mentioned above.[69,71,80]

To form a hierarchical core–satellite nanostructure, the connection between both nanocomponents is vitally important. To the best of the author's knowledge, the design of the linker always contains one or more strong anchoring moieties.[72,73,244] In this project, the adsorption between PEG chains (on AuNPs) and silica surface serves as the driving force which guides the colloidal self-assembly process of PEG-AuNPs and silica NPs under suitable conditions. In other words, no specific anchoring moiety design is required for self-assembly.

Since the size of silica directly defines the diameter of the circular pattern of AuNPs, for the optimal patterning performance, ~ 46 nm silica

with very high roundness was chosen as the template. The self-assembly of silica NPs and PEG-AuNPs in colloid was conducted in THF at room temperature by simply mixing and incubation. Parameters including the ratio of AuNPs to silica NPs, concentration, and incubation time must be precisely controlled to achieve a well-defined core–satellite nanostructure without aggregation and unbound AuNPs. In general, long incubation time (> 4 days) and precise dosing of AuNPs are required for a successful self-assembly process. The ratio of silica/AuNPs is a crucial parameter for the successful self-assembly process with the best visual appearance of the yielded nanopattern. Low dosing of AuNPs induces an instant formation of aggregation, which is caused by insufficient coverage of silica with PEG: the free silica surface can further interact with PEG-AuNPs adsorbed on the other silica NPs forming the cross-linking (aggregation) of the NPs. The optimized conditions are described in detail in **Section 8.5**.

After incubation, the colloid is directly drop-casted on a lacey carbon film covered TEM grid for TEM analysis. **Figure 5-2** shows the TE micrograph of the silica-gold nanohybrid: interestingly, the AuNPs are arranged closely to the surface of silica NPs in a clear 2D circular pattern. In fact, the arrangement of AuNPs on the surface of silica should be an isotropic distribution, as illustrated in **Scheme 5-1 II**, since no anisotropic interaction forming a circular arrangement is present in the colloid. It can be also extracted from the unchanged color of the colloid during the self-assembly process that the plasmonic coupling between AuNPs is not significantly present in the colloidal Au-silica nanostructure. This further indicates the distance between each AuNPs should be much larger than the distance observed in the 2D TEM images. In summary, the 3D arrangement of AuNPs in colloid is the only rational picture that supports all the experimental observations.

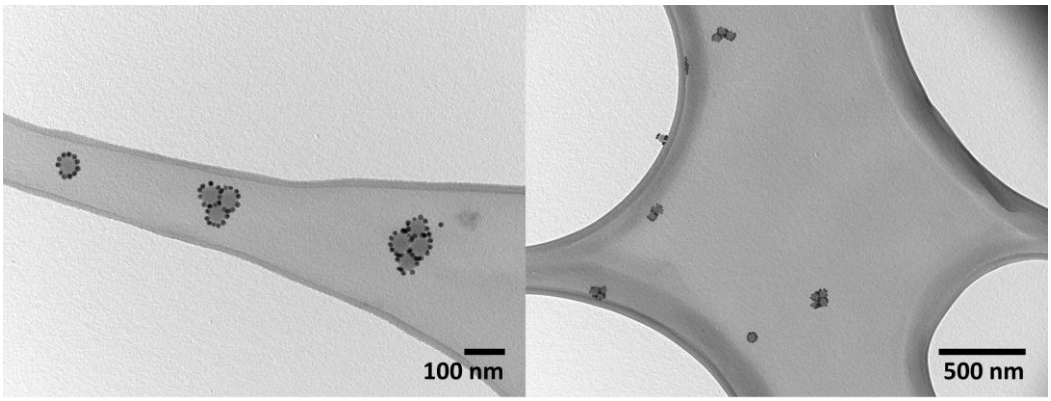

Figure 5-2 TE micrograph of 2D arrangement of silica-Au nanohybrids on a lacey carbon film covered TEM gird.

The formation of 2D circular distributed AuNPs should be originated from the interaction between core–satellite nanostructures with the substrate. As illustrated in **Scheme 5-1 III**, such positioning of AuNPs could provide the optimal contact between AuNPs, silica NP and substrate to minimize the surface energy.

The detailed dynamic process of transition of AuNPs arrangement from 3D (colloidal) to 2D (on the substrate) is highly incentive. Although this transition cannot be visualized in the frame of this thesis, such dramatic change indicates a reasonable assumption of mobile of AuNPs on the surface of silica NPs: the perfect arrangement of AuNPs around silica NPs support the hypothesis of a surface drifting of PEG capped AuNPs on the surface of silica. **Scheme 5-2** illustrates the pathway of AuNPs moving from the top position to the final "parking" position. The length of the pathway is 62 nm exceeding the contour length (at maximum physically possible extension) of PEG (~ 36 nm for 6000 g/mol, calculated based on the ethylene glycol unit length of 0.28 nm[245]). The flexible mobility of the PEG-AuNPs can be explained by the reversible adsorption interaction between PEG and the silica surface. Further evidence and mechanism of this intriguing surface drifting event must be studied in more detail in the future.

Scheme 5-2 Schematic illustration to stimulate the pathway of a AuNP moving from the top position to the final "parking" position.

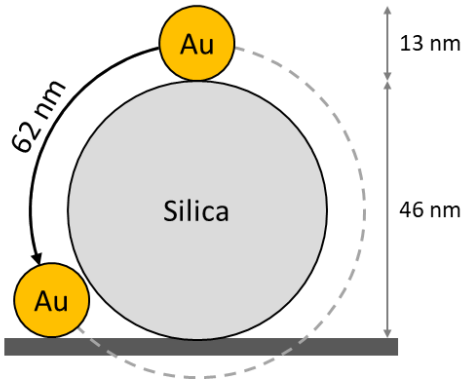

5.4 Optimizing selective etching of silica NPs: perfect circular AuNPs pattern

The last step between the silica-gold core–satellite nanostructure and the desired circular AuNPs pattern is the well-controlled etching of silica NPs without affecting the arrangement of AuNPs. There are several available options for silica etching, especially for nanoparticles, including HF,[80,246] alkaline solution,[92,247] and even hot water.[248] The obvious concern here is the dissociation of PEG-AuNPs during the etching process for its excellent water dispersibility. This concern turns out to be the real challenge: attempts made with 1 wt% NaOH, which is a widely-used protocol for etching silica NPs in the colloid.[92] At room temperature, no visible etching of silica NPs on the substrate can be observed. At raised temperatures (50 °C and 85 °C), silica was successfully removed at the cost of disordering the AuNPs circular pattern (**Figure 5-4 E–F**). These combined results show that immobilizing PEG-AuNPs on the substrate during the etching process is the major challenge in this step.

The turning point comes with the rising concentration of NaOH. The solubility of PEG ($\bar{M}_n$ = 6000, same as the PEG used in this project) is strongly dependent on the concentration of NaOH in an aqueous solution and decreases upon rising temperature (**Figure 5-3**).[249] With this knowledge, an

etching condition is designed using a highly concentrated NaOH solution under elevated temperature: PEG is rendered insoluble while the etching of silica should proceed rapidly.

The finalized etching protocol is very straightforward: The substrate decorated with silica-gold nanostructure was incubated in 10 wt% NaOH solution at increased temperature (50 °C and 85 °C) for 30 minutes, and then quickly dipped in water and ethanol successively to remove residual NaOH. This etching condition allows the complete removal of silica NPs while keeping the perfect circular pattern of AuNPs (**Figure 5-4 D**). The inside diameter of the AuNPs cycle matches perfectly with the silica NP template. The AuNPs are arranged with high order and short interparticle distance, strong plasmonic coupling between AuNPs should be occurring within such closely packed structures.[67,250-254] This makes the circular AuNPs potentially a unique surface patterning unit with a plasmonic hotspot character.

The temperature also plays a key role here: at room temperature, the etching process takes up to 20 hours to completely remove silica NPs (**Figure 5-4 A–B**) while the whole process takes less than 30 minutes at 50 °C and 85 °C (**Figure 5-4 C–D**). The disordering of AuNPs is significantly less pronounced in the samples that underwent high-temperature etching (both 50 °C and 85 °C) using 10 wt% NaOH. This behavior also meets the temperature-dependent solubility of PEG in NaOH (**Figure 5-3**).

On this topic, the colloidal behaviors of PEG capped AuNPs in pure water, 1 wt% NaOH and 10 wt% NaOH solution were studied with DLS at different temperatures, respectively, to confirm the change of dispersibility of PEG-AuNPs under diverse etching conditions. **Figure 5-5** shows that the PEG-AuNPs can be perfectly dispersed in both water and 1 wt% NaOH in the whole temperature range. The decreasing hydrodynamic diameter under higher temperatures results from the thermal release of solvent molecules (entropic effect).[255-257] However, in 10 wt% NaOH, nano-agglomeration forms at room temperature and 50 °C with increased hydrodynamic diameter; at 85 °C, a complete precipitation can be observed (**Figure 5-5** insert pictures). The DLS results impressively demonstrate that the poor dispersibility of PEG-AuNPs in 10 wt% NaOH solution is the cause of the

immobilization effect of PEG-AuNPs during the etching process, which is the prerequisite for the desired etching result.

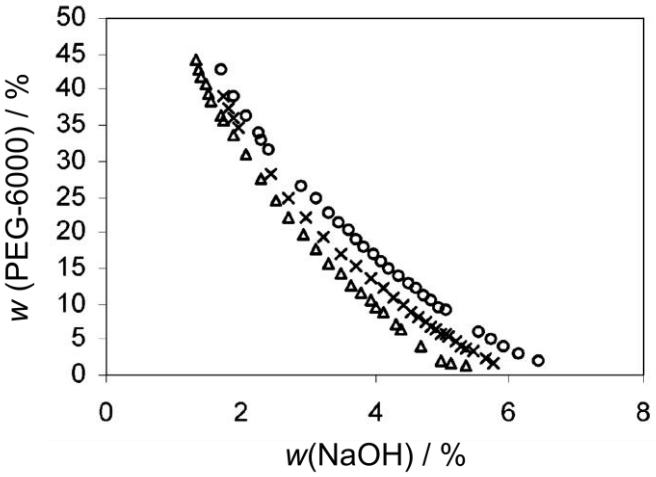

Figure 5-3 Binodal curves for the PEG ($\bar{M}_n$ = 6000) in aqueous NaOH system at different temperatures: (cycles) 25 °C; (cross) 35 °C; (triangle) 45°C. Adapted with permission from reference[249], copyright 2004 American Chemical Society.

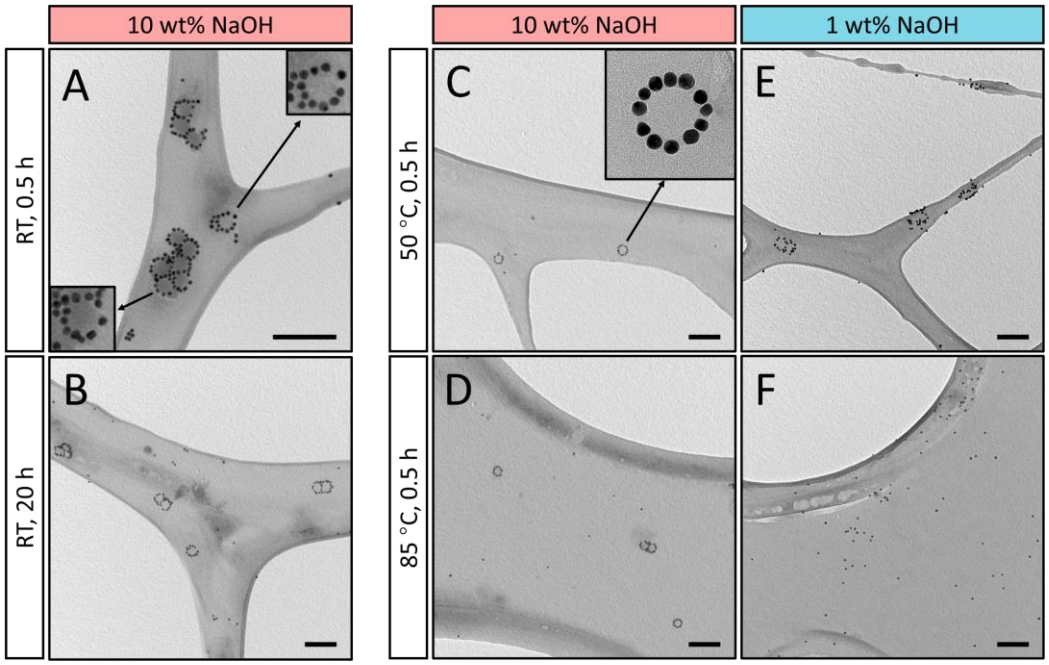

Figure 5-4 TE micrograph of circular AuNPs after different etching conditions. In **A**, most silica NPs still remain visible while few of them are completely removed (marked positions). In the sample of **B-F**, no silica NPs are visible in the whole sample. Scale bar = 200 nm.

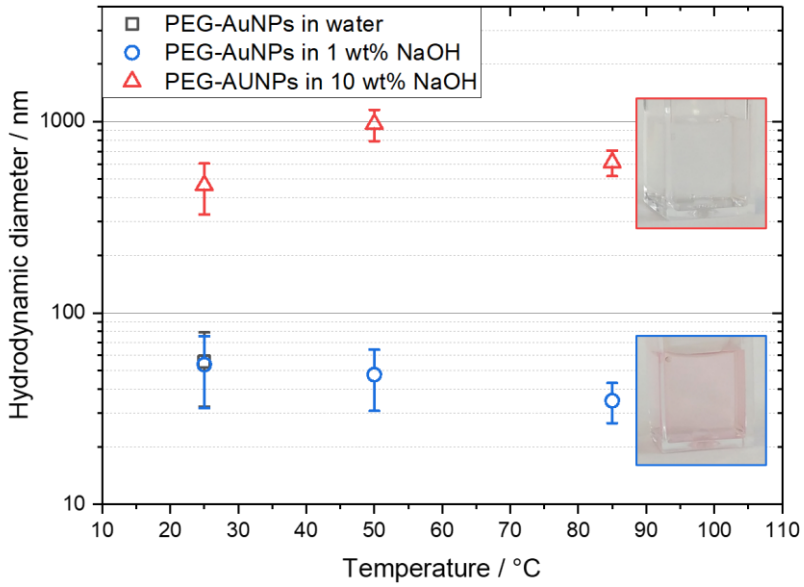

Figure 5-5 Hydrodynamic diameter from DLS measurements for 0.01 mg/mL PEG-AuNPs in water, 1 wt% NaOH aq., and 10 wt% NaOH aq. at different temperatures (25 °C, 50 °C, and 85 °C). Detailed distributions are shown in **Figure 8-16**. Insert pictures represent the states of PEG-AuNPs colloid in 1 wt% and 10 wt% NaOH aq. after heated at 85 °C.

5.5 Conclusion

In this chapter, a perfect circular pattern of AuNPs is created by selective etching of silica from a silica-core–Au-satellite nanostructure on the substrate. The core–satellite nanostructure is fabricated by colloidal self-assembly of PEG capped AuNPs with silica NPs using the strong adsorption of the PEG chains on the silica surface. The highlight of the etching process includes the judicious utilization of reduced solubility of PEG at a very high NaOH concentration and increased temperature to immobilize the circular pattern of PEG-AuNPs during the etching process.

The power of this approach also includes the potential flexible choice of patterning nanoparticles. The circular patterning of AuNPs is demonstrated in this thesis. However, the whole self-assembly process and etching protocol do not utilize any properties from the AuNPs. The author believes that the interchange of AuNP with any NP which has the access to form PEG shell and

is tolerant towards alkalic conditions should also result in a similar pattern. The inside diameter of the circular AuNPs pattern originates directly from the diameter of the silica template which can be precisely tuned over a wide range. In the present thesis, the chain length of the grafted polymer is not varied. However, diversifying the chain length of the capping PEG has a strong potential to change the circular pattern of AuNPs. These topics will be studied in more detail in future works.

In this stage, only carbon film is applied as the substrate for convenient access to TEM analysis. The incentive next step is to bring the circular pattern onto other types of surfaces and even in a well-defined monolayer using coating techniques like dip-coating or spin-coating. Notably, the polymer content can be removed by applying plasma treatment to expose the Au surface for further chemical or biological modifications.

6

AuNPs Covered Silica Nanoparticles Mimicking Hollow Gold Nanostructure for Enhancement of Phase-contrast CT Imaging

6.1 Preface

Phase-contrast computed tomography (CT) visualizes the phase shift experienced by the X-ray and can provide images with enhanced contrast in comparison to conventional absorption-based CT.[258] For imaging of soft tissues, the usage of contrast agents is inevitable for biological researches and clinical applications. On this topic, various types of contrast agents based on diverse materials containing heavy atoms, e.g., iodinated materials,[259,260] AuNPs,[261-263] $BaSO_4$, have been developed to increase the CT contrast.

Besides the choice of material, the 3D geometry of the nanomaterial is also an important design option for the phase-contrast CT experiment. It is known that spherical objects (e.g., micro bubble) have advantages for this task due to their high scattering properties: the hollow sphere refracts X-ray acting as a tiny lens.[264] As the consequence of multiple refractions caused by the population of microbubbles, the X-ray can be scattered in many directions and generates an area contrast.[265]

Following this line of thought, creating a hollow gold sphere could also offer an enhancement of the phase-contrast CT signal. Although the hollow AuNPs can be synthesized using a multi-step synthesis,[49,266,267] the yield of these syntheses is by far insufficient to meet the realistic dosing of a single *in*

vivo experiment (quick injection of ~ 1 mL colloid containing 100 mgAu/mL). Under this context, mimicking a hollow gold sphere becomes a feasible solution. For doing so, thiol functionalized 37 nm silica is fabricated and applied as a functional template to capture ~ 5 nm AuNPs on its surface forming a core–satellite nanostructure (**Scheme 6-1**). This nanostructure has a spherical layered arrangement of AuNPs which perfectly meet the geometrical requirement for mimicking hollow AuNPs for CT experiments. For a comparison experiment, the "solid" AuNPs are fabricated using ~ 13 nm AuNPs. The choice of this diameter is based on the consideration that both "hollow" and "solid" nanostructure should provide a similar thickness of Au for X-ray penetration. For long-term colloidal stability and bio-combability, both nanostructures are capped with PEG.

This project is in cooperation with Max Planck Institute for Experimental Medicine. Both samples must be injected with the same known Au-content (1 mL of 100 mgAu/mL, for a comparison purpose) into the living mice for *in vivo* lung imaging. The major challenges include the upscaled production of both "hollow" and "solid" AuNPs with precise quality control of the product. Effective fabrication routes for both nanostructures must be established, with the upscaled production of both types of AuNPs components. The purification/concentration steps must be optimized to achieve the ultra-high gold concentration in an aqueous colloid. A quantitative analysis method with high sensitivity and precision for the determination of Au content in the final product is also established by measuring UV-Vis absorption of $HAuCl_4$ converted from the AuNPs.

Scheme 6-1 Schematic representations of (**A**) "solid" AuNP as the reference sample and (**B**) "hollow" AuNP sample. Yellow, grey, red, and light blue color represent AuNPs, silica NPs, thiol anchoring groups on the silica surface, and surface grafted PEG polymer, respectively.

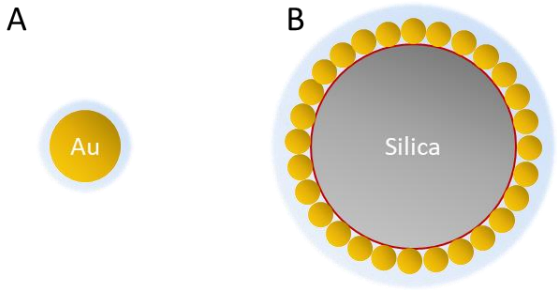

6.2 Results and discussion

To construct well-defined core–satellite nanostructures in the most efficient route (as illustrated in **Scheme 6-2**), we first synthesized 37 nm spherical silica NPs using the reversed microemulsion method. The surface of the silica NPs was then directly modified with thiol groups by adding (3-mercaptopropyl)trimethoxysilane *in situ* without any additional purification step for silica NPs. The thiol modified silica NPs were purified *via* centrifugation/redispersion cycles and finally dispersed in chloroform. These core silica NPs particles were then ready for self-assembly with tetraoctylammonium bromide (TOAB) capped ~ 5 nm AuNPs from a modified Brust-Schiffrin protocol. Finally, thiol terminated PEG (PEG-SH) was added to the "hollow" AuNPs colloid to form a protective shell. The detailed procedure can be found in **Section 8.6**. The formation of the targeted core–satellite structure is confirmed by TEM (**Figure 6-1**). Notably, the close-arranged AuNPs induce significant surface-plasmonic coupling between AuNPs: the "hollow" AuNPs structure exhibits a subtle red shift color change from red to violet.

Scheme 6-2 Schematic illustration of synthetic route for “hollow” AuNPs.

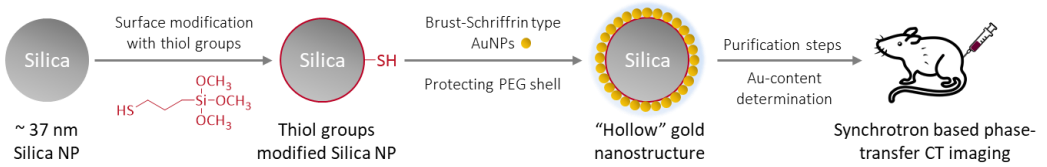

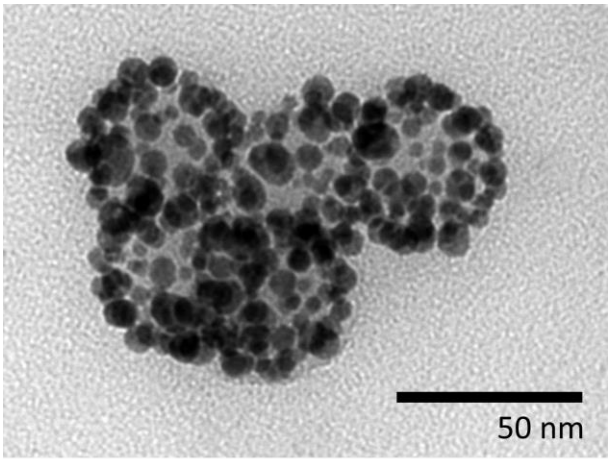

Figure 6-1 TE micrograph of the as-prepared “hollow” gold nanostructure.

As mentioned before, the Brust-Schiffrin method must be upscaled to meet the requirements for *in vivo* experiment. The major issue for this protocol in practice is the inconsistency of aggregation during the growth step. In the previous method, a typical reaction should be able to fabricate around 40 mg of AuNPs with the assumption of 100% conversion. However, the random formation of aggregations causes a potential dramatic loss of the yield AuNPs. To simultaneously address this issue and upscale the reaction, disposable glass flasks (100 mL) with a flat bottom design are chosen as the reactor with a small stir bar (length = 1 cm, diameter = 2 mm). The stirring velocity during the growth step was digitally set at 300 rpm to avoid the occurrence of any turbulent flow between the organic and aqueous layers. In this way, the random formation and growth of gold aggregates can be effectively suppressed for reliable production of ~ 5 nm Brust-Schiffrin type AuNPs.

The as-synthesized “hollow” AuNPs colloid was first concentrated from 200 mL (a mixture consisting of 5 batches) to approximately 1.5 mL (raw sample) using the centrifugation method before the quantitative analysis of gold content. Notably, during the centrifuge steps, the product

nanoassemblies were transferred from organic solvents into an aqueous condition, the excess AuNPs were also removed. The detailed experimental procedures for the upscaled synthesis of Brust-Schiffrin type AuNPs and fabrication/purification for the "hollow" AuNPs sample can be found in **Section 8.6**.

The synthesis of the "solid" AuNPs (reference sample) is very straightforward: the self-assembly process of PEG-SH onto the surface of ~ 13 nm citrate capped AuNPs was achieved by mixing citrate capped AuNPs with PEG-SH in an aqueous condition. The challenge here is the scale of production and method for concentrating since the Au content in the as-synthesized ~ 13 nm AuNPs is very low (0.1 mg/mL). Considering the loss of AuNPs during the multiple centrifugation steps, a 1.5 L colloid of citrate capped AuNPs was concentrated into approximately 0.8 mL (raw sample) before the quantitative analysis of gold content.

The Au content of the reference sample can be determined by comparing the plasmonic absorption in the UV-Vis spectrum with the original citrate capped AuNPs colloid (0.1 mg/mL). For the "hollow" AuNPs sample, due to the strong surface plasmonic coupling between the surface-bound AuNPs, this method is no longer suitable. An alternative method is applied for the determination for the "hollow" AuNPs sample: the AuNPs in the sample were converted into $HAuCl_4$ and the analysis was based on the specific absorption of $Au^{III}Cl_4^-$ ions with UV-Vis measurements (**Figure 8-19**, **Figure 8-20**). Detailed procedures for these analyses can be found in **Section 8.6**.

After knowing the Au content in both raw samples, the concentration of AuNPs can be adjusted to 100 mgAu/mL for the *in vivo* phase-contrast CT experiments. Notably, the high-density of PEG shell offers sufficient colloidal stability between sample delivery and imaging experiments.

The CT imaging experiments were carried out with the SYRMEP (Synchrotron radiation for medical physics) beamline from Elettra Synchrotron Trieste by PD Dr. Christian Dullin and co-workers. Three types of contrast agents – hollow AuNPs, reference AuNPs, and conventional $BaSO_4$ – were quickly injected into the mice, respectively, and phase-contrast

images of the mice lung were recorded. **Figure 6-2** shows that the "hollow" AuNPs (**B**) offer great imaging quality with high contrast and resolution. The "hollow" AuNPs outperform the conventional $BaSO_4$ (**C**) for better texture visualization of the soft tissues. However, the PEG capped ~ 13 nm AuNPs showed an unexpected toxic effect[268] on the mouse causing abnormal behavior of the animal. For this reason, the comparison with "solid" and "hollow" AuNPs was unable to be completed. However, it can be concluded that the core–satellite arranged "hollow" AuNPs offer a strong enhancement effect on the phase signal of CT experiment while carrying very low toxicity for *in vivo* application.

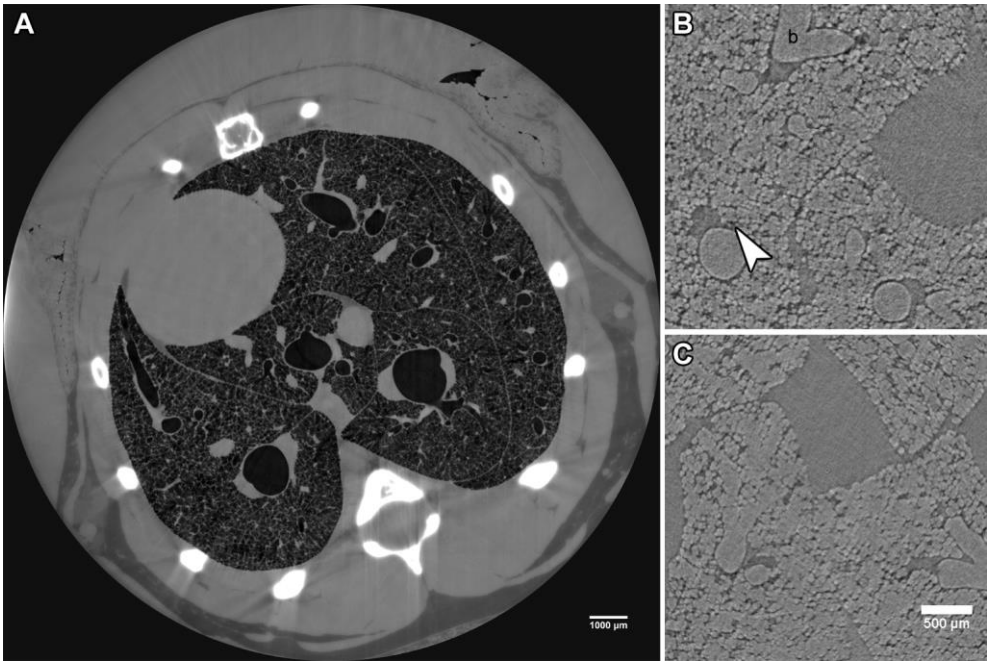

Figure 6-2 (**A**) Overview image of mice's lung visualized by phase-contrast CT. (**B**) Image with higher magnification using hollow AuNPs as the contrast agent. (**C**) Image with higher magnification using $BaSO_4$ as the contrast agent.

6.3 Conclusion

In this project, a highly efficient synthetic route for mimicking hollow gold nanoparticles is established, as a novel contrast agent for phase-contrast CT is established. Thiol functionalized silica NPs was used as a template for the self-assembly of AuNPs as gold shell, which is further protected by PEG

shell to increase the colloidal stability and biocompatibility. Furthermore, A reference sample (PEG capped ~ 13 nm AuNPs) is fabricated for comparison. Both samples were synthesized on a large scale and finally concentrated into a 1 ml colloid containing 100 mg gold. The CT-image of mouse lung with "hollow" AuNPs as contrast agent displays a strong image enhancement and provides very detailed structural information about soft tissue. The "hollow" AuNPs sample shows much lower toxicity compared with the reference AuNPs. The unexpected cytotoxicity of PEG capped ~ 13 nm AuNPs could be originated from the destabilization of nanoparticles in the biological media.

Overall, the design, fabrication, and quantitative analysis of "hollow" AuNPs are successful. The *in vivo* phase-contrast CT imaging experiment also demonstrates the strong enhancement and low toxicity of the nanostructure.

7
Closing Remarks

In this thesis, within four projects, a great number of well-defined nanostructures have been designed and fabricated for targeted application scenarios:

Superparamagnetic magnetite NPs carrying high-density PNIPAM brushes have been successfully prepared (**Chapter 3**). Reversed microemulsion method was chosen to achieve a precise one-to-one silica coating on hydrophobic oleylamine-capped MNPs, with a well-controlled silica thickness. Applying SI-RAFT polymerization, PNIPAM brushes with tunable molecular weight were grafted onto the silica-coated MNPs, imbuing the nanohybrids perfect dispersibility in various solvents. The polymer-grafted nanohybrids can self-assemble into ordered 2D nanopatterns with interparticle distance varied within 100 nm. Furthermore, owing to the well-defined structure, the fine control of silica shell thickness (~ 14 nm), and the polymer brushes, the magnetic interaction between MNP cores is significantly suppressed, as confirmed by SQUID experiments.

The project around the NIR photoluminescent Egyptian blue (**Chapter 4**) has made four breakthroughs on this material: I) effective mass production of EBNS, II) cracking down the size of EBNS, III) addressing the issue that EBNS lacks surface chemistry, and IV) new knowledge on the size-dependent PL performance of EBNS. A state-of-the-art method for mass production of EBNS (~ 60 g) has been established using high-energy stirred media milling. For the first time, the size of EBNS has been reduced to a diameter of 90 ± 50 nm and a thickness of 2.6 ± 0.6 nm. As a comparison, EBNS produced from the method in literature has a much larger dimension with the lateral size up to several μm. PL measurements reveal degeneration of PL

performance with reduced size of ENBS. This knowledge advance provides a guideline for choosing appropriate nanosheets' size in future studies. This work further exhibited the first surface modification chemistry of EBNS: A modified Stöber method was applied to achieve a thin silica shell on EBNS. Furthermore, two types of high-density polymer brushes, PNIPAM and PMMA, have been introduced onto the surface of silica-coated EBNS, rendering their diverse dispersibility and functions to EBNS. In particular, PMMA grafted EBNS shows significantly reduced light scattering due to the matched refractive indices, thus improving PL behavior.

In **Chapter 5**, silica NPs were used as a temporary template for the formation of circular AuNPs nanopattern on the surface of the carbon film substrate. Utilizing the apropos adsorption of PEG chains on silica, the silica-core–Au-satellite nanostructure was formed in colloid by self-assembly of PEG capped AuNPs onto the silica surface. The 3D nanoassemblies were cast onto a substrate to form a perfect 2D circular arrangement of AuNPs around silica NPs with a rationally hypothesized AuNPs re-arrangement during the process. A facile etching condition was found to remove the silica templates efficiently while maintaining the circular nanopattern undisturbed: The extremely high concentration of NaOH, along with the increased temperature are crucial to immobilize the AuNPs by significantly reducing the solubility of the PEG shell. In the future study, this templating and etching strategy can be extended with a great selection of varieties, e.g., by grafting PEG on other nanomaterials, diversifying size the and geometry of silica template, varying the PEG chain length and substate material.

Lastly, a core–satellite nanostructure from gold and silica NPs was designed as a contrast agent for phase-contrast CT imaging (**Chapter 6**). Thiol modified silica NPs were used as a template to attach AuNPs, to imitate a hollow gold design, which is further protected with a PEG shell for perfect water dispersibility and biocompatibility. As a comparison sample, PEG capped AuNPs were also fabricated. The synthetic routes for both samples were highly optimized to achieve the large sample requirement of 100 mgAu/mL in 1 mL. Furthermore, quantitative analysis methods to determine and regulate Au content in both samples were also established. CT

experiment shows an improved imaging contrast from the mouse injected with the hollow gold sample, compared with conventional contrast agent.

In summary, this thesis demonstrates the flexible strategies of fabricating diverse functional nanostructures. The in-depth understanding of the interaction and surface chemistry between each nanocomponent, silica surface, and functional polymers offers the optimized design and performance of the nanohybrids.

8
Experimental

8.1 Chemicals

Iron(III) acetylacetonate (Sigma-Aldrich, 97%), ethanol (Sigma-Aldrich, 99.8%), oleic acid (Sigma-Aldrich, 90%), oleylamine (ACROS, approximate C18-content 80–90%,), 1,2-dodecanediol (Sigma-Aldrich, 90%), benzylether (Sigma-Aldrich, 98%), 3-aminopropyldimethylethoxysilane (abcr, 97%), IGEPAL® CO-520 ($\bar{M}_n$ = 441 g · mol^{-1}, Sigma-Aldrich), *n*-hexane (VWR, 98.4%), chloroform (Fischer, HPLC), cyclohexane (VWR, ≥ 99%), aqueous ammonia (VWR, ~ 32%), tetraethyl orthosilicate (Sigma Aldrich, ≥ 99%), mercaptothiazoline (Sigma Aldrich, 98%), 1,4-dioxane (ROTH, ≥ 99.5%), hydrofluoric acid (Sigma-Aldrich, 48%), dicyclohexylcarbodiimide (Sigma-Aldrich, 99%), 4-(dimethylamino)pyridine (Sigma-Aldrich, 99%), 4-cyano-4-(dodecylsulfanylthiocarbonyl)sulfanylpentanoic acid (CDSPA, abcr, ≥ 97%), hydrochloric acid (Sigma-Aldrich, 37%, p.A.), nitric acid (Sigma-Aldrich, 65%, p.A.), diisopropylether (Acros, 99%), acetone (Sigma-Aldrich, ≥ 99.7%, GC), sodium hydroxide (Sigma-Aldrich, reagent grade), tetraoctylammonium bromide (TOAB, Sigma-Aldrich, 98%), magnesium sulfate (MERCK, anhydrous), toluene (Fischer, HPLC), hydrogen tetrachloroaurate trihydrate (ABCR, 99.9%), trisodium citrate dihydrate (Sigma-Aldrich, ≥ 99%), (3-mercaptopropyl)methyldimethoxysilane (Sigma-Aldrich, ≥ 95%), octadecylamine (Sigma-Aldrich, ≥ 99%), sodium borohydride (Acros, 99%), sulphuric acid (Sigma-Aldrich, p.A.), poly(ethylene glycol) methyl ether thiol ($\bar{M}_n$ = 6000 g/mol, Sigma-Aldrich), and commercial PMMA ($\bar{M}_w$ = 35 kg/mol, Acros) were used as received.

NIPAM was recrystallized twice from toluene/hexane (3 : 1) and stored at 3 °C prior to use. AIBN (Fluka, 98%,) was recrystallized twice from diisopropyl ether and stored at – 20 °C prior to use. Methyl methacrylate (Sigma-Aldrich, stabilized with hydroquinone monomethyl ether) was purified with inhibitor remover (Sigma-Aldric) before use. Tetrahydrofuran (Acros, 99.9%) was dried over CaH_2 overnight and distilled before use.

Egyptian blue bulk material was purchased from Kremer Pigments GmbH in powder form. Nanopure (type I) water was obtained from a Millipore water purification system equipped with a UV lamp (electric resistivity 18.2 MΩ · cm).

8.2 Equipment and analytical methods

Size-exclusion chromatography (SEC)

PNIPAM samples were analyzed with a dimethylacetamide SEC setup. SEC measurements were conducted at 45 °C on an Agilent 1260 Infinity SEC system equipped with a PSS GRAM precolumn (polyester copolymer network, 8 × 50 mm; 5 µm particle size) and three PSS GRAM separation columns (PSS SDV; 8 × 300 mm; 30, 10^3, and 10^3 Å pore sizes). Dimethylacetamide containing 0.1% LiBr was used as eluent with a flowrate at 0.8 mL · min^{-1}. An Agilent RI detector was used. The setups were calibrated with linear PMMA standards with low dispersity. All samples (5 mg · ml^{-1}) were filtered through a 0.45 µm PTFE filter prior to injection.

PMMA samples were analyzed with a THF SEC setup. SEC measurements were conducted at 35 °C on an Agilent 1260 Infinity SEC system equipped with a PSS GRAM precolumn (styrene-divinylbenzene copolymer network, 8 × 50 mm; 5 µm particle size) and three PSS GRAM separation columns (PSS SDV; 8 × 300 mm; 10^6, 10^5, and 10^3 Å pore sizes). THF (containing 0.1% toluene as internal standard) was used as eluent with a flowrate at 1.0 mL · min^{-1}. An Agilent RI detector was used. The setups were calibrated with linear PMMA standards with low dispersity. All samples (5 mg · ml^{-1}) were filtered through a 0.45 µm PTFE filter prior to injection.

Thermogravimetric analysis (TGA)

TGA was carried out using a TG 209 F3 Tarsus analyzer in the temperature range from 25 to 1000 °C at a heating rate of 10 °C/min under N_2 gas flow (20 mL/min).

Super quantum interference device (SQUID) measurements

SQUID measurements were kindly conducted by Dr. Serhiy Demeshko using a Quantum Design MPMS-XL-5 magnetometer. ZFC/FC curves were recorded with a static field of 100 Oe in the range from 295 to 2 K.

Transmission electron microscopy (TEM)

TEM measurements were carried out on a Philips CM 12 electron microscope operated at an acceleration voltage of 120 kV and an emission current of 3–4 µA. The focused electron spot has a diameter of 10 µm. A 50 µm aperture was used in the condenser lens and all scattered electrons were blocked with a 20 µm aperture. An Olympus 1376 × 1032 pixel CCD camera was used to acquire micrographs. Samples were prepared by drop-casting method and slow evaporation of the solvent. Two types of TEM sample holders are used in this thesis: Plano S166-3 with lacey carbon films (thickness ~ 3 nm) covering 300 mesh copper grid, and Plano S166 with 200 mesh copper grid holding an amorphous carbon film (thickness ~ 10 nm).

Dynamic light scattering (DLS)

DLS samples were measured on a Malvern Zetasizer Nano S system operating at 633 nm at a scattering angle of 173°. Samples were diluted with solvent according to the DLS detector signal.

DLS measurements for EB particle size during the fine grinding process were kindly conducted by Christoph Peppersack (Institut für Partikeltechnik, Technische Universität Braunschweig), using a NANOPHOX analyzer (Sympatec GmbH).

Atomic force microscopy (AFM)

AFM measurements were performed on a Multimode AFM (Bruker) with a NanoScope V controller using PeakForce QNM with a SCANASYST-AIR-HR cantilever (Bruker) at ambient condition. EBNS samples were prepared by drop-casting method from water/ethanol (1 : 2 in volume) dispersion on a silicon substrate.

Laser diffraction analysis

Particle size determinations during pre-grinding of EB were kindly conducted by Christoph Peppersack (Institut für Partikeltechnik, Technische Universität Braunschweig), monitored by laser diffraction analysis (Helos, Sympatec GmbH). The measurements were performed in the cuvette system by stirring at 1000 rpm. Samples were diluted with deionized water until an optical concentration of 15–20% was reached.

UV-Visible-Near Infrared (UV-Vis-NIR) spectroscopy

UV-Vis-NIR spectroscopy was performed with JASCO V-770 equipped with a PMT detector for the UV-Vis region and a peltier-cooled PbS detector for the NIR region. QS quartz cuvettes with a light path length of 10 mm were used for the measurements. The absorption spectra were recorded with a scan rate of 400 nm/min and a baseline correction by subtracting the spectrum of the pure solvent.

Photoluminescence (PL) spectroscopy

PL spectroscopy of EB samples was kindly conducted by Denis Pluta (Institut für Physikalische Chemie und Elektrochemie, Leibniz Universität Hannover), measured by an FLS1000 photoluminescence spectrometer (Edinburgh Instruments) equipped with a NIR-PMT InGaAs detector (liquid nitrogen cooled). The emission spectra were recorded with excitation wavelength at 637 nm, excitation bandwidth of 10–13 nm, and emission bandwidth of 1 nm.

Bath-type ultrasonicator

A bath-type ELMA S30H ultrasonic cleaner operating at 37 kHz with effective sonication power of 80 W and peak performance max of 320 W is used. The operation temperature of the water bath was kept below 50 °C. Samples were fixed in the center of the bath.

Sonic dismembrator

A Fischerbrand Model 120 sonic dismembrator was used to effectively disperse silica NPs or silica-coated nanomaterials in the centrifugation/redisperse cycles. The sonic dismembrator was operated with ultrasonic frequency at 20 kHz and maximum wattage at 120 W. The actual output was tuned to match the requirement of the samples.

Synchrotron-based phase-contrast computed tomography (CT) imaging

CT imaging was kindly conducted by PD Dr. Christian Dullin (Universitätsmedizin Göttingen) with the SYRMEP (Synchrotron Radiation for Medical Physics) beamline from Elettra Synchrotron Trieste in Trieste, Italy. 1 mL of 100 mgAu/mL reference sample and "hollow gold" sample, as well as conventional $BaSO_4$ suspension, were injected into mice, respectively. Phase-contrast CT images of mice's lungs were recorded.

8.3 Fabrication and characterization of PNIPAM grafted MNP@SiO_2

Synthesis of activated RAFT (activated CDSPA)

The synthesis and purification of the activated RAFT are described in the literature[269]. The structure was confirmed by NMR spectroscopy. ^{1}H NMR (300 MHz, $CDCl_3$): δ (ppm) 4.58 (t, 2H, J = 7.5 Hz), 3.70–3.46 (m, 2H), 3.33 (t, 4H, J = 7.5 Hz), 2.70–2.43 (m, 2H), 1.89 (s, 3H), 1.70 (quint, 2H, J = 7.5 Hz), 1.43–1.26 (m, 18H), 0.89 (t, 3H, J = 6.6 Hz).

Synthesis of ~ 8 nm hydrophobic magnetite nanoparticles

This synthesis of ~ 8 nm magnetite nanoparticles is modified from the Sun's work[166]. In a typical experiment, a mixture of $Fe(acac)_3$ (0.706 g, 2 mmol), oleic acid (1.88 g), oleylamine (2.00 g), 1,2-dodecanediol (2.24 g), and benzyl ether (20 mL) was degassed with argon for 15 minutes before heated to 200 °C. The mixture was kept at 200 °C under stirring for 2 hours and then under reflux by raising the temperature to the boiling point of benzyl ether (293 °C) and the mixture was heated under reflux for another 1 hour. The heating rate was not digitally controlled (approximately 15 minutes until boiling). The mixture was then spontaneously cooled to room temperature. A piece of neodymium magnet was used to collect MNPs from the mixture. The MNPs were washed with ethanol (30 mL) twice then dispersed in a*n*-hexane (3 mL) solution containing oleic acid (0.5 mL) and oleylamine (0.5 mL). Centrifugation (6000 rpm, 10 min) was used to remove any undispersed residue. The excess of oleic acid and oleylamine was removed by precipitation from *n*-hexane in ethanol (30 mL) and followed centrifugation (6000 rpm, 10 min). The MNPs were finally dried *in vacuo* and stored under an argon atmosphere.

TE micrograph of the as-synthesized MNPs and corresponding size distribution (7.9 ± 1.9 nm) histogram are shown in **Figure 8-1**. It is noted here that due to the limited control of heating rate from 200 °C to the boiling point of the solvent (293 °C), the size distribution of MNPs is sightly broader than the particles from Sun's work.

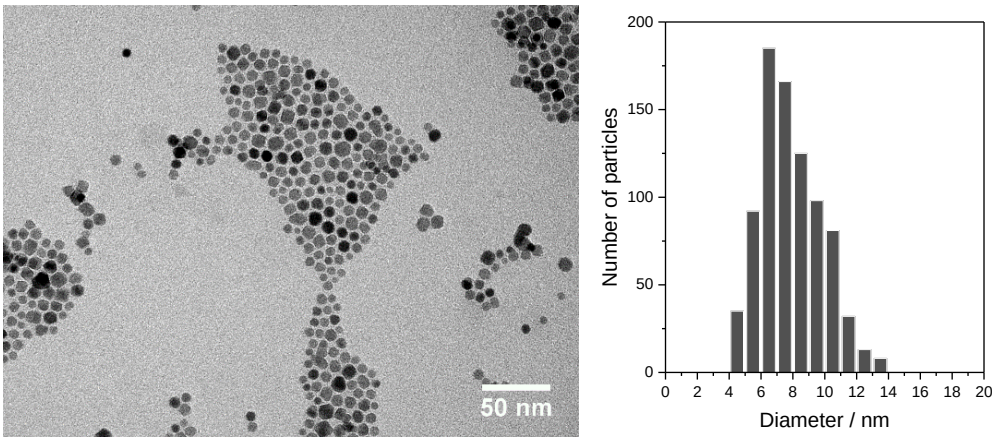

Figure 8-1 Exemplary TE micrographs and size distribution histogram of as-

prepared MNPs.

Synthesis of MNP@SiO_2 with reverse microemulsion method

The one-to-one silica coating was proceeded with a modified protocol from the literature[86]. MNPs (11.5 mg) were dispersed in cyclohexane (11.5 mL) with the aid of a bath sonication for short time and added dropwise under stirring into a cyclohexane solution of IGEPAL® CO-520 (31.3 g in 250 mL). After 10 min of stirring, ammonia (32% aq., 2.3 mL) was added to the solution dropwise. After another 30 min of stirring, TEOS (1.72 mL) was added to the mixture. The reaction was performed overnight at room temperature under vigorous stirring and then quenched by addition of a large excess of ethanol (~ 50 mL). MNP@SiO_2 was purified by three-fold centrifugation cycles in ethanol (5000 rpm, 30 min) and obtained after drying *in vacuo*.

TE micrographs and size distribution histogram of as-synthesized MNP@SiO_2 (35.7 ± 3.7 nm) are shown in **Figure 8-2**. This protocol provides uniform silica coating with a thickness of 13.9 ± 2.1 nm and only contains 4.6% particles with duo or multiple cores and 0.1% core-free particles (determined by counting over 1000 particles).

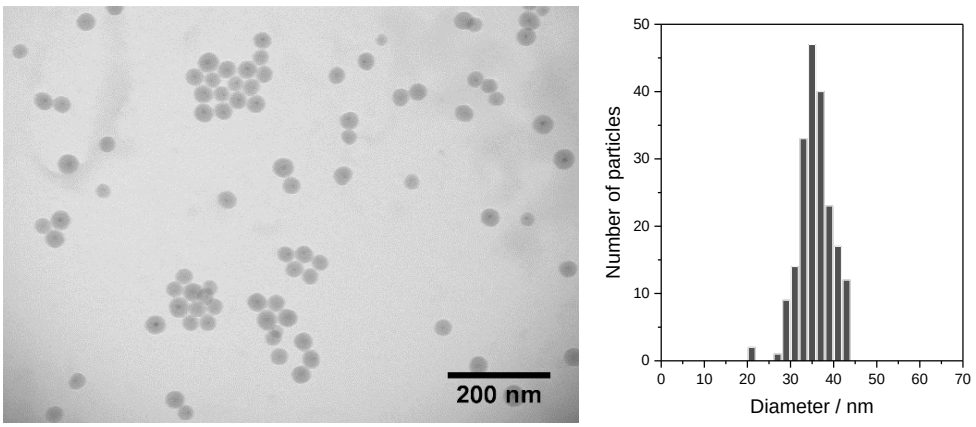

Figure 8-2 Exemplary TE micrographs and size distribution histogram of MNP@SiO_2 NPs.

Anchoring RAFT agents to MNP@SiO_2 surface

The anchoring of the RAFT agents to MNP@SiO_2 was proceeded with a

modified protocol from the literature[96]. In a typical experiment, MNP@SiO_2 (298 mg) was dispersed in dried THF (30 mL) by bath sonicating, 3-aminopropyldimethylethoxysilan (150 µL) was quickly added to the sol. The reaction mixture was kept overnight at 85 °C under stirring and argon atmosphere to ensure an efficient anchoring of the amine groups. After the reaction, the amine-functionalized MNP@SiO_2 was purified by three-fold centrifugation cycles (THF/*n*-hexane) and dried under reduced pressure.

Next step, the amine-functionalized MNP@SiO_2 (300 mg) was dispersed in 6 mL dried THF with the aid of sonication. A THF solution (3 ml) containing activated RAFT agents (60 mg) was added to the sol and the mixture was sealed and kept stirring overnight. Three centrifugation cycles (THF/diethyl ether) were applied here to obtain the RAFT anchored MNP@SiO_2. These particles could be dried *in vacuo* and stored in ambient condition over at least 1 year without affecting their performance during polymerization.

Surface-initiated RAFT polymerizations of PNIPAM brushes from the surface of MNP@SiO_2

RAFT capped MNP@SiO_2 nanoparticles were dispersed in a dioxane (found to be the best solvent for grafting PNIPAM) solution containing predetermined NIPAM (**Table 8-1**) by bath sonication for 20 min in polymerization tubes to ensure sufficient dispersion. The RAFT agents (CDSPA) and AIBN were then added to the sol, then the mixture was purged with argon for 15 minutes. The polymerization of NIPAM was carried out at 60 °C. After predetermined times, the polymerization reactions were stopped by cooling in an ice bath and exposing the mixtures to air. The PNIPAM capped MNP@SiO_2 nanohybrid and free polymer were gathered by three centrifugation cycles from acetone in diethyl ether. The PNIPAM capped MNP@SiO_2 nanohybrid was then isolated from the free polymer by three-fold centrifugation/dispersion cycles in acetone. The detailed polymerization conditions are listed in **Table 8-1**. The molecular weight distribution of the free polymers is determined by SEC and shown in **Figure 8-3**.

To confirm the consistency of chain lengths between free and grafted polymers, the grafted polymer was cleaved from nanoparticles by dissolving the MNP@SiO_2 with HF solution. For doing this, PNIPAM-I grafted MNP@SiO_2 (12 mg) was dispersed in acetone (3 mL) in a polypropylene tube. Then, 100 µL of 40 wt% hydrofluoric acid was added into this dispersion and the mixture was stirred for 2 h with a PTFE coated stir bar. After complete evaporation of all liquid, the remained polymer can be characterized with SEC with the regular process. **Figure 8-4** shows the comparison of molecular weight distributions between the free PNIPAM I and polymer cleaved from PNIPAM capped MNP@SiO_2 I.

The PNIPAM grafted MNP@SiO_2 can be perfectly dispersed in chloroform, as shown in the DLS result (**Figure 8-5**). The TE micrographs in low magnification of PNIPAM I-V grafted MNP@SiO_2 are shown from **Figure 8-6** to **Figure 8-10**.

Table 8-1 Polymerization conditions for the synthesis of the PNIPAM grafted MNPs@SiO_2 with different chain lengths (I-V), resulted from SEC analysis of the corresponding free polymers.

Polymer	**I**	**II**	**III**	**VI**	**V**
$\bar{M}_n$ / kg · mol^{-1}	29	40	58	73	94
Đ	1.20	1.15	1.17	1.15	1.17
m(MNP@SiO_2) / mg	33	10	10	10	10
m(RAFT) / mg	3.12	4.50	3.10	2.10	2.10
Equiv. of RAFT	1.00	1.00	1.00	1.00	1.00
m(NIPAM) / mg	1000	750	700	1000	1000
Equiv. of NIPAM	1000	600	1000	1700	1700
m(AIBN) / mg	0.70	0.90	0.70	0.70	0.70
Equiv. of AIBN	0.40	0.50	0.40	0.80	0.80
V(dioxane) / mL	4100	3750	3500	3500	3500
Reaction's time / min	90	120	120	120	150

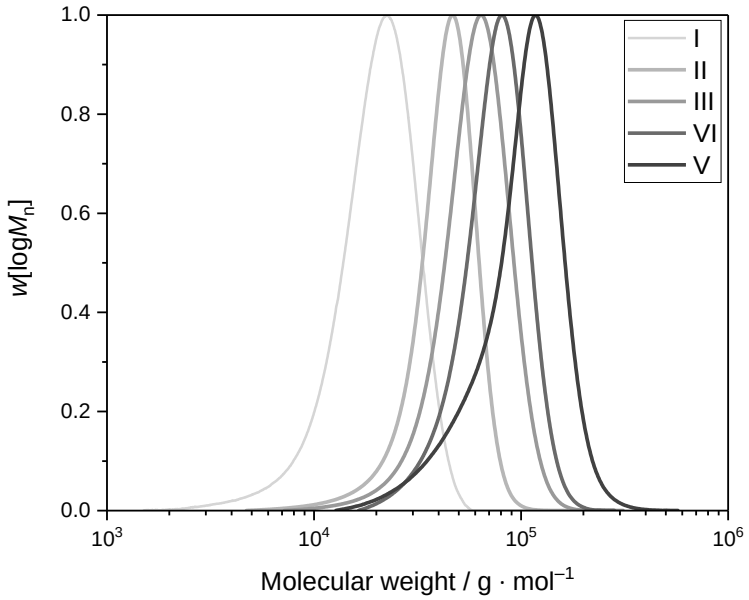

Figure 8-3 Molecular weight distributions from SEC analysis of the free polymers I-V.

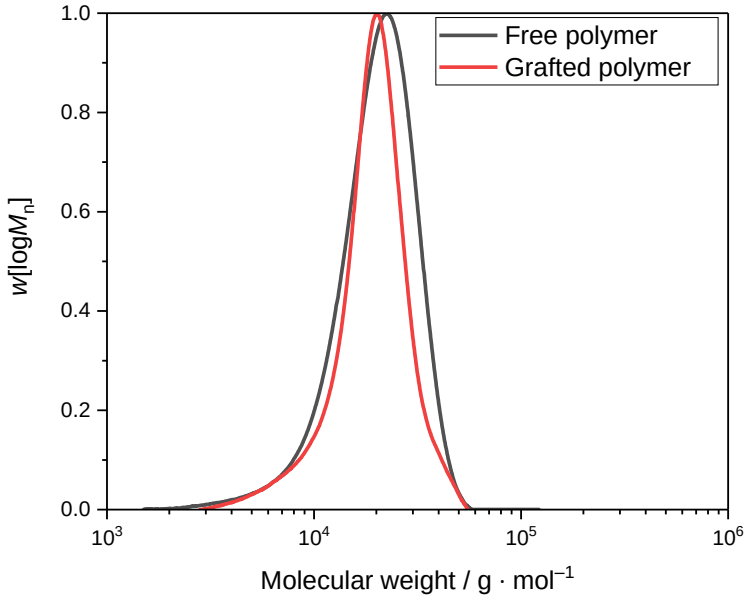

Figure 8-4 Molecular weight distributions from SEC analysis of the free PNIPAM-I and polymer cleaved from PNIPAM capped MNP@SiO_2-I.

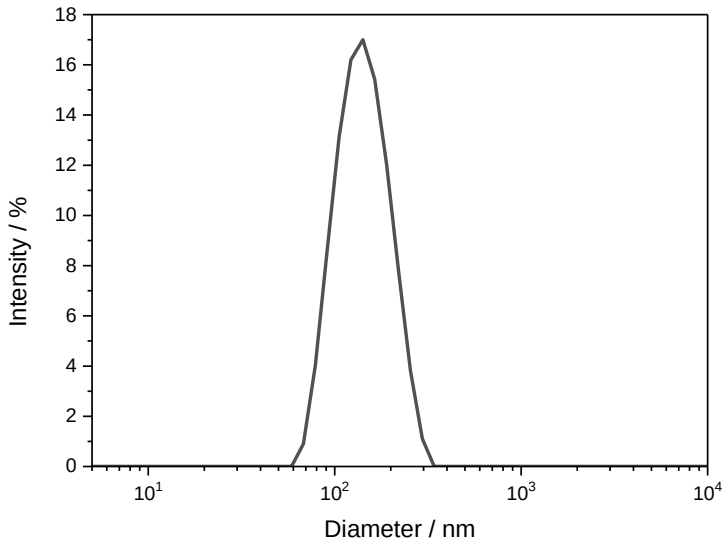

Figure 8-5 Hydrodynamic diameter from DLS measurement of PNIPAM-I capped MNP@SiO_2 in chloroform.

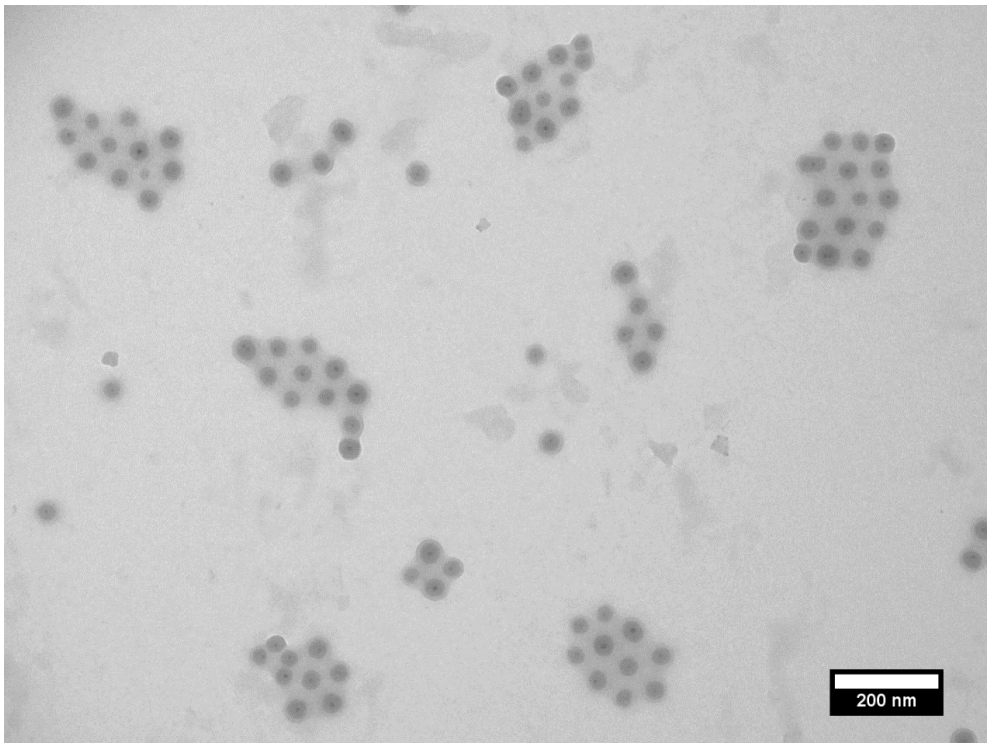

Figure 8-6 TE micrograph of PNIPAM-I capped MNP@SiO_2 in lower magnification.

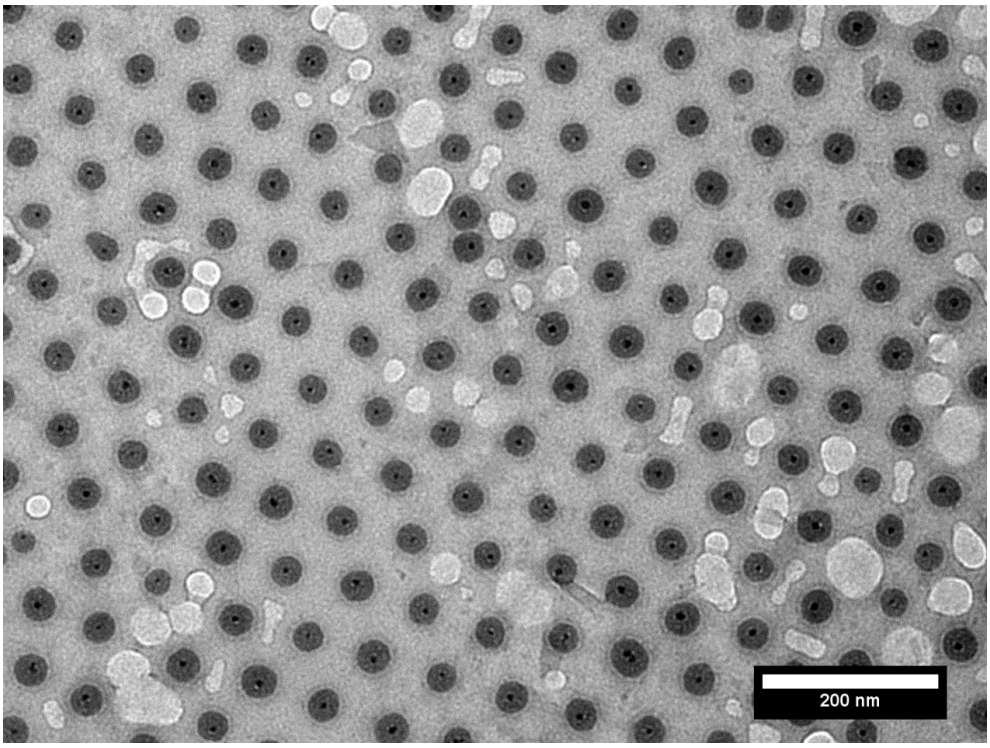

Figure 8-7 TE micrograph of PNIPAM-II capped MNP@SiO_2 in lower magnification.

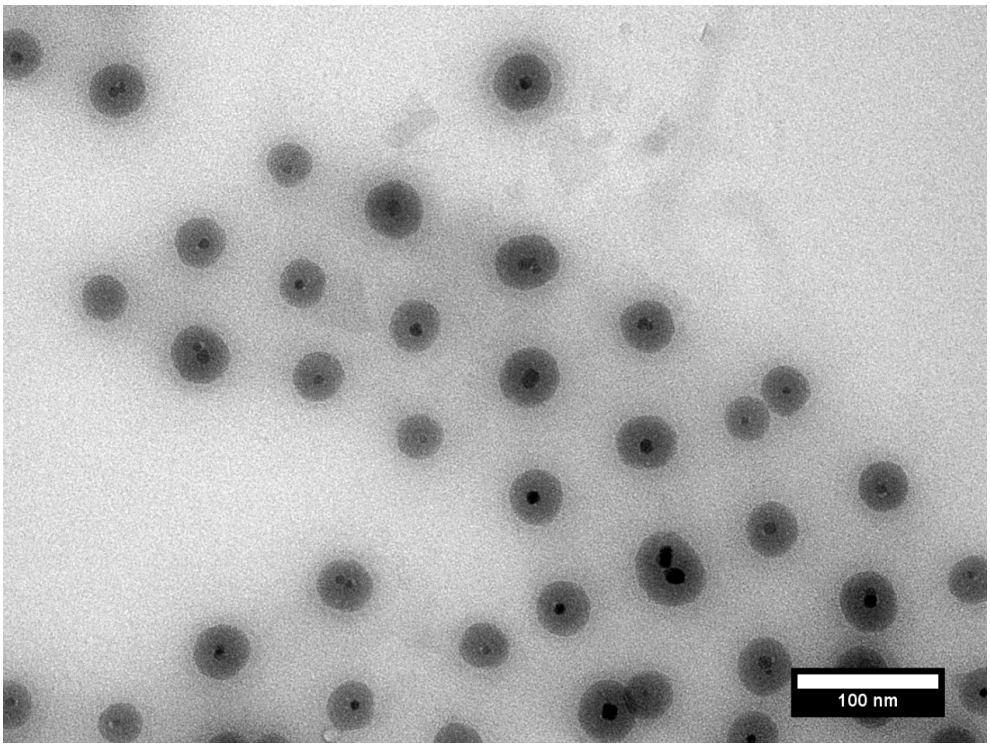

Figure 8-8 TE micrograph of PNIPAM-III capped MNP@SiO_2 in lower magnification.

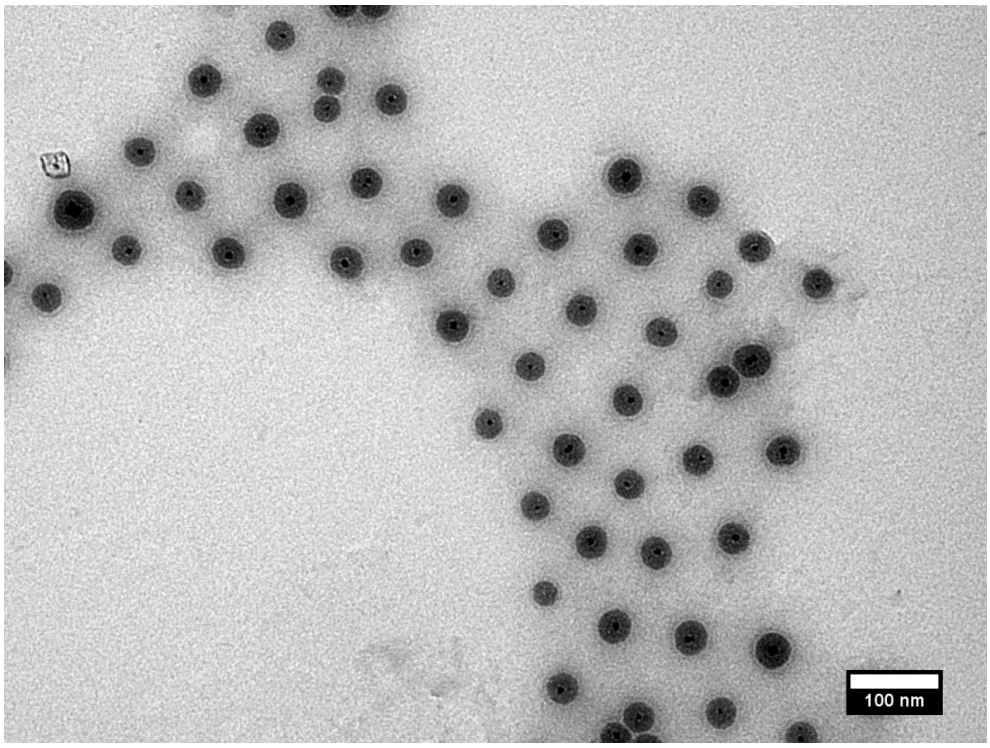

Figure 8-9 TE micrograph of PNIPAM-IV capped MNP@SiO_2 in lower magnification.

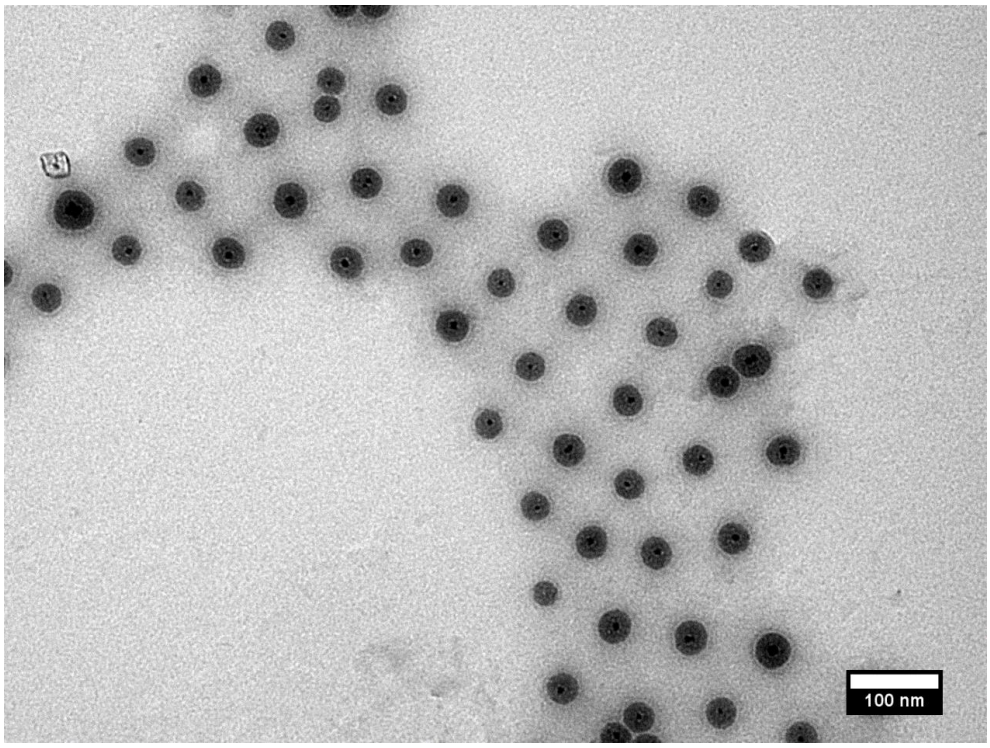

Figure 8-10 TE micrograph of PNIPAM-V capped MNP@SiO_2 in lower magnification.

Calculation of the grafting density from TGA results

Grafting density φ = 0.50 polymer chains / nm^2 was calculated using the known density, geometry of MNP@SiO_2 from TEM analysis, and molar mass from SEC analysis as such:

$$\varphi = \frac{\text{number of polymers pro mass}}{\text{total surface area of silica pro mass}} = \frac{\left(\frac{1-x_2}{x_2} - \frac{1-x_1}{x_1}\right) \cdot m(\text{MNP@SiO}_2)}{m(\text{PNIPAM}) \cdot A(\text{SiO}_2)} \qquad \textbf{8-1}$$

Here, x_1 and x_2 are the weight retention determined by TGA at 1000 °C for RAFT modified MNP@SiO_2 and PNIPAM grafted MNP@SiO_2, respectively (**Figure 8-11**). m(MNP@SiO_2) is the mass of one MNP@SiO_2, m(PNIPAM) is the mass of grafted PNIPAM molecule and A(SiO_2) is the surface area of one MNP@SiO_2.

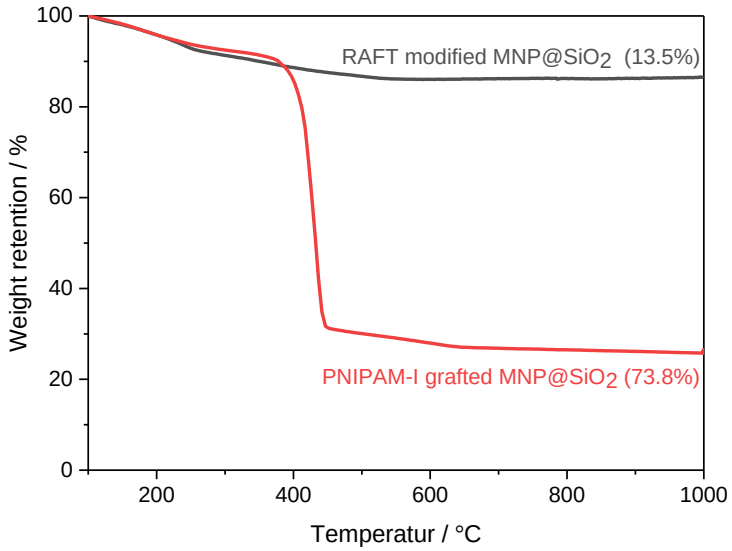

Figure 8-11 TGA curves of RAFT anchored MNP@SiO_2 and PNIPAM-I grafted MNP@SiO_2.

8.4 Fabrication methods and surface functionalization for Egyptian blue nanosheets

8.4.1 Fabrication methods for EBNS

Producing EBNS-GS with glass stir bar and hot water

The experimental condition for the fabrication of EBNS-GS is modified from the work of Johnson-McDaniel *et. al.*[131]

In a typical experiment, 250 mg of EB bulk material was incubated in an HCl solution (1 M, 20 mL) overnight. EB was then filtered, rinsed with deionized water, and dried overnight at 150 °C. This step is added to remove the Cu^{2+} containing impurity from the pigment (e.g. CuO). The purified EB was added to 20 mL nanopure water in a glass vial (57 mm × 27.5 mm Ø). This mixture was allowed to be stirred with a glass-coated stir bar (25 mm × 6 mm Ø) at 80 °C for 2 weeks. After the procedure, the mixture was cooled down and settled for 24 hours to collect the supernatant. A milky blue dispersion was yielded with swirling pearlescent distortions when agitated. EBNS-GS was finally collected by filtration (cellulose nitrate membrane, pore size 0.45 μm) and dried *in vacuo* (exfoliation yield ~ 50%).

Notably, the common PTFE stir bar cannot be used here for its insufficient hardness, otherwise, PTFE will be grinded by EB and no exfoliation can be observed.

Scalable production of EBNS-SMM using stirred media milling

Egyptian blue bulk material was soaked in 20 mL HCl (1 M) solution overnight then filtered, washed with deionized water, and dried overnight at 150 °C.

The milling experiment was kindly conducted by Christoph Peppersack (Institut für Partikeltechnik, Technische Universität Braunschweig) with a laboratory stirred media mill PML 2 (Bühler AG) using the process unit Centex™S2. Wear-resistant materials were chosen for both the rotor and the

lining of the chamber which consisted of polyurethane (DraisElast™) and sintered silicon carbide (SSiC), respectively. 60 g of Egyptian blue feed material were processed in deionized water (solid concentration of 6 wt%) by utilizing spherical grinding media made of yttria-stabilized zirconia (Sigmund Lindner GmbH). In the pre-grinding step (grinding time: 90 min), a media size of 849 µm and a circumferential speed of 8 m/s were chosen. In addition, the fine grinding (360 min) was conducted with a media size of 315 µm and a speed of 10 m/s. The operation temperature was set to 20 ± 2 °C by water cooling throughout both grinding steps. Samples were taken for particle size determination at pre-defined times for laser diffraction analysis (pre-grinding stage) or DLS (fine grinding stage). After grinding, a light-blue colloidal suspension (50 mg/mL) was obtained with very high colloidal stability (no permanent aggregated material after months).

8.4.2 Silica coating and functionalization on EBNS

Silica coating on EBNS

60 mg of EBNS-GS (dried) or 1.2 mL (corresponding 60 mg EBNS) as-obtained EBNS-SMM colloid was added into 300 mL ethanol and treated with bath-type ultrasonicator (5h for EBNS-GS to ensure a sufficient dispersion, 30 min for ENNS-SMM). Then 15 mL of aqueous ammonia and 3 mL of TEOS ethanol solution (10 vol%) were successively added into the dispersion and stirred overnight. The silica-coated EBNS were isolated from reactants by three-fold centrifugation/redispersion in ethanol and dried *in vacuo*.

Functionalization of silica-coated EBNS

The amine functionalization and followed anchoring with RAFT moieties on EBNS-silica surface were proceeded analogously to the approaches used in **Section 8.3**. Briefly, 3-aminopropyldimethylethoxysilan (300µL) was added into a dispersion of 130 mg silica-coated EBNS in 20 mL anhydrous THF. The reaction mixture was kept overnight at 85 °C under stirring. After the reaction, the amine-functionalized EBNS-silica was purified by three-fold centrifugation / redisperse cycles (3000 rpm, 15 min,

THF) and redispersed in 6 mL THF. Then, a THF solution (3 mL) containing activated CDSPA (120 mg) was added to the sol and the mixture was kept stirring overnight. The RAFT anchored EBNS-silica was purified by three-fold centrifugation / redisperse cycles (3000 rpm, 25 min, THF) and dried *in vacuo*.

Surface-initiated RAFT polymerization of PNIPAM and PMMA brushes from the surface of silica-coated EBNS

RAFT anchored EBNS-silica was dispersed in a monomer solution containing RAFT agents (CDSPA). AIBN was then added to the sol and the mixture was purged with argon for 15 minutes. The polymerization was carried out at 60 °C and stopped after predetermined times by cooling in an ice bath and exposing the mixtures to air.

In the case that the polymerization mixture was too viscous, it can be diluted with a proper solvent (acetone for PNIPAM, toluene for PMMA) before purification steps. The polymer capped EBNS along with its free polymer was gathered by three centrifugation cycles from acetone in the precipitation solvent (diethyl ether for PNIPAM and methanol for PMMA). The polymer capped EBNS was then isolated from the free polymer by three-fold centrifugation/dispersion cycles in acetone. The detailed polymerization conditions are listed in **Table 8-2**. The molecular weight distribution of the free polymers is determined by SEC and shown in **Figure 8-12**.

Table 8-2 Conditions for SI-RAFT polymerization from the surface of silica-coated EBNS-GS and EBNS-SMM. Molecular weight is determined from SEC analyses with the corresponding free polymers.

	PMMA on EBNS-GS	**PMMA on EBNS-SMM**	**PNIPAM on EBNS-SMM**
$\bar{M}_n$ / kg · mol^{-1}	88	139	104
$Đ$	1.2	1.2	1.5
m(EBNS) / mg	60.5	9.5	6.7
m(RAFT) / mg	11.2	11.0	2.1
Equiv. of RAFT	1.00	1.00	1.00

m(monomer) / g	12.00	6.00	1.00
Equiv. of monomer	4320	2200	1700
m(AIBN) / mg	4.8	2.4	0.7
Equiv. of AIBN	1.05	0.54	0.82
V(dioxane) / mL	-	-	3.5
Reaction's time / h	6	20	2.3

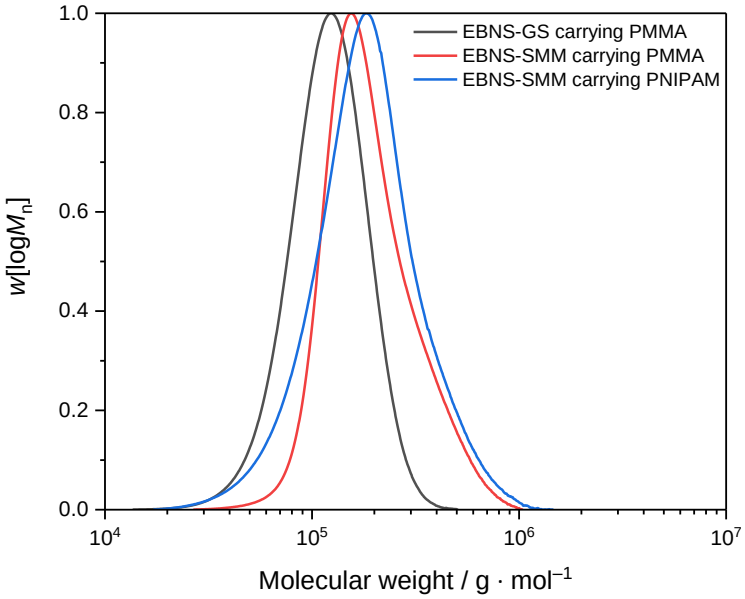

Figure 8-12 Molecular weight distributions from SEC analyses of the free polymers.

Notably, PMMA-grafted EBNS can be perfectly dispersed in the PMMA matrix. For this, a high-concentrated colloid of EBNS-GS-PMMA in toluene was mixed with a toluene solution of commercial PMMA ($\bar{M}_w$ = 35 kg/mol), then dried in a PTFE form (1.5 cm × 1.5 cm) by heated over aluminum beads bath (80 °C). The photograph of as-prepared composite material is shown below. The sample shows very homogenous transparency, indicating a perfect dispersion of EBNS in the PMMA matrix.

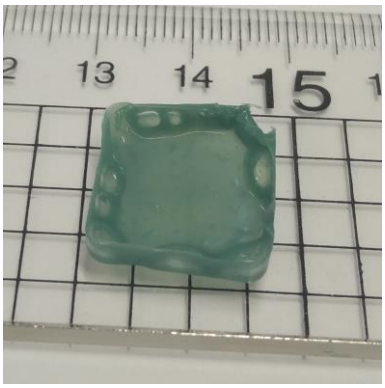

Figure 8-13 Composite material of 50 wt% PMMA grafted EBNS-GS in PMMA matrix.

Immobilization of AuNPs onto amine-functionalized EBNS-silica

100 µL colloid of amine-modified EBNS-silica (approximately 1.5 mg/mL) was mixed with 500 µL ~ 13 nm citrate capped AuNPs aqueous sol (approximately 0.1 mg/mL) under ultrasonication (10 s). The as-prepared nanohybrid AuNPs-EBNS nanohybrid was used freshly for TEM analysis.

8.5 Preparation of circular AuNPs nanopattern

Synthesis of ~ 13 nm citrate capped AuNPs

The synthesis of AuNPs was proceeded with a protocol from the work of Peng *et.al*.[73] Before the experiment, all glassware was cleaned by aqua regia, washed many times with nanopure water, and then oven-dried.

In a typical synthesis, a hot aqueous solution of sodium citrate (5 mL, 39 mM, 3.9 equiv.) was added into a boiling aqueous solution of $HAuCl_4$ (100 mL, 0.5 mM, 1.0 equiv.) under vigorous stirring. The mixture was stirred under reflux for further 15 minutes and then cooled to room temperature. The obtained AuNPs colloidal suspension (12.7 ± 0.8 nm, 0.1 mgAu/mL) was stored in polypropylene tubes in the dark at room temperature. Notably, this reaction can be 5 times upscaled and conducted in a 1 L flask.

To prepare the TEM sample, the AuNPs were phase-transferred into organic phase by adding the same volume chloroform containing 0.75 M

octadecyl amine into the as-obtained AuNPs sol and successive shaking (~ 2 min). TE micrograph of AuNPs and corresponding size distribution histogram are shown below.

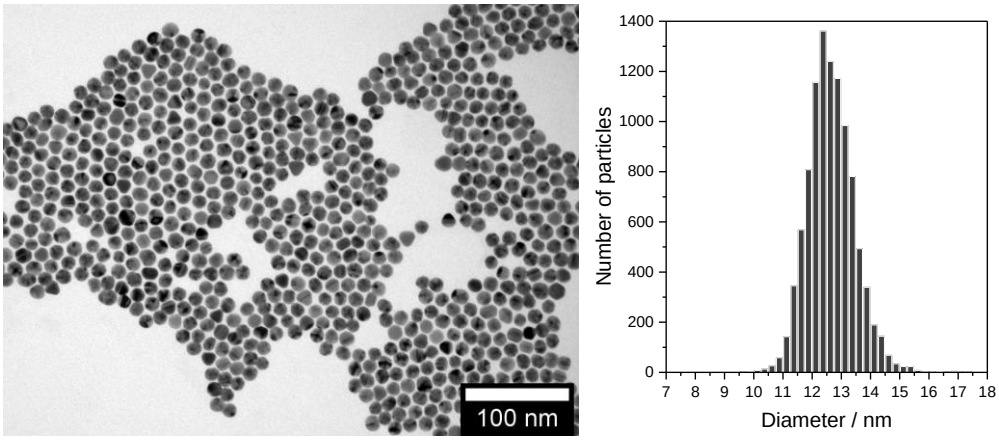

Figure 8-14 Exemplary TE micrograph and size distribution histogram of citrate capped AuNPs.

Preparing PEG capped AuNPs

1 mL of 1 mg/mL thiol terminated methoxy PEG ($\bar{M}_n$ = 6000 g/mol) was added into 10 mL of as-synthesized citrate capped AuNPs. This mixture was vigorously shaken for 1 min and sonicated for 3 min by a bath-type ultrasonicator to ensure sufficient polymer grafting on AuNPs. The PEG-AuNPs were purified by centrifugation and redispersed in THF. The Au content of PEG-AuNPs was calculated by comparing its absorption intensity from UV-Vis spectroscopy with that of citrate capped AuNPs.

Synthesis of ~ 46 nm Silica NPs

The synthesis of silica NPs is analogous to the procedure for MNP@SiO_2 described in **Section 8.3**. TEOS (35.2 µL) and ammonia (46.8 µL, 32% aq) were successively added into a solution of IGEPAL® CO-520 (638 mg) in cyclohexane (5.39 mL) under vigorous stirring. The reaction was proceeded overnight at room temperature under vigorous stirring and then quenched by the addition of ethanol (~ 4 mL). The silica NPs was purified by three-fold centrifugation cycles in ethanol (5000 rpm, 30 min) and stocked in 0.5 mL ethanol (approximately 8 mg/mL) for further usage. TE micrograph and size distribution histogram of as-synthesized silica NPs (46 ± 4 nm) are shown

below.

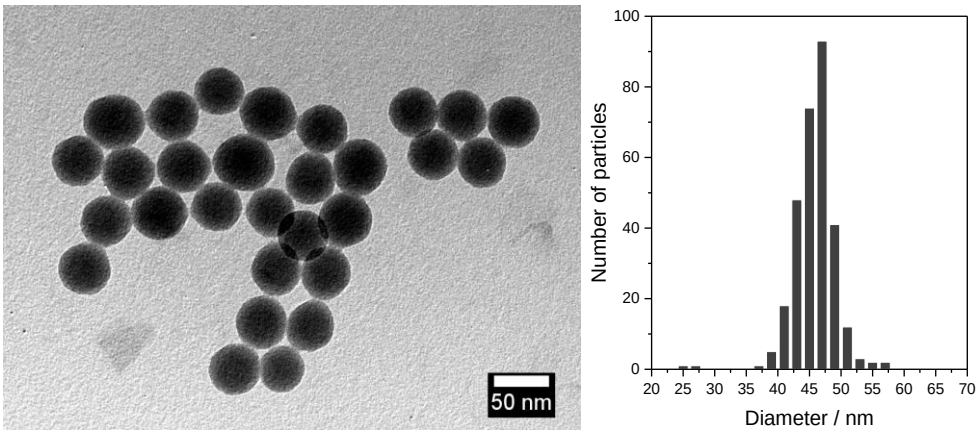

Figure 8-15 Exemplary TE micrograph and size distribution histogram of silica NPs.

Self-assembly of silica-core–AuNPs-satellite nanostructure

In a typical run, 5 µL of as-prepared silica NPs were added into PEG-AuNPs sol (0.23 mgAu/mL in 200 µL THF). This mixture was diluted 20 times and allowed to incubate for > 4 days to ensure completely colloidal self-assembly of silica-core–AuNPs-satellite nanostructure. 2D arrangement of the self-assembled nanohybrid was conducted by drop-casting 10 µL of colloid onto a lacey carbon film covered TEM-grid. The TEM-grid was left under ambient condition overnight (covered with a glass vial) to ensure complete evaporation of the solvent.

Selective etching of silica NPs template without disordering circular AuNPs pattern

TEM-grid with 2D silica-AuNPs pattern was incubated in 10 wt% aqueous NaOH for 30 min. After the incubation, the TEM-grid was quickly dipped in water and ethanol successively to remove excess NaOH and then left for solvent evaporation before the TEM analysis.

DLS measurements were performed to study the colloidal stability of 0.01 mg/mL PEG-AuNPs in different environments. The hydrodynamic diameter from DLS for PEG-AuNPs in water, 1 wt% NaOH, and 10 wt% NaOH at different temperatures are shown below. It is worth mentioning that AuNPs in 10 wt% NaOH at 85 °C underwent complete precipitation. In this

case, the actual value should be much larger than the distribution determined by DLS, since the sedimented particles cannot be measured in the colloid.

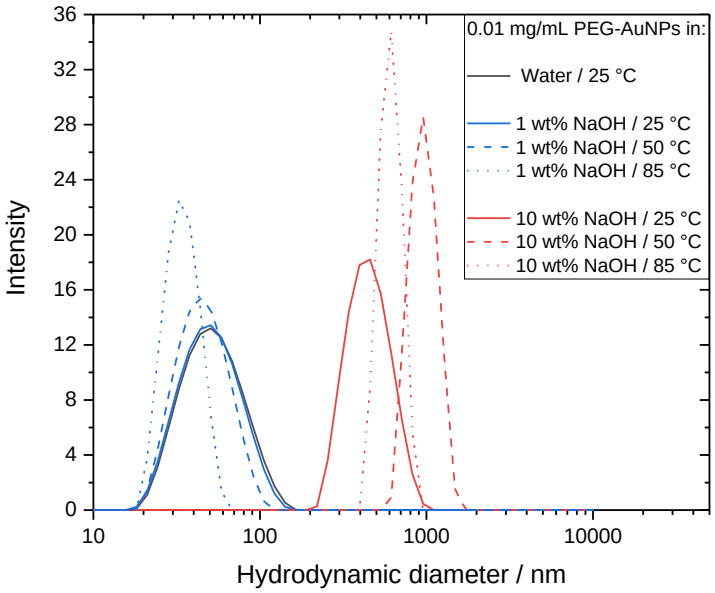

Figure 8-16 Size distributions from DLS of 0.01 mg/mL PEG-AuNPs in water, 1 wt% NaOH, and 10 wt% NaOH at three different temperatures (25 °C, 50 °C, and 85 °C).

8.6 Preparation of "hollow" gold nanostructure and its reference sample for CT imaging

Preparation of reference sample with 100 mgAu/mL

Reference sample (PEG capped AuNPs) was prepared by mixing citrate capped ~ 13 nm AuNPs (0.1 mgAu/mL, 1.5 L) and thiol terminated methoxy PEG ($\bar{M}_n$ = 6000 g/mol, 10 mg/mL in 15 mL water). The PEG capped AuNPs underwent four centrifuge cycles to be concentrated into 0.8 mL sol. The synthesis method for citrate capped AuNPs can be found in **Section 8.5**. The Au content in the reference sample was determined and regulated into 100 mgAu/mL to meet the requirement of CT imaging. For this, the plasmonic absorption of 1500 times diluted reference sample was measured by UV-Vis spectrometer and compared with original citrate capped AuNPs. According to the absorbances at 520 nm (**Figure 8-17**), the as-prepared

reference sample contains 197 mgAu/mL. A further dilution of this sample was conducted to give the final concentration of 100 mgAu/mL.

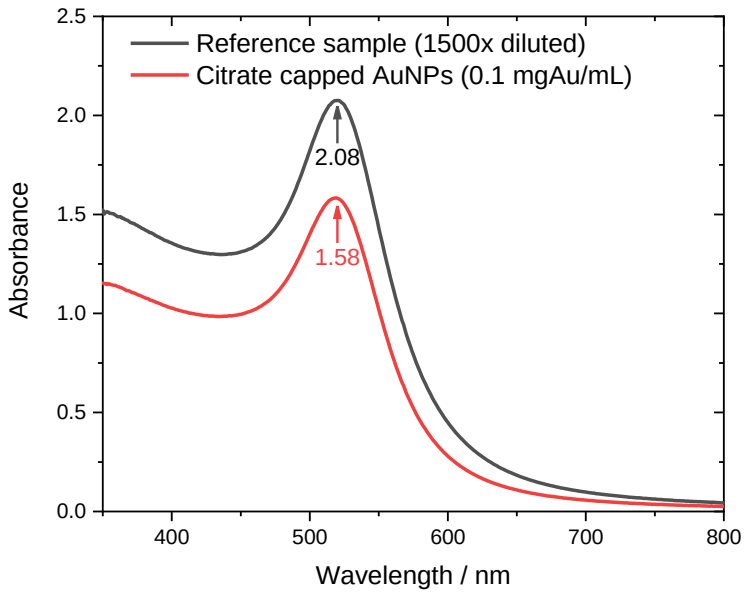

Figure 8-17 UV-Vis spectra of 1500 times diluted reference sample and the original citrate capped AuNPs sol.

Synthesis of thiol groups modified silica NPs

Thiol groups functionalized silica NPs (silica-SH) were prepared as the template of the "hollow" gold nanostructure. The procedure for the synthesis of silica NPs can be found in **Section 8.5**. TEOS (1 mL), ammonia (2.3 mL, 32% aq), IGEPAL® CO-520 (31.3 mg), and cyclohexane (250 mL) were used in a typical batch. After 14 hours of stirring, 100 µL of (3-mercaptopropyl)-methyldimethoxysilane was added directly into the reaction mixture. The mixture was allowed to stir for another 1 hour before being subjected to centrifugation purification with ethanol (3 times, 4000 rpm, 40 min). The yielded silica-SH (37 ± 2 nm in diameter) was dispersed in chloroform (1 mg/mL) for the next step.

Upscaled synthesis of Brust-Schriffrin type AuNPs

Hydrophobic AuNPs with a size of ~ 5 nm were fabricated with a modified Brust-Schiffrin two-phase method[270]. Some further optimization was made to increase the yield of the synthesis.

In two polypropylene centrifuge tubes, hydrogen tetrachloroauratetrihydrate (94.5 mg, 0.240 mmol) in nanopure water (20 mL) and TOAB (524.9 mg, 0.960 mmol) in toluene (20 mL) were mixed (20 ml mixture in each tube) and shaken vigorously for 120 s. During this step, the $AuCl^-$ in the aqueous phase was transferred into the toluene phase by forming ($N(C_8H_{17})_4^+AuCl_4^-$) ion pairs. After the phase-transfer step, the color of the water phase turned from yellow into colorless, whereas the initial colorless toluene phase became deep orange. The upper organic layer was then carefully transferred into a disposable flat-bottom glass flask (100 mL with crimp neck). A digital stirrer was used to precisely control the stirring velocity during the synthesis. Under vigorously stirring (1200 rpm) with a tiny stir bar (length = 1 cm, diameter = 2 mm), a freshly prepared solution of sodium borohydride (72.6 mg, 1.92 mmol) in water (5 mL) was added into the flask. The stirring velocity was kept for 120 s and then slowed down to 300 rpm to avoid any turbulent mixing between organic and aqueous phases. It is worth mentioning that, some aggregation of gold could sometimes appear in the bottom of the flask at the early stage of the reaction. The contact between aggregated material with the organic phase often leads to further growth of the aggregation and complete precipitation of gold. The stirring velocity and stir bar are thus appropriately selected to prevent this issue. After 4 hours of stirring, the organic phase was transferred into a clean separator funnel (rinsed with aqua regia and nanopure water prior to use), washed with dilute sulphuric acid (5%, 10 mL) and water (5 × 10 mL), and dried over magnesium sulfate. The yielded TOAB stabilized AuNPs (4.6 ± 1.5 nm) exhibits deep red-brown color and contains approximately 20 mgAu/mL.

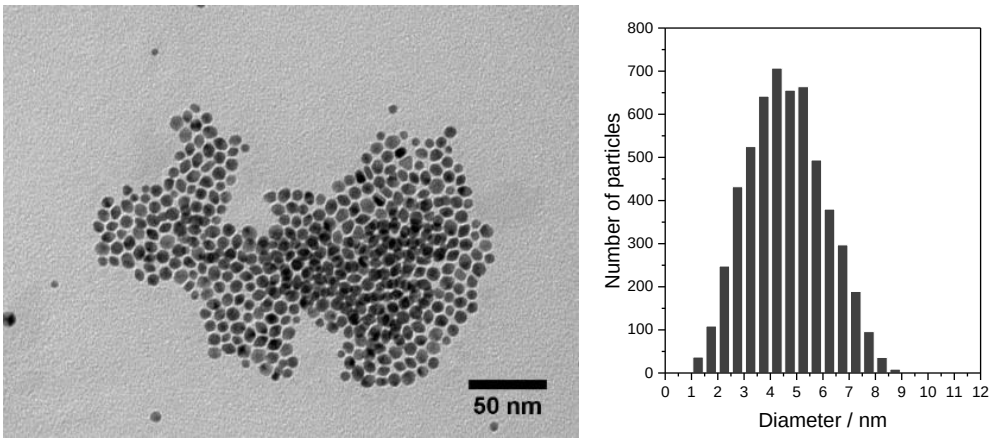

Figure 8-18 Exemplary TE micrograph and size distribution histogram of Brust-Schriffrin type AuNPs.

Preparation of AuNPs covered silica NPs for mimicking "hollow" gold nanostructures

In a typical batch, 3 mL colloidal dispersion of silica-SH (1 mg/mL in chloroform) was diluted with 32 mL chloroform, in which 7 mL of as-synthesized Brust-Schriffrin type AuNPs was then added. The mixture was mixed *via* shaking and treated with bath-type ultrasonication for 5 min. A solution of thiol terminated methoxy PEG (2.1 mL, 10 mL/mL) was added into the mixture under ultrasonication to protect the gold surface and improve the colloidal stability of the nanocomposites. The mixture was allowed to be sonicated for another 5 min before being subjected to centrifuge cycles. Notably, the content of AuNPs from each batch of Brust-Schriffrin synthesis significantly fluctuated. The ratio of used silica-SH and AuNPs sol must be adjusted to ensure a sufficient attachment of AuNPs on silica NPs. For this purpose, TEM measurements of some trial samples were conducted during the experiment to find a suitable ratio for the current batch. The content of solvents, as well as the silica-SH/PEG ratio, were always maintained as the same values. Five individual batches of the "hollow" gold nanohybrids were merged and centrifuged. During the centrifugation cycles, the solvent was exchanged from chloroform/toluene to ethanol, then finally to water. The nanocomposites were washed with water for another centrifugation step and concentrated into ~ 1.5 mL water. This sample is referred as "raw-hollow-Au" for brevity.

Quantitative analysis of gold content in the "hollow gold" sample

In the quantitative analysis, Au^0 in the hollow-Au sample was converted into $Au^{III}Cl_4^-$ in solution, so that the Au content can be determined by measuring the characteristic absorption of $AuCl_4^-$ at 313 nm, which can be assigned to ligand-to-metal charge transfer.[271]

In a typical experiment, 100 µL of 100 times diluted as-prepared raw-hollow-Au sample was dried at 80 °C in a ceramic crucible. The crucible was heated at 850 °C for 30 min to remove all organic contents. Notably, this temperature is also sufficient to melt AuNPs.[272] After cooling down to room temperature. The resultant Au^0 was dissolved in aqua regia to be converted into $HAu^{III}Cl_4$ and then diluted with water. The solvent and excess acid were removed by evaporation at 80 °C. The remaining chloroauric acid was dissolved in 2 mL of 0.1 M aqueous HCl under the consideration that the characteristic absorption of $AuCl_4^-$ is highly pH-dependent.[273] This sample was used for UV-Vis analysis with the final dilution factor of 2000, according to the Au content.

UV-Vis spectrum shows the $AuCl_4^-$ from raw-hollow-Au sample possessing an absorbance maximum of 0.901 at the wavelength of 313 nm (**Figure 8-19**). Based on this absorption band, a calibration series with commercially available $HAuCl_4 \cdot 3\,H_2O$ was performed, according to the relationship between Au content (mgAu/mL) and the absorbance at 313 nm (**Figure 8-20**). From these analysis results, the Au content in the raw-hollow-Au sample is determined as 64 mgAu/mL. This sample underwent another concentration *via* centrifugation to give a final "hollow" AuNPs sample with desired 100 mgAu/mL.

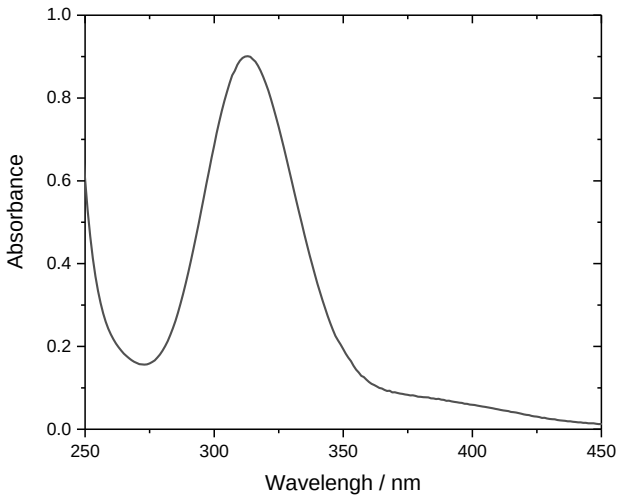

Figure 8-19 UV-Vis spectrum of $AuCl_4^-$ converted from the raw-hollow-Au sample. The measurement is conducted by using 0.1 M aqueous HCl as solvent. The dilution factor is 2000, according to the Au content from the raw-hollow-Au sample.

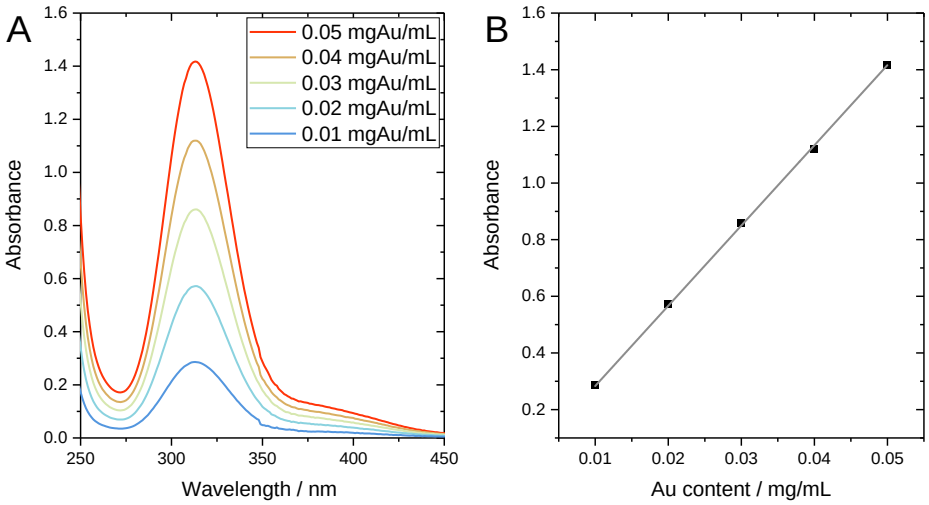

Figure 8-20 (**A**) UV-Vis spectra of $AuCl_4^-$ by dissolving commercial $HAuCl_4 \cdot 3\ H_2O$ with different Au concentrations in 0.1 M aqueous HCl. (**B**) Calibration curve according to the absorbance maximum at 313 nm from the UV-Vis spectra in (A). The calibration function is $y = 28\ x$.

Abbreviations and Symbols

Abbreviations

1D	one-dimensional
2D	two-dimensional
3D	three-dimensional
AFM	atomic force microscopy/microscope
AIBN	azobisisobutyronitrile
aq.	aqueous solution
ATRP	atom transfer radical polymerization
AuNP	gold nanoparticle
CDSPA	4-cyano-4-(dodecylsulfanylthiocarbonyl)sulfanylpentanoic acid
CT	computed tomography
DLS	dynamic light scattering
e.g.	*exempli gratia*
EB	Egyptian blue
EBNS	Egyptian blue nanosheet(s)
EBNS-GS	Egyptian blue nanosheet produced from exfoliation in hot water with glass stir bar
EBNS-SMM	Egyptian blue nanosheets produced by stirred media milling approach
et. al.	*et alii*
equiv.	equivalent
etc.	*et cetera*
FC	field-cooled
i.e.	*id est*
LCST	lower critical solution temperature
MNP	magnetite nanoparticle
MNP@SiO_2	silica-coated magnetite nanoparticle

NHS	*N*-hydroxysuccinimide
NIPAM	*N*-isopropylacrylamide
NIR	near-infrared
NP	nanoparticle
PEG	polyethylene glycol
PEG-AuNP	polyethylene glycol capped gold nanoparticle
PEG-SH	thiol terminated polyethylene glycol
PL	photoluminescence
PMMA	polymethyl methacrylate
PNIPAM	poly(*N*-isopropylacrylamide)
PTFE	polytetrafluoroethylene
QD	quantum dot
RAFT	reversible addition-fragmentation chain transfer
RI	refractive index
rpm	revolutions per minute
RT	room temperature
SAED	selected-area electron diffraction
SE(M)	scanning electron (microscopy/microscope)
SEC	size-exclusion chromatography
SI	surface-initiated
silica-SH	thiol groups functionalized silica nanoparticles
SQUID	superconducting quantum interference device
TE(M)	transmission electron (microscopy/microscope)
TEOS	tetraethyl orthosilicate
TGA	thermogravimetric analysis
THF	tetrahydrofuran
TOAB	tetraoctylammonium bromide
UV	ultraviolet
Vis	visible
w/o	water-in-oil
XRD	X-ray diffraction analysis
ZFC	zero-field-cooled

Symbols

A	surface area
C	concentration of hydrolyzed TEOS
$Đ$	polydispersity index
H	magnetic field strength
m	mass
M_S^{core}	normalized specific saturation magnetization according to the mass of the MNPs cores
M_S^{sample}	specific saturation magnetization
$\bar{M}_n$	number average molar mass
M_s	saturation magnetization
$\bar{M}_w$	mass average molar mass
n	refractive index
T_B	blocking temperature
V	volume
φ	grafting density

Bibliography

[1] Chiefari, J.; Chong, Y. K. B.; Ercole, F.; Krstina, J.; Jeffery, J.; Le, T. P. T.; Mayadunne, R. T. A.; Meijs, G. F.; Moad, C. L.; Moad, G.; Rizzardo, E.; Thang, S. H. Living free-radical polymerization by reversible addition–fragmentation chain transfer: the RAFT process. *Macromolecules* **1998**, *31*, 5559–5562.

[2] Keddie, D. J.; Moad, G.; Rizzardo, E.; Thang, S. H. RAFT agent design and synthesis. *Macromolecules* **2012**, *45*, 5321–5342.

[3] Moad, G.; Rizzardo, E.; Thang, S. H. End-functional polymers, thiocarbonylthio group removal/transformation and reversible addition–fragmentation–chain transfer (RAFT) polymerization. *Polym. Int.* **2011**, *60*, 9–25.

[4] Skandalis, A.; Sentoukas, T.; Giaouzi, D.; Kafetzi, M.; Pispas, S. Latest advances on the synthesis of linear ABC-type triblock terpolymers and star-shaped polymers by RAFT polymerization. *Polymers* **2021**, *13*, 1698.

[5] Keddie, D. J. A guide to the synthesis of block copolymers using reversible-addition fragmentation chain transfer (RAFT) polymerization. *Chem. Soc. Rev.* **2014**, *43*, 496–505.

[6] Semsarilar, M.; Abetz, V. Polymerizations by RAFT: developments of the technique and its application in the synthesis of tailored (co)polymers. *Macromol. Chem. Phys.* **2021**, *222*, 2000311.

[7] Ren, J. M.; McKenzie, T. G.; Fu, Q.; Wong, E. H. H.; Xu, J.; An, Z.; Shanmugam, S.; Davis, T. P.; Boyer, C.; Qiao, G. G. Star polymers. *Chem. Rev.* **2016**, *116*, 6743–6836.

[8] Kuckling, D.; Wycisk, A. Stimuli-responsive star polymers. *J. Polym. Sci., Part A: Polym. Chem.* **2013**, *51*, 2980–2994.

[9] Zheng, Y.; Li, S.; Weng, Z.; Gao, C. Hyperbranched polymers: advances from synthesis to applications. *Chem. Soc. Rev.* **2015**, *44*, 4091–4130.

[10] Bhat, S. I.; Ahmadi, Y.; Ahmad, S. Recent advances in structural modifications of hyperbranched polymers and their applications. *Ind. Eng. Chem. Res.* **2018**, *57*, 10754–10785.

[11] Li, Z.; Tang, M.; Liang, S.; Zhang, M.; Biesold, G. M.; He, Y.; Hao, S.-M.; Choi, W.; Liu, Y.; Peng, J.; Lin, Z. Bottlebrush polymers: from controlled synthesis, self-assembly, properties to applications. *Prog. Polym. Sci.* **2021**, 101387.

[12] Perrier, S. 50th anniversary perspective: RAFT polymerization—a user guide.

Macromolecules **2017**, *50*, 7433–7447.

[13] Deirram, N.; Zhang, C.; Kermaniyan, S. S.; Johnston, A. P. R.; Such, G. K. pH-responsive polymer nanoparticles for drug delivery. *Macromol. Rapid Commun.* **2019**, *40*, 1800917.

[14] Fairbanks, B. D.; Gunatillake, P. A.; Meagher, L. Biomedical applications of polymers derived by reversible addition–fragmentation chain-transfer (RAFT). *Adv. Drug Delivery Rev.* **2015**, *91*, 141–152.

[15] Zhang, A.; Jung, K.; Li, A.; Liu, J.; Boyer, C. Recent advances in stimuli-responsive polymer systems for remotely controlled drug release. *Prog. Polym. Sci.* **2019**, *99*, 101164.

[16] Ahmed, M.; Narain, R. Progress of RAFT based polymers in gene delivery. *Prog. Polym. Sci.* **2013**, *38*, 767–790.

[17] Gurnani, P.; Perrier, S. Controlled radical polymerization in dispersed systems for biological applications. *Prog. Polym. Sci.* **2020**, *102*, 101209.

[18] Jin, X.; Sun, P.; Tong, G.; Zhu, X. Star polymer-based unimolecular micelles and their application in bio-imaging and diagnosis. *Biomaterials* **2018**, *178*, 738–750.

[19] Yang, R.; Wang, X.; Yan, S.; Dong, A.; Luan, S.; Yin, J. Advances in design and biomedical application of hierarchical polymer brushes. *Prog. Polym. Sci.* **2021**, *118*, 101409.

[20] Nagase, K.; Okano, T.; Kanazawa, H. Poly(*N*-isopropylacrylamide) based thermoresponsive polymer brushes for bioseparation, cellular tissue fabrication, and nano actuators. *Nano-Struct. Nano-Objects* **2018**, *16*, 9–23.

[21] Moad, G. RAFT polymerization to form stimuli-responsive polymers. *Polym. Chem.* **2016**, *8*, 177–219.

[22] Lu, C.; Urban, M. W. Stimuli-responsive polymer nano-science: Shape anisotropy, responsiveness, applications. *Prog. Polym. Sci.* **2018**, *78*, 24–46.

[23] Zhao, C.; Ma, Z.; Zhu, X. X. Rational design of thermoresponsive polymers in aqueous solutions: a thermodynamics map. *Prog. Polym. Sci.* **2019**, *90*, 269–291.

[24] Zhao, N.; Yan, L.; Zhao, X.; Chen, X.; Li, A.; Zheng, D.; Zhou, X.; Dai, X.; Xu, F.-J. Versatile types of organic/inorganic nanohybrids: from strategic design to biomedical applications. *Chem. Rev.* **2019**, *119*, 1666–1762.

[25] Pereira, S. O.; Barros-Timmons, A.; Trindade, T. Polymer@gold nanoparticles prepared via RAFT polymerization for opto-biodetection. *Polymers* **2018**, *10*, 189.

[26] Huang, X.; Hu, J.; Li, Y.; Xin, F.; Qiao, R.; Davis, T. P. Engineering organic/inorganic nanohybrids through RAFT polymerization for biomedical applications. *Biomacromolecules* **2019**, *20*, 4243–4257.

[27] Roberts, M. J.; Bentley, M. D.; Harris, J. M. Chemistry for peptide and protein PEGylation. *Adv. Drug Delivery Rev.* **2012**, *64*, 116–127.

[28] Knop, K.; Hoogenboom, R.; Fischer, D.; Schubert, U. S. Poly(ethylene glycol) in drug delivery: pros and cons as well as potential alternatives. *Angew. Chem. Int. Ed.* **2010**, *49*, 6288–6308.

[29] Lowe, S.; O'Brien-Simpson, N. M.; Connal, L. A. Antibiofouling polymer interfaces: poly(ethylene glycol) and other promising candidates. *Polym. Chem.* **2015**, *6*, 198–212.

[30] Serrano, Â.; Sterner, O.; Mieszkin, S.; Zürcher, S.; Tosatti, S.; Callow, M. E.; Callow, J. A.; Spencer, N. D. Nonfouling response of hydrophilic uncharged polymers. *Adv. Funct. Mater.* **2013**, *23*, 5706–5718.

[31] Wu, Z.; Chen, H.; Liu, X.; Zhang, Y.; Li, D.; Huang, H. Protein adsorption on poly(*N*-vinylpyrrolidone)-modified silicon surfaces prepared by surface-initiated atom transfer radical polymerization. *Langmuir* **2009**, *25*, 2900–2906.

[32] Klein, T.; Parkin, J.; de Jongh, P. A. J. M.; Esser, L.; Sepehrizadeh, T.; Zheng, G.; De Veer, M.; Alt, K.; Hagemeyer, C. E.; Haddleton, D. M.; Davis, T. P.; Thelakkat, M.; Kempe, K. Functional brush poly(2-ethyl-2-oxazine)s: synthesis by CROP and RAFT, thermoresponsiveness and grafting onto iron oxide nanoparticles. *Macromol. Rapid Commun.* **2019**, *40*, e1800911.

[33] Estephan, Z. G.; Schlenoff, P. S.; Schlenoff, J. B. Zwitteration as an alternative to PEGylation. *Langmuir* **2011**, *27*, 6794–6800.

[34] Shao, Q.; Jiang, S. Molecular understanding and design of zwitterionic materials. *Adv. Mater.* **2015**, *27*, 15–26.

[35] Qiao, R.; Esser, L.; Fu, C.; Zhang, C.; Hu, J.; Ramírez-arcía, P.; Li, Y.; Quinn, J. F.; Whittaker, M. R.; Whittaker, A. K.; Davis, T. P. Bioconjugation and fluorescence labeling of iron oxide nanoparticles grafted with bromomaleimide-terminal polymers. *Biomacromolecules* **2018**, *19*, 4423–4429.

[36] Montana, D. M.; Nasilowski, M.; Hess, W. R.; Saif, M.; Carr, J. A.; Nienhaus, L.; Bawendi, M. G. Monodisperse and water-soluble quantum dots for SWIR imaging via carboxylic acid copolymer ligands. *ACS Appl. Mater. Interfaces* **2020**, *12*, 35845–35855.

[37] Boyer, C.; Priyanto, P.; Davis, T. P.; Pissuwan, D.; Bulmus, V.; Kavallaris, M.; Teoh, W. Y.; Amal, R.; Carroll, M.; Woodward, R.; St Pierre, T. Anti-fouling magnetic nanoparticles for siRNA delivery. *J. Mater. Chem.* **2010**, *20*, 255–265.

[38] Liu, W.; Greytak, A. B.; Lee, J.; Wong, C. R.; Park, J.; Marshall, L. F.; Jiang, W.; Curtin, P. N.; Ting, A. Y.; Nocera, D. G.; Fukumura, D.; Jain, R. K.; Bawendi, M. G. Compact biocompatible quantum dots via RAFT-mediated synthesis of imidazole-based random copolymer ligand. *J. Am. Chem. Soc.* **2010**, *132*, 472–483.

[39] Dunlap, J. H.; Loszko, A. F.; Flake, R. A.; Huang, Y.; Benicewicz, B. C.; Greytak, A. B. Multiply-binding polymeric imidazole ligands: influence of molecular weight and monomer sequence on colloidal quantum dot stability. *J. Phys. Chem. C* **2018**, *122*, 26756–26763.

[40] Nguyen, T. D.; Vu-Quang, H.; Vo, T. S.; Nguyen, D. C.; Vo, D.-V. N.; Nguyen, D. H.; Lim, K. T.; Tran, D. L.; Bach, L. G. Chemical synthesis and characterization of poly(poly(ethylene glycol) methacrylate)-grafted CdTe nanocrystals via RAFT polymerization for covalent immobilization of adenosine. *Polymers* **2019**, *11*, 77.

[41] Roy, D.; Brooks, W. L. A.; Sumerlin, B. S. New directions in thermoresponsive polymers. *Chem. Soc. Rev.* **2013**, *42*, 7214.

[42] Hogan, K. J.; Mikos, A. G. Biodegradable thermoresponsive polymers: applications in drug delivery and tissue engineering. *Polymer* **2020**, *211*, 123063.

[43] Kwon, Y.; Choi, Y.; Jang, J.; Yoon, S.; Choi, J. NIR laser-responsive PNIPAM and gold nanorod composites for the engineering of thermally reactive drug delivery nanomedicine. *Pharmaceutics* **2020**, *12*, 204.

[44] Sahoo, B.; Devi, K. S. P.; Banerjee, R.; Maiti, T. K.; Pramanik, P.; Dhara, D. Thermal and pH responsive polymer-tethered multifunctional magnetic nanoparticles for targeted delivery of anticancer drug. *ACS Appl. Mater. Interfaces* **2013**, *5*, 3884–3893.

[45] Kakwere, H.; Leal, M. P.; Materia, M. E.; Curcio, A.; Guardia, P.; Niculaes, D.; Marotta, R.; Falqui, A.; Pellegrino, T. Functionalization of strongly interacting magnetic nanocubes with (thermo)responsive coating and their application in hyperthermia and heat-triggered drug delivery. *ACS Appl. Mater. Interfaces* **2015**, *7*, 10132–10145.

[46] Park, C. H.; Yun, H.; Yang, H.; Lee, J.; Kim, B. J. Fluorescent block copolymer-MoS_2 nanocomposites for real-time photothermal heating and imaging. *Adv. Funct. Mater.* **2017**, *27*, 1604403.

[47] Rohleder, D.; Vana, P. Near-infrared-triggered photothermal aggregation of polymer-grafted gold nanorods in a simulated blood fluid. *Biomacromolecules* **2021**, *22*, 1614–1624.

[48] Liu, J.; Detrembleur, C.; De Pauw-Gillet, M.-C.; Mornet, S.; Duguet, E.; Jérôme, C. Gold nanorods coated with a thermo-responsive poly(ethylene glycol)-*b*-poly(*N*-vinylcaprolactam) corona as drug delivery systems for remotely near infrared-triggered release. *Polym. Chem.* **2014**, *5*, 799–813.

[49] Yavuz, M. S.; Cheng, Y.; Chen, J.; Cobley, C. M.; Zhang, Q.; Rycenga, M.; Xie, J.; Kim, C.; Song, K. H.; Schwartz, A. G.; Wang, L. V.; Xia, Y. Gold nanocages covered by smart polymers for controlled release with near-infrared light. *Nat. Mater.* **2009**, *8*, 935–939.

[50] Li, W.; Cai, X.; Kim, C.; Sun, G.; Zhang, Y.; Deng, R.; Yang, M.; Chen, J.; Achilefu, S.; V. Wang, L.; Xia, Y. Gold nanocages covered with thermally-responsive polymers for controlled release by high-intensity focused ultrasound. *Nanoscale* **2011**, *3*, 1724–1730.

[51] Needham, D.; Dewhirst, M. W. The development and testing of a new temperature-sensitive drug delivery system for the treatment of solid tumors. *Adv. Drug Delivery Rev.* **2001**, *53*, 285–305.

[52] Bigall, N. C.; Nandan, B.; Gowd, E. B.; Horechyy, A.; Eychmüller, A. High-resolution metal nanopatterning by means of switchable block copolymer templates. *ACS Appl. Mater. Interfaces* **2015**, *7*, 12559–12569.

[53] Wolkenhauer, M.; Bumbu, G.-G.; Cheng, Y.; Roth, S. V.; Gutmann, J. S. Investigation of micromechanical cantilever sensors with microfocus grazing incidence small-angle X-ray scattering. *Appl. Phys. Lett.* **2006**, *89*, 054101.

[54] Amarandei, G.; O'Dwyer, C.; Arshak, A.; Corcoran, D. Fractal patterning of nanoparticles on polymer films and their SERS capabilities. *ACS Appl. Mater. Interfaces* **2013**, *5*, 8655–8662.

[55] Santoro, G.; Yu, S.; Schwartzkopf, M.; Zhang, P.; Koyiloth Vayalil, S.; Risch, J. F. H.; Rübhausen, M. A.; Hernández, M.; Domingo, C.; Roth, S. V. Silver substrates for surface enhanced raman scattering: correlation between nanostructure and raman scattering enhancement. *Appl. Phys. Lett.* **2014**, *104*, 243107.

[56] Huang, Z.; Geyer, N.; Werner, P.; de Boor, J.; Gösele, U. Metal-assisted chemical etching of silicon: a review. *Adv. Mater.* **2011**, *23*, 285–308.

[57] Han, H.; Huang, Z.; Lee, W. Metal-assisted chemical etching of silicon and nanotechnology applications. *Nano Today* **2014**, *9*, 271–304.

[58] Du, X.; He, J. A self-templated etching route to surface-rough silica nanoparticles for superhydrophobic coatings. *ACS Appl. Mater. Interfaces* **2011**, *3*, 1269–1276.

[59] Wang, X.; Li, S.; Yan, C.; Liu, P.; Ding, J. Fabrication of RGD micro/nanopattern and corresponding study of stem cell differentiation. *Nano Lett.* **2015**, *15*, 1457–1467.

[60] Lohmüller, T.; Aydin, D.; Schwieder, M.; Morhard, C.; Louban, I.; Pacholski, C.; Spatz, J. P. Nanopatterning by block copolymer micelle nanolithography and bioinspired applications. *Biointerphases* **2011**, *6*, MR1–MR12.

[61] Cavalcanti-Adam, E. A.; Volberg, T.; Micoulet, A.; Kessler, H.; Geiger, B.; Spatz, J. P. Cell spreading and focal adhesion dynamics are regulated by spacing of integrin ligands. *Biophys. J.* **2007**, *92*, 2964–2974.

[62] Guasch, J.; Diemer, J.; Riahinezhad, H.; Neubauer, S.; Kessler, H.; Spatz, J. P. Synthesis of binary nanopatterns on hydrogels for initiating cellular responses. *Chem. Mater.* **2016**, *28*, 1806–1815.

[63] Bockstaller, M. R.; Mickiewicz, R. A.; Thomas, E. L. Block copolymer nanocomposites: perspectives for tailored functional materials. *Adv. Mater.* **2005**, *17*, 1331–1349.

[64] Bang, J.; Jeong, U.; Ryu, D. Y.; Russell, T. P.; Hawker, C. J. Block copolymer nanolithography: translation of molecular level control to nanoscale patterns. *Adv. Mater.* **2009**, *21*, 4769–4792.

[65] Spatz, J. P.; Mößmer, S.; Möller, M. Mineralization of gold nanoparticles in a block copolymer microemulsion. *Chem. Eur. J.* **1996**, *2*, 1552–1555.

[66] Lee, G. W.; Lee, S.; Kim, J. H.; Yim, S.-G.; Ryu, J.; Lee, E.; Lee, J.; Yoo, S. I.; Yang, S. Y. Density-controlled freestanding biodegradable nanopillar arrays patterned via block copolymer micelle lithography. *Macromol. Mater. Eng.* **2017**, *302*, 1600361.

[67] Chang, T.; Du, B.; Huang, H.; He, T. Highly tunable complementary micro/submicro-nanopatterned surfaces combining block copolymer self-assembly and colloidal lithography. *ACS Appl. Mater. Interfaces* **2016**, *8*, 22705–22713.

[68] Glass, R.; Möller, M.; Spatz, J. P. Block copolymer micelle nanolithography. *Nanotechnology* **2003**, *14*, 1153–1160.

[69] Ebeling, B.; Vana, P. RAFT-polymers with single and multiple trithiocarbonate groups as uniform gold-nanoparticle coatings. *Macromolecules* **2013**, *46*, 4862–4871.

[70] Peng, W. Binary planetsatellite nanostructure using RAFT polymer. Ph.D. thesis, Georg-August-Universität Göttingen, Göttingen, Germany, 2020.

[71] Ohno, K.; Akashi, T.; Huang, Y.; Tsujii, Y. Surface-initiated living radical polymerization from narrowly size-distributed silica nanoparticles of diameters less than 100 nm. *Macromolecules* **2010**, *43*, 8805–8812.

[72] Rossner, C.; Vana, P. Planet–satellite nanostructures made to order by RAFT star polymers. *Angew. Chem. Int. Ed.* **2014**, *53*, 12639–12642.

[73] Peng, W.; Rossner, C.; Roddatis, V.; Vana, P. Gold-planet–silver-satellite nanostructures using RAFT star polymer. *ACS Macro Lett.* **2016**, *5*, 1227–1231.

[74] Stöber, W.; Fink, A.; Bohn, E. Controlled growth of monodisperse silica spheres in the micron size range. *J. Colloid Interface Sci.* **1968**, *26*, 62–69.

[75] Graf, C.; Vossen, D. L. J.; Imhof, A.; van Blaaderen, A. A general method to coat colloidal particles with silica. *Langmuir* **2003**, *19*, 6693–6700.

[76] Knopp, D.; Tang, D.; Niessner, R. Review: bioanalytical applications of biomolecule-functionalized nanometer-sized doped silica particles. *Anal. Chim. Acta.* **2009**, *647*, 14–30.

[77] Guerrero-Martínez, A.; Pérez-Juste, J.; Liz-Marzán, L. M. Recent progress on silica coating of nanoparticles and related nanomaterials. *Adv. Mater.* **2010**, *22*, 1182–1195.

[78] Zhelev, Z.; Ohba, H.; Bakalova, R. Single quantum dot-micelles coated with silica shell as potentially non-cytotoxic fluorescent cell tracers. *J. Am. Chem. Soc.* **2006**, *128*, 6324–6325.

[79] Ohmori, M.; Matijevic, E. Preparation and properties of uniform coated inorganic colloidal particles: 8. silica on iron. *J. Colloid Interface Sci.* **1993**, *160*, 288–292.

[80] Cai, Y.; Peng, W.; Demeshko, S.; Tian, J.; Vana, P. Silica-coated magnetite nanoparticles carrying a high-density polymer brush shell of hydrophilic polymer. *Macromol. Rapid Commun.* **2018**, *39*, 1800226.

[81] Tadic, M.; Kralj, S.; Lalatonne, Y.; Motte, L. Iron oxide nanochains coated with silica:

synthesis, surface effects and magnetic properties. *Appl. Surf. Sci.* **2019**, *476*, 641–646.

[82] Ryan, J. N.; Elimelech, M.; Baeseman, J. L.; Magelky, R. D. Silica-coated titania and zirconia colloids for subsurface transport field experiments. *Environ. Sci. Technol.* **2000**, *34*, 2000–2005.

[83] LaMer, V. K.; Dinegar, R. H. Theory, production and mechanism of formation of monodispersed hydrosols. *J. Am. Chem. Soc.* **1950**, *72*, 4847–4854.

[84] LaMer, V. K. Nucleation in phase transitions. *Ind. Eng. Chem.* **1952**, *44*, 1270–1277.

[85] Thanh, N. T. K.; Maclean, N.; Mahiddine, S. Mechanisms of nucleation and growth of nanoparticles in solution. *Chem. Rev.* **2014**, *114*, 7610–7630.

[86] Ding, H. L.; Zhang, Y. X.; Wang, S.; Xu, J. M.; Xu, S. C.; Li, G. H. Fe_3O_4@SiO_2 core/shell nanoparticles: the silica coating regulations with a single core for different core sizes and shell thicknesses. *Chem. Mater.* **2012**, *24*, 4572–4580.

[87] El-Toni, A. M.; Yin, S.; Sato, T. Control of silica shell thickness and microporosity of titania–silica core–shell type nanoparticles to depress the photocatalytic activity of titania. *J. Colloid Interface Sci.* **2006**, *300*, 123–130.

[88] Nozawa, K.; Gailhanou, H.; Raison, L.; Panizza, P.; Ushiki, H.; Sellier, E.; Delville, J. P.; Delville, M. H. Smart control of monodisperse stöber silica particles: effect of reactant addition rate on growth process. *Langmuir* **2005**, *21*, 1516–1523.

[89] Kobayashi, Y.; Inose, H.; Nakagawa, T.; Gonda, K.; Takeda, M.; Ohuchi, N.; Kasuya, A. Control of shell thickness in silica-coating of Au nanoparticles and their X-ray imaging properties. *J. Colloid Interface Sci.* **2011**, *358*, 329–333.

[90] Arriagada, F. J.; Osseo-Asare, K. Synthesis of nanosize silica in a nonionic water-in-oil microemulsion: effects of the water/surfactant molar ratio and ammonia concentration. *J. Colloid Interface Sci.* **1999**, *211*, 210–220.

[91] Koole, R.; van Schooneveld, M. M.; Hilhorst, J.; de Mello Donegá, C.; Hart, D. C. t.; van Blaaderen, A.; Vanmaekelbergh, D.; Meijerink, A. On the incorporation mechanism of hydrophobic quantum dots in silica spheres by a reverse microemulsion method. *Chem. Mater.* **2008**, *20*, 2503–2512.

[92] Crane, C. C.; Tao, J.; Wang, F.; Zhu, Y.; Chen, J. Mask-assisted seeded growth of segmented metallic heteronanostructures. *J. Phys. Chem. C* **2014**, *118*, 28134–28142.

[93] Han, Y.; Jiang, J.; Lee, S. S.; Ying, J. Y. Reverse microemulsion-mediated synthesis of silica-coated gold and silver nanoparticles. *Langmuir* **2008**, *24*, 5842–5848.

[94] Gilroy, K. D.; Peng, H.-C.; Yang, X.; Ruditskiy, A.; Xia, Y. Symmetry breaking during nanocrystal growth. *Chem. Commun.* **2017**, *53*, 4530–4541.

[95] Liberman, A.; Mendez, N.; Trogler, W. C.; Kummel, A. C. Synthesis and surface functionalization of silica nanoparticles for nanomedicine. *Surf. Sci. Rep.* **2014**, *69*, 132–158.

[96] Li, C.; Han, J.; Ryu, C. Y.; Benicewicz, B. C. A versatile method to prepare RAFT agent anchored substrates and the preparation of PMMA grafted nanoparticles. *Macromolecules* **2006**, *39*, 3175–3183.

[97] Zhu, L.-J.; Zhu, L.-P.; Zhao, Y.-F.; Zhu, B.-K.; Xu, Y.-Y. Anti-fouling and anti-bacterial polyethersulfone membranes quaternized from the additive of poly(2-dimethylamino ethyl methacrylate) grafted SiO_2 nanoparticles. *J. Mater. Chem. A* **2014**, *2*, 15566–15574.

[98] Cui, L.; Wang, R.; Ji, X.; Hu, M.; Wang, B.; Liu, J. Template-assisted synthesis of biodegradable and pH-responsive polymer capsules via RAFT polymerization for controlled drug release. *Mater. Chem. Phys.* **2014**, *148*, 87–95.

[99] Piech, M.; George, M. C.; Bell, N. S.; Braun, P. V. Patterned colloid assembly by grafted photochromic polymer layers. *Langmuir* **2006**, *22*, 1379–1382.

[100] Mulvihill, M. J.; Rupert, B. L.; He, R.; Hochbaum, A.; Arnold, J.; Yang, P. Synthesis of bifunctional polymer nanotubes from silicon nanowire templates via atom transfer radical polymerization. *J. Am. Chem. Soc.* **2005**, *127*, 16040–16041.

[101] Ohno, K.; Morinaga, T.; Koh, K.; Tsujii, Y.; Fukuda, T. Synthesis of monodisperse silica particles coated with well-defined, high-density polymer brushes by surface-initiated atom transfer radical polymerization. *Macromolecules* **2005**, *38*, 2137–2142.

[102] Bagheri, A.; Arandiyan, H.; Adnan, N. N. M.; Boyer, C.; Lim, M. Controlled direct growth of polymer shell on upconversion nanoparticle surface via visible light regulated polymerization. *Macromolecules* **2017**, *50*, 7137–7147.

[103] Kavand, A.; Blanck, C.; Przybilla, F.; Mély, Y.; Anton, N.; Vandamme, T.; A. Serra, C.; Chan-Seng, D. Investigating the growth of hyperbranched polymers by self-condensing vinyl RAFT copolymerization from the surface of upconversion nanoparticles. *Polym. Chem.* **2020**, *11*, 4313–4325.

[104] Bagheri, A.; Sadrearhami, Z.; Adnan, N. N. M.; Boyer, C.; Lim, M. Surface functionalization of upconversion nanoparticles using visible light-mediated polymerization. *Polymer* **2018**, *151*, 6–14.

[105] Pourjavadi, A.; Kohestanian, M.; Streb, C. pH and thermal dual-responsive poly(NIPAM-co-GMA)-coated magnetic nanoparticles via surface-initiated RAFT polymerization for controlled drug delivery. *Mater. Sci. Eng. C* **2020**, *108*, 110418.

[106] Zoppe, J. O.; Ataman, N. C.; Mocny, P.; Wang, J.; Moraes, J.; Klok, H.-A. Surface-initiated controlled radical polymerization: state-of-the-art, opportunities, and challenges in surface and interface engineering with polymer brushes. *Chem. Rev.* **2017**, *117*, 1105–1318.

[107] Biggs, C. I.; Walker, M.; Gibson, M. I. "grafting to" of RAFTed responsive polymers to glass substrates by thiol-ene and critical comparison to thiol-gold coupling. *Biomacromolecules* **2016**, *17*, 2626–2633.

[108] A. Olson, R.; B. Korpusik, A.; S. Sumerlin, B. Enlightening advances in polymer bioconjugate chemistry: light-based techniques for grafting to and from biomacromolecules. *Chem. Sci.* **2020**, *11*, 5142–5156.

[109] L. M. Gonçalves, J.; J. Castanheira, E.; P. C. Alves, S.; Baleizão, C.; Farinha, J. P. Grafting with RAFT—gRAFT strategies to prepare hybrid nanocarriers with core-shell architecture. *Polymers* **2020**, *12*, 2175.

[110] Falatach, R.; McGlone, C.; Al-Abdul-Wahid, M. S.; Averick, S.; Page, R. C.; Berberich, J. A.; Konkolewicz, D. The best of both worlds: active enzymes by grafting-to followed by grafting-from a protein. *Chem. Commun.* **2015**, *51*, 5343–5346.

[111] Mazloomi-Rezvani, M.; Salami-Kalajahi, M.; Roghani-Mamaqani, H. "Grafting to" approach for surface modification of AuNPs with RAFT-mediated synthesized smart polymers: stimuli-responsive behaviors of hybrid nanoparticles. *J. Phys. Chem. Solids* **2018**, *123*, 183–190.

[112] Mazloomi-Rezvani, M.; Salami-Kalajahi, M.; Roghani-Mamaqani, H.; Pirayesh, A. Effect of surface modification with various thiol compounds on colloidal stability of gold nanoparticles. *Appl. Organomet. Chem.* **2018**, *32*, e4079.

[113] Gargari, J. E.; Shakeri, A.; Kalal, H. S.; Khanchi, A.; Rashedi, H. Synthesis and characterization of silica–polyvinyl imidazole core–shell nanoparticles via combination of RAFT polymerization and grafting-to method. *Polym. Adv. Technol.* **2017**, *28*, 1884–1891.

[114] Chancellor, A. J.; Seymour, B. T.; Zhao, B. Characterizing polymer-grafted nanoparticles: from basic defining parameters to behavior in solvents and self-assembled structures. *Anal. Chem.* **2019**, *91*, 6391–6402.

[115] Ohno, K.; Ma, Y.; Huang, Y.; Mori, C.; Yahata, Y.; Tsujii, Y.; Maschmeyer, T.; Moraes, J.; Perrier, S. Surface-initiated reversible addition–fragmentation chain transfer (RAFT) polymerization from fine particles functionalized with trithiocarbonates. *Macromolecules* **2011**, *44*, 8944–8953.

[116] Roeven, E.; Kuzmyn, A. R.; Scheres, L.; Baggerman, J.; Smulders, M. M.; Zuilhof, H. PLL–poly(HPMA) bottlebrush-based antifouling coatings: three grafting routes. *Langmuir* **2020**, *36*, 10187–10199.

[117] Ghasemi, S.; Karim, S. Organic/inorganic hybrid composed of modified polyacrylamide grafted silica supported Pd nanoparticles using RAFT polymerization process: controlled synthesis, characterization and catalytic activity. *Mater. Chem. Phys.* **2018**, *205*, 347–358.

[118] Conzatti, G.; Cavalie, S.; Combes, C.; Torrisani, J.; Carrere, N.; Tourrette, A. PNIPAM grafted surfaces through ATRP and RAFT polymerization: chemistry and bioadhesion. *Colloids Surf., B* **2017**, *151*, 143–155.

[119] Foster, J. C.; Radzinski, S. C.; Matson, J. B. Graft polymer synthesis by RAFT

transfer-to. *J. Polym. Sci., Part A: Polym. Chem.* **2017**, *55*, 2865–2876.

[120] Moehrke, J.; Vana, P. The kinetics of surface-initiated RAFT polymerization of butyl acrylate mediated by trithiocarbonates. *Macromol. Chem. Phys.* **2017**, *218*, 1600506.

[121] Eskandari, P.; Abousalman-Rezvani, Z.; Roghani-Mamaqani, H.; Salami-Kalajahi, M.; Mardani, H. Polymer grafting on graphene layers by controlled radical polymerization. *Adv. Colloid Interface Sci.* **2019**, *273*, 102021.

[122] Boyer, C.; Stenzel, M. H.; Davis, T. P. Building nanostructures using RAFT polymerization. *J. Polym. Sci., Part A: Polym. Chem.* **2011**, *49*, 551–595.

[123] Jaksch, H.; Seipel, W.; Weiner, K.; El Goresy, A. Egyptian blue—cuprorivaite a window to ancient Egyptian technology. *Naturwissenschaften* **1983**, *70*, 525–535.

[124] Riederer, J. In *Artists'pigments: A handbook of their history and characteristics*; FitzHugh, E. W., Ed.; National Gallery of Art, Washington, 1997; Vol. 3; pp 23–46.

[125] Pabst, A. Structures of some tetragonal sheet silicates. *Acta Crystallogr.* **1959**, *12*, 733–739.

[126] Bensch, W.; Schur, M. Crystal structure of calcium copper phyllo-decaoxotetrasilicate, $CaCuSi_4O_{10}$. *Zeitschrift für Kristallographie* **1995**, 530.

[127] Warner, T. E. *Synthesis, properties and mineralogy of important inorganic materials*; John Wiley & Sons, Ltd., 2011; Chapter Artificial Cuprorivaite $CaCuSi_4O_{10}$ (Egyptian Blue) by a Salt-Flux Method, pp 26–49.

[128] Pozza, G.; Ajò, D.; Chiari, G.; De Zuane, F.; Favaro, M. Photoluminescence of the inorganic pigments Egyptian blue, Han blue and Han purple. *J. Cult. Heritage* **2000**, *1*, 393–398.

[129] Verri, G. The spatially resolved characterisation of Egyptian blue, Han blue and Han purple by photo-induced luminescence digital imaging. *Anal. Bioanal.Chem.* **2009**, *394*, 1011–1021.

[130] Accorsi, G.; Verri, G.; Bolognesi, M.; Armaroli, N.; Clementi, C.; Miliani, C.; Romani, A. The exceptional near-infrared luminescence properties of cuprorivaite (Egyptian blue). *Chem. Commun.* **2009**, 3392–3394.

[131] Johnson-McDaniel, D.; Barrett, C. A.; Sharafi, A.; Salguero, T. T. Nanoscience of an ancient pigment. *J. Am. Chem. Soc.* **2013**, *135*, 1677–1679.

[132] Johnson-McDaniel, D.; Salguero, T. T. Exfoliation of Egyptian blue and Han blue, two alkali earth copper silicate-based pigments. *J. Visualized Exp.* **2014**, *86*, 51686.

[133] Xiao, L.; Li, J.; Brougham, D. F.; Fox, E. K.; Feliu, N.; Bushmelev, A.; Schmidt, A.; Mertens, N.; Kiessling, F.; Valldor, M.; Fadeel, B.; Mathur, S. Water-soluble superparamagnetic magnetite nanoparticles with biocompatible coating for enhanced magnetic resonance imaging. *ACS Nano* **2011**, *5*, 6315–6324.

[134] Sun, C.; Lee, J. S.; Zhang, M. Magnetic nanoparticles in MR imaging and drug delivery. *Adv. Drug Delivery Rev.* **2008**, *60*, 1252–1265.

[135] Wang, Y.-X. J.; Hussain, S. M.; Krestin, G. P. Superparamagnetic iron oxide contrast agents: physicochemical characteristics and applications in MR imaging. *Eur. Radiol.* **2001**, *11*, 2319–2331.

[136] Tromsdorf, U. I.; Bruns, O. T.; Salmen, S. C.; Beisiegel, U.; Weller, H. A highly effective, nontoxic T_1 MR contrast agent based on ultrasmall PEGylated iron oxide nanoparticles. *Nano Lett.* **2009**, *9*, 4434–4440.

[137] Sun, C.; Du, K.; Fang, C.; Bhattarai, N.; Veiseh, O.; Kievit, F.; Stephen, Z.; Lee, D.; Ellenbogen, R. G.; Ratner, B.; Zhang, M. PEG-mediated synthesis of highly dispersive multifunctional superparamagnetic nanoparticles: their physicochemical properties and function *in vivo*. *ACS Nano* **2010**, *4*, 2402–2410.

[138] Huang, J.; Bu, L.; Xie, J.; Chen, K.; Cheng, Z.; Li, X.; Chen, X. Effects of nanoparticle size on cellular uptake and liver MRI with polyvinylpyrrolidone-coated iron oxide nanoparticles. *ACS Nano* **2010**, *4*, 7151–7160.

[139] Ulbrich, K.; Holá, K.; Subr, V.; Bakandritsos, A.; Tucek, J.; Zboril, R. Targeted drug delivery with polymers and magnetic nanoparticles: covalent and noncovalent approaches, release control, and clinical studies. *Chem. Rev.* **2016**, *116*, 5338–5431.

[140] Chen, Y.; Chen, H.; Zeng, D.; Tian, Y.; Chen, F.; Feng, J.; Shi, J. Core/shell structured hollow mesoporous nanocapsules: a potential platform for simultaneous cell imaging and anticancer drug delivery. *ACS Nano* **2010**, *4*, 6001–6013.

[141] Park, J.; Kadasala, N. R.; Abouelmagd, S. A.; Castanares, M. A.; Collins, D. S.; Wei, A.; Yeo, Y. Polymer–iron oxide composite nanoparticles for EPR-independent drug delivery. *Biomaterials* **2016**, *101*, 285–295.

[142] Zanganeh, S.; Hutter, G.; Spitler, R.; Lenkov, O.; Mahmoudi, M.; Shaw, A.; Pajarinen, J. S.; Nejadnik, H.; Goodman, S.; Moseley, M.; Coussens, L. M.; Daldrup-Link, H. E. Iron oxide nanoparticles inhibit tumour growth by inducing pro-inflammatory macrophage polarization in tumour tissues. *Nat. Nanotechnol.* **2016**, *11*, 986.

[143] Maier-Hauff, K.; Ulrich, F.; Nestler, D.; Niehoff, H.; Wust, P.; Thiesen, B.; Orawa, H.; Budach, V.; Jordan, A. Efficacy and safety of intratumoral thermotherapy using magnetic iron-oxide nanoparticles combined with external beam radiotherapy on patients with recurrent glioblastoma multiforme. *J. Neurooncol.* **2011**, *103*, 317–324.

[144] Andreu, I.; Natividad, E.; Solozabal, L.; Roubeau, O. Nano-objects for addressing the control of nanoparticle arrangement and performance in magnetic hyperthermia. *ACS Nano* **2015**, *9*, 1408–1419.

[145] Bazak, R.; Houri, M.; El Achy, S.; Kamel, S.; Refaat, T. Cancer active targeting by nanoparticles: a comprehensive review of literature. *J. Cancer Res. Clin. Oncol.* **2015**, *141*,

769–784.

[146] Pham, A. L.-T.; Lee, C.; Doyle, F. M.; Sedlak, D. L. A silica-supported iron oxide catalyst capable of activating hydrogen peroxide at neutral pH values. *Environ. Sci. Technol.* **2009**, *43*, 8930–8935.

[147] Coker, V. S.; Bennett, J. A.; Telling, N. D.; Henkel, T.; Charnock, J. M.; van der Laan, G.; Pattrick, R. A.; Pearce, C. I.; Cutting, R. S.; Shannon, I. J. Microbial engineering of nanoheterostructures: biological synthesis of a magnetically recoverable palladium nanocatalyst. *ACS Nano* **2010**, *4*, 2577–2584.

[148] Wang, Z.; Shen, B.; Zou, A.; He, N. Synthesis of Pd/Fe_3O_4 nanoparticle-based catalyst for the cross-coupling of acrylic acid with iodobenzene. *Chem. Eng. J.* **2005**, *113*, 27–34.

[149] Rossi, L. M.; Costa, N. J.; Silva, F. P.; Wojcieszak, R. Magnetic nanomaterials in catalysis: advanced catalysts for magnetic separation and beyond. *Green Chem.* **2014**, *16*, 2906–2933.

[150] Ross, C. A.; Haratani, S.; Castaño, F. J.; Hao, Y.; Hwang, M.; Shima, M.; Cheng, J. Y.; Vögeli, B.; Farhoud, M.; Walsh, M.; Smith, H. I. Magnetic behavior of lithographically patterned particle arrays. *J. Appl. Phys.* **2002**, *91*, 6848–6853.

[151] Kumar, T. A.; Bardea, A.; Shai, Y.; Yoffe, A.; Naaman, R. Patterning gradient properties from sub-micrometers to millimeters by magnetolithography. *Nano Lett.* **2010**, *10*, 2262–2267.

[152] Bardea, A.; Baram, A.; Tatikonda, A. K.; Naaman, R. Magnetolithographic patterning of inner walls of a tube: a new dimension in microfluidics and sequential microreactors. *J. Am. Chem. Soc.* **2009**, *131*, 18260–18262.

[153] Han, X. X.; Schmidt, A. M.; Marten, G.; Fischer, A.; Weidinger, I. M.; Hildebrandt, P. Magnetic silver hybrid nanoparticles for surface-enhanced resonance Raman spectroscopic detection and decontamination of small toxic molecules. *ACS Nano* **2013**, *7*, 3212–3220.

[154] Zhang, Y.; Xu, S.; Luo, Y.; Pan, S.; Ding, H.; Li, G. Synthesis of mesoporous carbon capsules encapsulated with magnetite nanoparticles and their application in wastewater treatment. *J. Mater. Chem.* **2011**, *21*, 3664–3671.

[155] Ohno, K.; Mori, C.; Akashi, T.; Yoshida, S.; Tago, Y.; Tsujii, Y.; Tabata, Y. Fabrication of contrast agents for magnetic resonance imaging from polymer-brush-afforded iron oxide magnetic nanoparticles prepared by surface-initiated living radical polymerization. *Biomacromolecules* **2013**, *14*, 3453–3462.

[156] Stjerndahl, M.; Andersson, M.; Hall, H. E.; Pajerowski, D. M.; Meisel, M. W.; Duran, R. S. Superparamagnetic Fe_3O_4/SiO_2 nanocomposites: enabling the tuning of both the iron oxide load and the size of the nanoparticles. *Langmuir* **2008**, *24*, 3532–3536.

[157] Davila-Ibanez, A. B.; Salgueirino, V.; Martinez-Zorzano, V.; Mariño Fernández, R.; García-Lorenzo, A.; Maceira-Campos, M.; Muñoz Ubeda, M.; Junquera, E.; Aicart, E.; Rivas, J. Magnetic silica nanoparticle cellular uptake and cytotoxicity regulated by electrostatic polyelectrolytes–DNA loading at their surface. *ACS Nano* **2011**, *6*, 747–759.

[158] Kunzmann, A.; Andersson, B.; Thurnherr, T.; Krug, H.; Scheynius, A.; Fadeel, B. Toxicology of engineered nanomaterials: focus on biocompatibility, biodistribution and biodegradation. *Biochim. Biophys. Acta, Gen. Subj.* **2011**, *1810*, 361–373.

[159] Zhang, Y.; Kohler, N.; Zhang, M. Surface modification of superparamagnetic magnetite nanoparticles and their intracellular uptake. *Biomaterials* **2002**, *23*, 1553–1561.

[160] Benezra, M.; Penate-Medina, O.; Zanzonico, P. B.; Schaer, D.; Ow, H.; Burns, A.; DeStanchina, E.; Longo, H. E., Valerie; Iyer, S.; Wolchok, J.; Larson, S. M.; Wiesner, U.; Bradbury, M. S. Multimodal silica nanoparticles are effective cancer-targeted probes in a model of human melanoma. *J. Clin. Investig.* **2011**, *121*, 2768–2780.

[161] Schmaljohann, D. Thermo-and pH-responsive polymers in drug delivery. *Adv. Drug Delivery Rev.* **2006**, *58*, 1655–1670.

[162] Kade, M. J.; Burke, D. J.; Hawker, C. J. The power of thiol-ene chemistry. *J. Polym. Sci., Part A: Polym. Chem.* **2010**, *48*, 743–750.

[163] Li, M.; De, P.; Li, H.; Sumerlin, B. S. Conjugation of RAFT-generated polymers to proteins by two consecutive thiol–ene reactions. *Polym. Chem.* **2010**, *1*, 854–859.

[164] Pan, H.; Yang, J.; Kopečková, P.; Kopeček, J. Backbone degradable multiblock textitN-(2-hydroxypropyl) methacrylamide copolymer conjugates via reversible addition- fragmentation chain transfer polymerization and thiol- ene coupling reaction. *Biomacromolecules* **2010**, *12*, 247–252.

[165] Willcock, H.; O'Reilly, R. K. End group removal and modification of RAFT polymers. *Polym. Chem.* **2010**, *1*, 149–157.

[166] Sun, S.; Zeng, H.; Robinson, D. B.; Raoux, S.; Rice, P. M.; Wang, S. X.; Li, G. Monodisperse MFe_2O_4 (M = Fe, Co, Mn) nanoparticles. *J. Am. Chem. Soc.* **2004**, *126*, 273–279.

[167] Lu, A.-H.; Salabas, E. L.; Schüth, F. Magnetic nanoparticles: synthesis, protection, functionalization, and application. *Angew. Chem. Int. Ed.* **2007**, *46*, 1222–1244.

[168] Ebeling, B.; Eggers, S.; Hendrich, M.; Nitschke, A.; Vana, P. Flipping the pressure- and temperature-dependent cloud-point behavior in the cononsolvency system of poly(*N*-isopropylacrylamide) in water and ethanol. *Macromolecules* **2014**, *47*, 1462–1469.

[169] Jaiswal, M. K.; Gogoi, M.; Sarma, H. D.; Banerjee, R.; Bahadur, D. Biocompatibility, biodistribution and efficacy of magnetic nanohydrogels in inhibiting growth of tumors in experimental mice models. *Biomater. Sci.* **2014**, *2*, 370–380.

[170] Ohno, K.; Morinaga, T.; Takeno, S.; Tsujii, Y.; Fukuda, T. Suspensions of silica particles grafted with concentrated polymer brush: effects of graft chain length on brush

layer thickness and colloidal crystallization. *Macromolecules* **2007**, *40*, 9143–9150.

[171] Granitzer, P.; Rumpf, K.; Roca, A.; Morales, M.; Poelt, P.; Albu, M. Investigation of a mesoporous silicon based ferromagnetic nanocomposite. *Nanoscale Res. Lett.* **2010**, *5*, 374.

[172] Garcá-Otero, J.; Porto, M.; Rivas, J.; Bunde, A. Influence of dipolar interaction on magnetic properties of ultrafine ferromagnetic particles. *Phys. Rev. Lett.* **2000**, *84*, 167.

[173] Woinska, M.; Szczytko, J.; Majhofer, A.; Gosk, J.; Dziatkowski, K.; Twardowski, A. Magnetic interactions in an ensemble of cubic nanoparticles: a monte carlo study. *Phys. Rev. B* **2013**, *88*, 144421.

[174] Pansare, V. J.; Hejazi, S.; Faenza, W. J.; Prud'homme, R. K. Review of long-wavelength optical and NIR imaging materials: contrast agents, fluorophores, and multifunctional nano carriers. *Chem. Mater.* **2012**, *24*, 812–827.

[175] Wang, R.; Zhang, F. NIR luminescent nanomaterials for biomedical imaging. *J. Mater. Chem. B* **2014**, *2*, 2422–2443.

[176] Hong, G.; Antaris, A. L.; Dai, H. Near-infrared fluorophores for biomedical imaging. *Nat. Biomed. Eng.* **2017**, *1*, 1–22.

[177] Zeng, H.; Zhou, T.; Wang, L.; Xie, R.-J. Two-site occupation for exploring ultra-broadband near-infrared phosphor–double-perovskite $La_2MgZrO_6:Cr^{3+}$. *Chem. Mater.* **2019**, *31*, 5245–5253.

[178] Qiao, J.; Zhou, G.; Zhou, Y.; Zhang, Q.; Xia, Z. Divalent europium-doped near-infrared-emitting phosphor for light-emitting diodes. *Nat. Comm.* **2019**, *10*, 1–7.

[179] Correia, S. F. H.; Frias, A. R.; Fu, L.; Rondão, R.; Pecoraro, E.; Ribeiro, S. J. L.; André, P. S.; Ferreira, R. A. S.; Carlos, L. D. Large-area tunable visible-to-near-infrared luminescent solar concentrators. *Adv. Sustainable Syst.* **2018**, *2*, 1800002.

[180] Rondão, R.; Frias, A. R.; Correia, S. F.; Fu, L.; de Zea Bermudez, V.; André, P. S.; Ferreira, R. A.; Carlos, L. D. High-performance near-infrared luminescent solar concentrators. *ACS Appl. Mater. Interfaces* **2017**, *9*, 12540–12546.

[181] Zhang, D.; Wang, L.; Yuan, X.; Gong, Y.; Liu, H.; Zhang, J.; Zhang, X.; Liu, Y.; Tan, W. Naked-eye readout of analyte-induced NIR fluorescence responses by an initiation–input–transduction nanoplatform. *Angew. Chem. Int. Ed.* **2020**, *59*, 695–699.

[182] Carr, J. A.; Franke, D.; Caram, J. R.; Perkinson, C. F.; Saif, M.; Askoxylakis, V.; Datta, M.; Fukumura, D.; Jain, R. K.; Bawendi, M. G.; Bruns, O. T. Shortwave infrared fluorescence imaging with the clinically approved near-infrared dye indocyanine green. *Proc. Natl. Acad. Sci. U.S.A.* **2018**, *115*, 4465–4470.

[183] Escobedo, J. O.; Rusin, O.; Lim, S.; Strongin, R. M. NIR dyes for bioimaging applications. *Curr. Opin. Chem. Biol.* **2010**, *14*, 64–70.

[184] Zhao, Q.; Huang, C.; Li, F. Phosphorescent heavy-metal complexes for bioimaging. *Chem. Soc. Rev.* **2011**, *40*, 2508–2524.

[185] Michalet, X.; Pinaud, F. F.; Bentolila, L. A.; Tsay, J. M.; Doose, S.; Li, J. J.; Sundaresan, G.; Wu, A.; Gambhir, S.; Weiss, S. Quantum dots for live cells, *in vivo* imaging, and diagnostics. *Science* **2005**, *307*, 538–544.

[186] Bruns, O. T. et al. Next-generation *in vivo* optical imaging with short-wave infrared quantum dots. *Nat. Biomed. Eng.* **2017**, *1*, 1–11.

[187] Welsher, K.; Liu, Z.; Daranciang, D.; Dai, H. Selective probing and imaging of cells with single walled carbon nanotubes as near-infrared fluorescent molecules. *Nano Lett.* **2008**, *8*, 586–590.

[188] Cherukuri, P.; Bachilo, S. M.; Litovsky, S. H.; Weisman, R. B. Near-infrared fluorescence microscopy of single-walled carbon nanotubes in phagocytic cells. *J. Am. Chem. Soc.* **2004**, *126*, 15638–15639.

[189] Hertel, T.; Himmelein, S.; Ackermann, T.; Stich, D.; Crochet, J. Diffusion limited photoluminescence quantum yields in 1-D semiconductors: single-wall carbon nanotubes. *ACS nano* **2010**, *4*, 7161–7168.

[190] Li, H.; Wang, X.; Ohulchanskyy, T. Y.; Chen, G. Lanthanide-doped near-infrared nanoparticles for biophotonics. *Adv. Mat.* **2021**, *33*, 2000678.

[191] Errington, B.; Lawson, G.; Lewis, S. W.; Smith, G. D. Micronised Egyptian blue pigment: a novel near-infrared luminescent fingerprint dusting powder. *Dyes Pigm.* **2016**, *132*, 310–315.

[192] Selvaggio, G. et al. Exfoliated near infrared fluorescent silicate nanosheets for (bio)photonics. *Nat. Commun.* **2020**, *11*, 1–11.

[193] Salguero, T. T.; Johnson-McDaniel, D.; Barrett, C. A.; Sharafi, A.; Weimar, R.; Blevins, T. Nanoscience of metal silicate-based pigments. *MRS Online Proceedings Library Archive* **2014**, *1618*, 161–166.

[194] Vopálenská, I.; Váchová, L.; Palková, Z. New biosensor for detection of copper ions in water based on immobilized genetically modified yeast cells. *Biosens. Bioelectron.* **2015**, *72*, 160–167.

[195] Jalil, R. A.; Zhang, Y. Biocompatibility of silica coated $NaYF_4$ upconversion fluorescent nanocrystals. *Biomaterials* **2008**, *29*, 4122–4128.

[196] Souris, J. S.; Chen, N.-T.; Cheng, S.-H.; Chen, C.-T.; Lo, L.-W. *Cancer Theranostics*; Elsevier, 2014; pp 363–391.

[197] Shahbazi, S.; Goodpaster, J. V.; Smith, G. D.; Becker, T.; Lewis, S. W. Preparation, characterization, and application of a lipophilic coated exfoliated Egyptian blue for near-infrared luminescent latent fingermark detection. *Forensic Chem.* **2020**, *18*, 100208.

[198] Mazzi, F.; Pabst, A. Reexamination of cuprorivaite. *Am. Mineral.* **1962**, *47*, 409–411.

[199] Breitung-Faes, S.; Kwade, A. Nano particle production in high-power-density mills. *Chem. Eng. Res. Des.* **2008**, *86*, 390–394.

[200] Knieke, C.; Steinborn, C.; Romeis, S.; Peukert, W.; Breitung-Faes, S.; Kwade, A. Nanoparticle production with stirred-media mills: opportunities and limits. *Chem. Eng. Technol.* **2010**, *33*, 1401–1411.

[201] Schilde, C.; Breitung-Faes, S.; Kampen, I.; Kwade, A. Grinding kinetics of nano-sized particles for different electrostatic stabilizing acids in a stirred media mill. *Powder Technol.* **2013**, *235*, 1008–1016.

[202] Stenger, F.; Mende, S.; Schwedes, J.; Peukert, W. Nanomilling in stirred media mills. *Chem. Eng. Sci.* **2005**, *60*, 4557–4565.

[203] Bitterlich, A.; Laabs, C.; Busmann, E.; Grandeury, A.; Juhnke, M.; Bunjes, H.; Kwade, A. Challenges in nanogrinding of active pharmaceutical ingredients. *Chem. Eng. Technol.* **2014**, *37*, 840–846.

[204] Flach, F.; Breitung-Faes, S.; Kwade, A. Scaling wet fine grinding processes of organic particles using stirred media mills. *Chem. Ing. Tech.* **2017**, *89*, 1051–1059.

[205] Flach, F.; Konnerth, C.; Peppersack, C.; Schmidt, J.; Damm, C.; Breitung-Faes, S.; Peukert, W.; Kwade, A. Impact of formulation and operating parameters on particle size and grinding media wear in wet media milling of organic compounds–a case study for pyrene. *Adv. Powder Technol.* **2016**, *27*, 2507–2519.

[206] Stender, H.-H.; Kwade, A.; Schwedes, J. Stress energy distribution in different stirred media mill geometries. *Int. J. Miner. Process.* **2004**, *74*, S103–S117.

[207] Breitung-Faes, S.; Kwade, A. Use of an enhanced stress model for the optimization of wet stirred media milling processes. *Chem. Eng. Technol.* **2014**, *37*, 819–826.

[208] Breitung-Faes, S.; Kwade, A. Mill, material, and process parameters–a mechanistic model for the set-up of wet-stirred media milling processes. *Adv. Powder Technol.* **2019**, *30*, 1425–1433.

[209] Souza, T. G. F.; Ciminelli, V. S. T.; Mohallem, N. D. S. A comparison of TEM and DLS methods to characterize size distribution of ceramic nanoparticles. *J. Phys. Conf. Ser.* **2016**, *733*, 012039.

[210] Shen, S.; Ding, B.; Zhang, S.; Qi, X.; Wang, K.; Tian, J.; Yan, Y.; Ge, Y.; Wu, L. Near-infrared light-responsive nanoparticles with thermosensitive yolk-shell structure for multimodal imaging and chemo-photothermal therapy of tumor. *Nanomedicine* **2017**, *13*, 1607–1616.

[211] Ward, M. A.; Georgiou, T. K. Thermoresponsive polymers for biomedical applications. *Polymers* **2011**, *3*, 1215–1242.

[212] Yildiz, I.; Yildiz, B. S. Applications of thermoresponsive magnetic nanoparticles. *J. Nanomater.* **2016**, *16*, 357.

[213] Lü, J.; Yang, Y.; Gao, J.; Duan, H.; Lü, C. Thermoresponsive amphiphilic block copolymer-stablilized gold nanoparticles: synthesis and high catalytic properties. *Langmuir* **2018**, *34*, 8205–8214.

[214] Liu, G.; Wang, D.; Zhou, F.; Liu, W. Electrostatic self-assembly of Au nanoparticles onto thermosensitive magnetic core-shell microgels for thermally tunable and magnetically recyclable catalysis. *Small* **2015**, *11*, 2807–2816.

[215] Xiao, Q.; Li, Y.; Li, F.; Zhang, M.; Zhang, Z.; Lin, H. Rational design of a thermalresponsive-polymer-switchable FRET system for enhancing the temperature sensitivity of upconversion nanophosphors. *Nanoscale* **2014**, *6*, 10179–10186.

[216] Zheng, Y.; Soeriyadi, A. H.; Rosa, L.; Ng, S. H.; Bach, U.; Justin Gooding, J. Reversible gating of smart plasmonic molecular traps using thermoresponsive polymers for single-molecule detection. *Nat. Commun.* **2015**, *6*, 1–8.

[217] Maji, S.; Cesur, B.; Zhang, Z.; De Geest, B. G.; Hoogenboom, R. Poly(*N*-isopropylacrylamide) coated gold nanoparticles as colourimetric temperature and salt sensors. *Polym. Chem.* **2016**, *7*, 1705–1710.

[218] Lee, L.-H.; Chen, W.-C. High-refractive-index thin films prepared from trialkoxysilane-capped poly(methyl methacrylate)-titania materials. *Chem. Mater.* **2001**, *13*, 1137–1142.

[219] Loste, J.; Lopez-Cuesta, J.-M.; Billon, L.; Garay, H.; Save, M. Transparent polymer nanocomposites: an overview on their synthesis and advanced properties. *Prog. Polym. Sci.* **2019**, *89*, 133–158.

[220] Li, J.-Y.; Qiu, L.; Xu, X.-F.; Pan, C.-Y.; Hong, C.-Y.; Zhang, W.-J. Photo-responsive camptothecin-based polymeric prodrug coated silver nanoparticles for drug release behaviour tracking via the nanomaterial surface energy transfer (NSET) effect. *J. Mater. Chem. B* **2018**, *6*, 1678–1687.

[221] Qiu, L.; Li, J.-W.; Hong, C.-Y.; Pan, C.-Y. Silver nanoparticles covered with pH-sensitive camptothecin-loaded polymer prodrugs: switchable fluorescence "off" or "on" and drug delivery dynamics in living cells. *ACS Appl. Mater. Interfaces* **2017**, *9*, 40887–40897.

[222] Gao, P. F.; Li, Y. F.; Huang, C. Z. Plasmonics-attended NSET and PRET for analytical applications. *TrAC, Trends Anal. Chem.* **2020**, *124*, 115805.

[223] Sun, D.; Tian, Y.; Zhang, Y.; Xu, Z.; Sfeir, M. Y.; Cotlet, M.; Gang, O. Light-harvesting nanoparticle core–shell clusters with controllable optical output. *ACS Nano* **2015**, *9*, 5657–5665.

[224] Kulakovich, O.; Strekal, N.; Yaroshevich, A.; Maskevich, S.; Gaponenko, S.; Nabiev, I.; Woggon, U.; Artemyev, M. Enhanced luminescence of CdSe quantum dots on gold colloids. *Nano Lett.* **2002**, *2*, 1449–1452.

[225] Kang, K. A.; Wang, J.; Jasinski, J. B.; Achilefu, S. Fluorescence manipulation by gold nanoparticles: from complete quenching to extensive enhancement. *J. Nanobiotechnol.* **2011**, *9*, 16.

[226] Gandra, N.; Portz, C.; Tian, L.; Tang, R.; Xu, B.; Achilefu, S.; Singamaneni, S.

Probing distance-dependent plasmon-enhanced near-infrared fluorescence using polyelectrolyte multilayers as dielectric spacers. *Angew. Chem. Int. Ed.* **2014**, *53*, 866–870.

[227] Mout, R.; Moyano, D. F.; Rana, S.; Rotello, V. M. Surface functionalization of nanoparticles for nanomedicine. *Chem. Soc. Rev.* **2012**, *41*, 2539–2544.

[228] Fratila, R. M.; Mitchell, S. G.; del Pino, P.; Grazu, V.; de la Fuente, J. M. Strategies for the biofunctionalization of gold and iron oxide nanoparticles. *Langmuir* **2014**, *30*, 15057–15071.

[229] Horechyy, A.; Nandan, B.; Zafeiropoulos, N. E.; Formanek, P.; Oertel, U.; Bigall, N. C.; Eychmüller, A.; Stamm, M. A step-wise approach for dual nanoparticle patterning via block copolymer self-assembly. *Adv. Funct. Mater.* **2013**, *23*, 483–490.

[230] Mendes, P. M.; Jacke, S.; Critchley, K.; Plaza, J.; Chen, Y.; Nikitin, K.; Palmer, R. E.; Preece, J. A.; Evans, S. D.; Fitzmaurice, D. Gold nanoparticle patterning of silicon wafers using chemical e-beam lithography. *Langmuir* **2004**, *20*, 3766–3768.

[231] Wang, W. M.; Stoltenberg, R. M.; Liu, S.; Bao, Z. Direct patterning of gold nanoparticles using dip-pen nanolithography. *ACS Nano* **2008**, *2*, 2135–2142.

[232] Liu, L.; Zheng, M.; Li, Z.; Li, Q.; Mao, C. Patterning nanoparticles with DNA molds. *ACS Appl. Mater. Interfaces* **2019**, *11*, 13853–13858.

[233] Yang, G.; Nanda, J.; Wang, B.; Chen, G.; Hallinan, D. T. Self-assembly of large gold nanoparticles for surface-enhanced raman spectroscopy. *ACS Appl. Mater. Interfaces* **2017**, *9*, 13457–13470.

[234] Asbahi, M.; Lim, K. T. P.; Wang, F.; Duan, H.; Thiyagarajah, N.; Ng, V.; Yang, J. K. W. Directed self-assembly of densely packed gold nanoparticles. *Langmuir* **2012**, *28*, 16782–16787.

[235] Martin, M. N.; Basham, J. I.; Chando, P.; Eah, S.-K. Charged gold nanoparticles in non-polar solvents: 10-min synthesis and 2D self-assembly. *Langmuir* **2010**, *26*, 7410–7417.

[236] Sayin, M.; Dahint, R. Formation of charge-nanopatterned templates with flexible geometry via layer by layer deposition of polyelectrolytes for directed self-assembly of gold nanoparticles. *Nanotechnology* **2017**, *28*, 135303.

[237] Do, M. T.; Tong, Q. C.; Lidiak, A.; Luong, M. H.; Ledoux-Rak, I.; Lai, N. D. Nano-patterning of gold thin film by thermal annealing combined with laser interference techniques. *Appl. Phys. A* **2016**, *122*, 1–6.

[238] Lin, S.; Li, M.; Dujardin, E.; Girard, C.; Mann, S. One-dimensional plasmon coupling by facile self-assembly of gold nanoparticles into branched chain networks. *Adv. Mater.* **2005**, *17*, 2553–2559.

[239] Deng, Z.; Tian, Y.; Lee, S.-H.; Ribbe, A. E.; Mao, C. DNA-encoded self-assembly of gold nanoparticles into one-dimensional arrays. *Angew. Chem. Int. Ed.* **2005**, *44*, 3582–

3585.

[240] Zheng, J.; Zhu, Z.; Chen, H.; Liu, Z. Nanopatterned assembling of colloidal gold nanoparticles on silicon. *Langmuir* **2000**, *16*, 4409–4412.

[241] Kwon, N. K.; Lee, T. K.; Kwak, S. K.; Kim, S. Y. Aggregation-driven controllable plasmonic transition of silica-coated gold nanoparticles with temperature-dependent polymernanoparticle interactions for potential applications in optoelectronic devices. *ACS Appl. Mater. Interfaces* **2017**, *9*, 39688–39698.

[242] Kim, S. Y.; Zukoski, C. F. Particle restabilization in silica/PEG/ethanol suspensions: how strongly do polymers need to adsorb to stabilize against aggregation? *Langmuir* **2011**, *27*, 5211–5221.

[243] Nuzzo, R. G.; Dubois, L. H.; Allara, D. L. Fundamental studies of microscopic wetting on organic surfaces. 1. Formation and structural characterization of a self-consistent series of polyfunctional organic monolayers. *J. Am. Chem. Soc.* **1990**, *112*, 558–569.

[244] Tian, J.; Huang, B.; Zhang, W. Precise self-assembly and controlled catalysis of thermoresponsive core–satellite multicomponent hybrid nanoparticles. *Langmuir* **2019**, *35*, 266–275.

[245] Oesterhelt, F.; Rief, M.; Gaub, H. E. Single molecule force spectroscopy by AFM indicates helical structure of poly(ethylene-glycol) in water. *New J. Phys.* **1999**, *1*, 6.

[246] Huang, X.; Appelhans, D.; Formanek, P.; Simon, F.; Voit, B. Tailored synthesis of intelligent polymer nanocapsules: an investigation of controlled permeability and pH-dependent degradability. *ACS Nano* **2012**, *6*, 9718–9726.

[247] Chen, Y.; Chen, H.; Guo, L.; He, Q.; Chen, F.; Zhou, J.; Feng, J.; Shi, J. Hollow/rattle-type mesoporous nanostructures by a structural difference-based selective etching strategy. *ACS Nano* **2010**, *4*, 529–539.

[248] Wong, Y. J.; Zhu, L.; Teo, W. S.; Tan, Y. W.; Yang, Y.; Wang, C.; Chen, H. Revisiting the Stöber method: inhomogeneity in silica shells. *J. Am. Chem. Soc.* **2011**, *133*, 11422–11425.

[249] Zafarani-Moattar, M. T.; Sadeghi, R. Phase behavior of aqueous two-phase PEG + NaOH system at different temperatures. *J. Chem. Eng. Data* **2004**, *49*, 297–300.

[250] Tsai, C.-Y.; Lin, J.-W.; Wu, C.-Y.; Lin, P.-T.; Lu, T.-W.; Lee, P.-T. Plasmonic coupling in gold nanoring dimers: observation of coupled bonding mode. *Nano Lett.* **2012**, *12*, 1648–1654.

[251] Dey, P.; Thurecht, K. J.; Fredericks, P. M.; Blakey, I. Stepwise like supramolecular polymerization of plasmonic nanoparticle building blocks through complementary interactions. *Macromolecules* **2020**, *53*, 7469–7478.

[252] Dey, P.; Zhu, S.; Thurecht, K. J.; Fredericks, P. M.; Blakey, I. Self assembly of plasmonic core–satellite nano-assemblies mediated by hyperbranched polymer linkers.

J. Mater. Chem. B **2014**, *2*, 2827–2837.

[253] Gandra, N.; Abbas, A.; Tian, L.; Singamaneni, S. Plasmonic planet–satellite analogues: hierarchical self-assembly of gold nanostructures. *Nano Lett.* **2012**, *12*, 2645–2651.

[254] Jin, R. Nanoparticle clusters light up in SERS. *Angew. Chem. Int. Ed.* **2010**, *49*, 2826–2829.

[255] Hatti-Kaul, R. Aqueous two-phase systems. *Mol. Biotechnol.* **2001**, *19*, 269–277.

[256] Karlstroem, G. A new model for upper and lower critical solution temperatures in poly(ethylene oxide) solutions. *J. Phys. Chem.* **1985**, *89*, 4962–4964.

[257] Kim, H. J.; Wang, W.; Travesset, A.; Mallapragada, S. K.; Vaknin, D. Temperature-induced tunable assembly of columnar phases of nanorods. *ACS Nano* **2020**, *14*, 6007–6012.

[258] Donath, T.; Pfeiffer, F.; Bunk, O.; Grünzweig, C.; Hempel, E.; Popescu, S.; Vock, P.; David, C. Toward clinical X-ray phase-contrast CT: demonstration of enhanced soft-tissue contrast in human specimen. *Invest. Radiol.* **2010**, *45*, 445–452.

[259] Namasivayam, S.; Kalra, M. K.; Torres, W. E.; Small, W. C. Adverse reactions to intravenous iodinated contrast media: a primer for radiologists. *Emerg. Radiol.* **2006**, *12*, 210–215.

[260] Badea, C. T.; Athreya, K. K.; Espinosa, G.; Clark, D.; Ghafoori, A. P.; Li, Y.; Kirsch, D. G.; Johnson, G. A.; Annapragada, A.; Ghaghada, K. B. Computed tomography imaging of primary lung cancer in mice using a liposomal-iodinated contrast agent. *PLoS One* **2012**, *7*, e34496.

[261] Menk, R. H.; Schültke, E.; Hall, C.; Arfelli, F.; Astolfo, A.; Rigon, L.; Round, A.; Ataelmannan, K.; MacDonald, S. R.; Juurlink, B. H. J. Gold nanoparticle labeling of cells is a sensitive method to investigate cell distribution and migration in animal models of human disease. *Nanomed. Nanotechnol. Biol. Med.* **2011**, *7*, 647–654.

[262] Chhour, P.; Naha, P. C.; O'Neill, S. M.; Litt, H. I.; Reilly, M. P.; Ferrari, V. A.; Cormode, D. P. Labeling monocytes with gold nanoparticles to track their recruitment in atherosclerosis with computed tomography. *Biomaterials* **2016**, *87*, 93–103.

[263] Popovtzer, R.; Agrawal, A.; Kotov, N. A.; Popovtzer, A.; Balter, J.; Carey, Thomas. E.; Kopelman, R. Targeted gold nanoparticles enable molecular CT imaging of cancer. *Nano Lett.* **2008**, *8*, 4593–4596.

[264] Arfelli, F.; Rigon, L.; Menk, R. H. Microbubbles as X-ray scattering contrast agents using analyzer-based imaging. *Phys. Med. Biol.* **2010**, *55*, 1643–1658.

[265] Millard, T. P.; Endrizzi, M.; Everdell, N.; Rigon, L.; Arfelli, F.; Menk, R. H.; Stride, E.; Olivo, A. Evaluation of microbubble contrast agents for dynamic imaging with X-ray phase contrast. *Sci. Rep.* **2015**, *5*, 1–8.

[266] Chen, J.; Wiley, B.; Li, Z.-Y.; Campbell, D.; Saeki, F.; Cang, H.; Au, L.; Lee, J.; Li, X.;

Xia, Y. Gold nanocages: engineering their structure for biomedical applications. *Adv. Mater.* **2005**, *17*, 2255–2261.

[267] Liang, H.-P.; Wan, L.-J.; Bai, C.-L.; Jiang, L. Gold hollow nanospheres: tunable surface plasmon resonance controlled by interior-cavity sizes. *J. Phys. Chem. B* **2005**, *109*, 7795–7800.

[268] Boisselier, E.; Astruc, D. Gold nanoparticles in nanomedicine: preparations, imaging, diagnostics, therapies and toxicity. *Chem. Soc. Rev.* **2009**, *38*, 1759–1782.

[269] Huang, Y.; Zheng, Y.; Sarkar, A.; Xu, Y.; Stefik, M.; Benicewicz, B. C. Matrix-free polymer nanocomposite thermoplastic elastomers. *Macromolecules* **2017**, *50*, 4742–4753.

[270] Brust, M.; Walker, M.; Bethell, D.; Schiffrin, D. J.; Whyman, R. Synthesis of thiol-derivatised gold nanoparticles in a two-phase liquid–liquid system. *J. Chem. Soc., Chem. Commun.* **1994**, *0*, 801–802.

[271] Gangopadhayay, A. K.; Chakravorty, A. Scharge transfer spectra of some gold(III) complexes. *J. Chem. Phys.* **1961**, *35*, 2206–2209.

[272] Qiao, Z.; Feng, H.; Zhou, J. Molecular dynamics simulations on the melting of gold nanoparticles. *Phase Transit.* **2014**, *87*, 59–70.

[273] King, S. R.; Massicot, J.; McDonagh, A. M. A straightforward route to tetrachloroauric acid from gold metal and molecular chlorine for nanoparticle synthesis. *Metals* **2015**, *5*, 1454–1461.

Acknowledgments

First of all, I want to express my sincere gratitude to my supervisor Prof. Philipp Vana for his magnificent guide and support, inspiring discussions, and encouragement during the last 6 years throughout my bachelor thesis, master thesis, and whole PhD study. From a student to a researcher, my experience in his group is a true treasure for me.

I also want to thank my co-supervisor Prof. Frauke Alves: Our interdisciplinary cooperation and discussion expanded my scientific vision and offered me great opportunities to develop and test my nanostructures for biomedical researches. I am also grateful to my co-supervisor Prof. Andreas Janshoff for his interest in my work and helpful discussions.

Prof. Marcus Müller, Jun.-Prof. Daniel Obenchain and Dr. Tim Schäfer are gratefully acknowledged for being members of my thesis committee.

During this journey, I am very lucky to have the opportunity to collaborate with so many amazing experts for a great number of interdisciplinary cooperation. I appreciate Dr. Serhiy Demeshko from Prof. Franc Meyer's group for the SQUID measurements, the excellent result offered me great insight into the interaction between my nanoparticles. Christoph Peppersack, Sandra Breitung-Faesb, and Prof Arno Kwade from Institut für Partikeltechnik, Technische Universität Braunschweig are acknowledged for their kind efforts on cracking down Egyptian blue using their excellent milling expertise and equipment. Denis Pluta from the group of Prof. Nadja-C. Bigall (Institut für Physikalische Chemie und Elektrochemie, Leibniz Universität Hannover) is gratefully acknowledged for the great help on the NIR photonluminence measurements. I would like to thank PD Dr. Christian Dullin from Universitätsmedizin Göttingen for the great project of using my nanostructure for the *in vivo* CT imaging experiment. Furthermore, I am very grateful to Prof. Akito Masuhara, Keiji Shito from the University of Yamagata for

the support and intriguing scientific and cultural discussions during my conference tour in Japan. I am very thankful to Mr. Matthias Hahn from the institute for material physics for his teaching and assistance on the TEM measurements.

I want to thank all members of the MMC group especially my ex- and current officemates for the great working ambient and helpful discussions. There amazing mates are: Dr. Wentao Peng, Dr. Alex Groschopp, Dr. Jannik Wagner, Dr. Judith Rauschendorfer, and Qingyuan Song.

Special thanks to Dr. Wentao Peng and Luise Fanslau for grinding (at the speed of light) our big review together. I would also like to thank Qingyuan Song for being my trainee and precipitating for the “hollow gold” project.

I also want to give my thanks to Luise Fanslau, Enno Meyer, and Dr. Wentao Peng for the careful proofreading of my thesis.

Big special thanks go to my faithful husband: Dr. Wentao Peng, who paid all my bills during the last decade :) In this way, I believe that we are going to have a bright future together.

Finally, I’d like to be thankful to my family and all my friends who support me along my journey.